Ph.D. DISSERTATION

Enhancement of Mechanical Conformability *via* Nanocomposites for Augmented Spatial Signal/Heat Transfer in Wearable Sensors and Energy Devices

웨어러블 센서 및 에너지 소자의
공간 신호 및 열 전달 증진을 위한
나노복합체를 이용한 기계적 순응성 향상

AUGUST 2020

DEPARTMENT OF ELECTRICAL
AND COMPUTER ENGINEERING
COLLEGE OF ENGINEERING
SEOUL NATIONAL UNIVERSITY

BYEONGMOON LEE

Abstract

Enhancement of Mechanical Conformability *via* Nanocomposites for Augmented Spatial Signal/Heat Transfer in Wearable Sensors and Energy Devices.

BYEONGMOON LEE

DEPARTMENT OF ELECTRICAL AND COMPUTER ENGINEERING

COLLEGE OF ENGINEERING

SEOUL NATIONAL UNIVERSITY

Electronic skin (e-skin) that mimics mechanical and functional properties of human skin has a strong impact on the field of wearable electronics. Beyond being just wearable, e-skin seamlessly interfaces human, machine, and environment by perfectly adhering to soft and time-dynamic three-dimensional (3D) geometries of human skin and organs. Real-time and intimate access to the sources of physical and biological signals can be achieved by adopting soft or flexible electronic sensors that can detect pressure, strain, temperature, and chemical substances. Such extensions in accessible signals drastically accelerate the growth of the Internet of Things

(IoT) and expand its application to health monitoring, medical implants, and novel human-machine interfaces.

In wearable sensors and energy devices, which are essential building blocks for skin-like functionalities and self-power generation in e-skin, spatial signals and heat are transferred from time-dynamic 3D environments through numerous geometries and electrical devices. Therefore, the transfer of high-fidelity signals or a large amount of heat is of great importance in these devices. The mechanical conformability potentially enhances the signal/heat transfer by providing conformal geometries with the 3D sources. However, while the relation between system conformability and electrical signals has been widely investigated, studies on its effect on the transfer of other mechanical signals and heat remain in their early stages. Furthermore, because active materials and their designs for sensors and energy devices have been optimized to maximize their performances, it is challenging to develop ultrathin or soft forms of active layers without compromising their performances. Therefore, many devices in these fields suffer from poor spatial signal/heat transfer due to limited conformability.

In this dissertation, to ultimately augment the functionalities of wearable sensors and energy devices, comprehensive studies on conformability enhancement *via* composite materials and its effect on signal/heat transfer, especially in pressure sensors and thermoelectric generators (TEGs), are conducted. A solution for each device is carefully optimized to reinforce its conformability, taking account of the structure, characteristics, and potential advantages of the device. As a result, the mechanical conformability of each device is significantly enhanced, improving signal/heat transfer and consequently augmenting its

functionalities, which have been considered as tough challenges in each area. The effect of the superior conformability on signal/heat transfer is systematically analyzed *via* a series of experiments and finite element analyses. Demonstrations of practical wearable electronics show the feasibility of the proposed strategies.

For wearable pressure sensors, ultrathin piezoresistive layers are developed using cellulose/nanowire nanocomposites (CNNs). The unique nanostructured surface enables unprecedentedly high sensor performances such as ultrahigh sensitivity, wide working range, and fast response time without microstructures in sensing layers. Because the ultrathin pressure sensor perfectly conforms to 3D contact objects, it transfers pressure distribution into conductivity distribution with high spatial fidelity. When integrated with a quantum dot-based electroluminescent film, the transferred high-resolution pressure distribution is directly visualized without the need for pixel structures. The electroluminescent skin enables real-time smart touch interfaces that can identify the user as well as touch force and location.

For high-performance wearable TEGs, an intrinsically soft heat transfer and electrical interconnection platform (SHEP) is developed. The SHEP comprises AgNW random networks for intrinsically stretchable electrodes and magnetically self-assembled metal particles for soft thermal conductors (STCs). The stretchable electrodes lower the flexural rigidity, and the STCs enhance the heat exchange capability of the soft platform, maintaining its softness. As a result, a compliant TEG with SHEPs forms unprecedentedly conformal contact with 3D heat sources, thereby enhancing the heat transfer to the TE legs. This results in significant improvement in thermal energy harvesting on 3D surfaces. Self-powered wearable warning

systems indicating an abrupt temperature increase with light-emitting alarms are demonstrated to show the feasibility of this strategy.

This study provides a systematic and comprehensive framework for enhancing mechanical conformability of e-skin and consequently improving the transfer of spatial signals and energy from time-dynamic and complex 3D surfaces. The framework can be universally applied to other fields in wearable electronics that require improvement in signal/energy transfer through conformal contact with 3D surfaces. The materials, manufacturing methods, and devices introduced in this dissertation will be actively exploited in practical and futuristic applications of wearable electronics such as skin-attachable advanced user interfaces, implantable bio-imaging systems, nervous systems in soft robotics, and self-powered artificial tactile systems.

Keyword: Wearable electronics, Electronic skin, Pressure sensors, Thermoelectric generators, Mechanical conformability, Nanocomposites

Student Number: 2014-21683

Contents

List of Tables

List of Figures

Chapter 1

Introduction

1.1 Wearable Electronics and Electronic Skin

Wearable electronics that are wirelessly connected to a network and exchange data acquired from the human body realize the “Internet of Things” (IoT), where a broad range of applications such as healthcare, advanced user interfaces, and prosthetics can be achieved. Recent efforts to realize a new type of electronics, namely electronic skin (e-skin), that mimics mechanical and functional properties of human or animal skin, have a strong impact on the field of wearables and IoT. Unlike conventional wearable electronics that have a fixed shape, e-skin is flexible, stretchable, and even self-healable. These unique mechanical properties place e-skin at a particular position in wearable electronics. Beyond being just wearable, e-skin seamlessly interfaces human, machine, and environment by perfectly adhering to soft and time-dynamic three-dimensional (3D) geometries of human skin and organs (Figure 1.1) [1-3]. Real-time and intimate access to the sources of physical and biological signals from complex 3D surfaces can be achieved by adopting

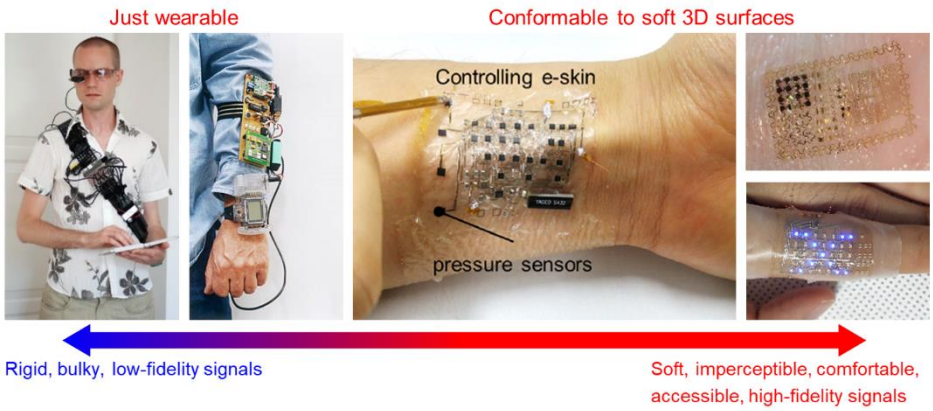

Figure 1.1 | Differences between rigid wearables and e-skin [1-3].

soft [4-6] or ultrathin [7-9] forms of electronic sensors that can detect pressure [10-12], strain [13,14], temperature [15], and chemical substances [16,17]. Such extensions in accessible and sharable signals drastically accelerate the growth of the IoT and expands its application to health monitoring [16,17], medical implants [18,19], and novel human-machine interfaces [20-22] (Figure 1.2). For instance, researchers developed fully integrated and mechanically flexible biosensor arrays that can monitor and analyze perspiration *via* real-time signal processing and wireless transmission, providing a wide range of biomarkers for personalized diagnostic [16]. Other researchers reported stretchable patch systems that can be conformably attached to human skin for continuous monitoring of glucose and feedback therapy [17]. These unprecedented applications suggest how mechanical conformability of e-skin enables us to monitor and process biomarkers that are inaccessible with previous rigid electronics in daily life. Furthermore, the skin-like sensors offer an opportunity to replace real skin in prosthetics [23,24], and sensory systems for soft robotics [2,25].

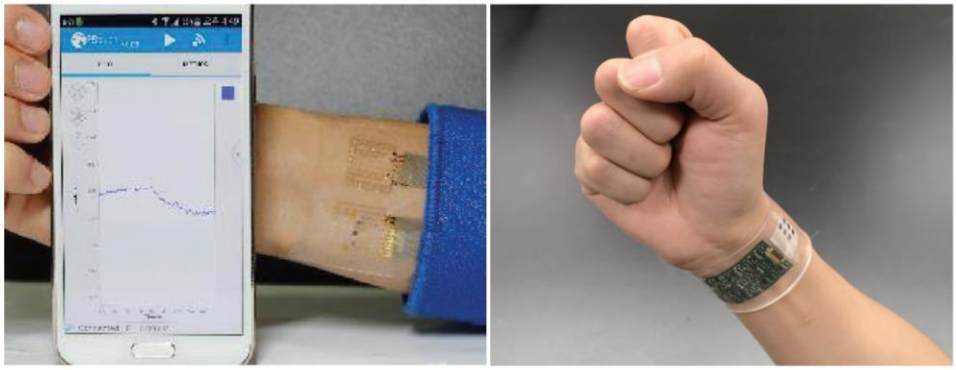

Health monitoring & treatment

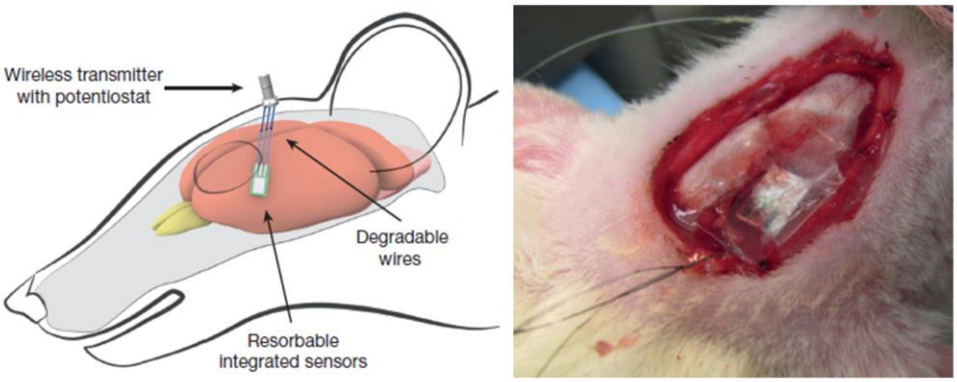

Medical implants & bio-applications

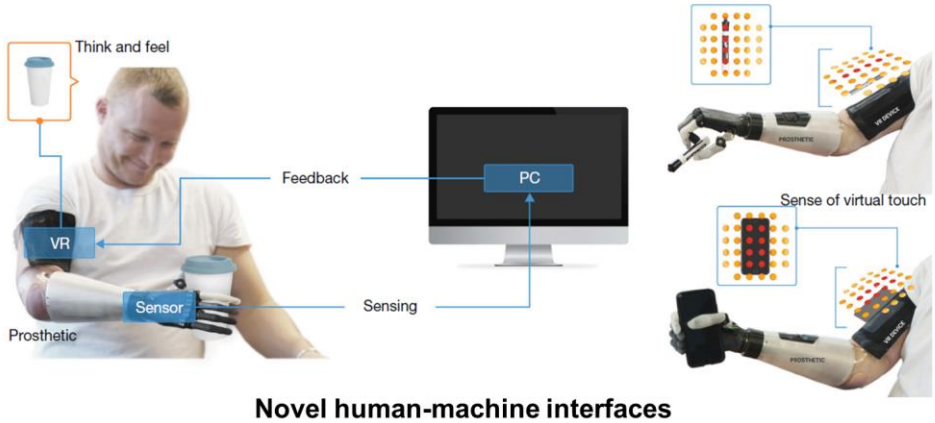

Novel human-machine interfaces

Figure 1.2 | Unprecedented Applications enabled by e-skin [16-20].

As the field of e-skin grows, methods to supply power to e-skin without compromising its advantages such as conformability and portability are emerging as a significant issue. The conjunction of e-skin and energy harvesting technologies opens the door to stand-alone and self-sustainable skin electronics. Ambient energy is converted to electrical energy for self-powered e-skin *via* energy harvesting devices. Enabling technologies include photovoltaic [8], piezoelectric [26], triboelectric [27], and thermoelectric generators [28]. Soft and conformable forms of such devices enable e-skin to continuously and accurately detect physiological signals on living tissues without the need for additional power sources or batteries. They allow remote sensing without the need for maintenance or human intervention, realizing self-sustainable or disposable electronics that are critical to the IoT.

Most recently, an innovative concept of self-healing has joined the stream of e-skin, further enriching its versatility. Like wound healing in human skin, self-healable e-skin can recover its substrate and electrical functionalities [29,30]. Such devices are especially beneficial in soft robotics and prosthetics in that damages during actuation and interaction with the environment can be recovered, preventing system failure. Furthermore, reliable and recyclable operation in body-attachable and implantable electronics can be achieved by self-healing devices.

For the schemes and applications above, recent researches on e-skin mainly focus on conferring mechanical flexibility or softness on electronic components such as sensors and energy devices. However, these novel mechanical properties cannot be realized with a conventional paradigm of rigid electronics. For example, processes for inorganic-based integrated circuits cannot be applied to the polymer-/organic-based devices due to their

high process temperature. Moreover, brittle and rigid properties of conventional electronic materials need to be adjusted or replaced to have flexibility or softness. Therefore, new materials, device design, and manufacturing methods that are entirely different from those of conventional rigid electronics are highly required for realizing e-skin. In the next section, as a sine qua non of e-skin, the mechanical conformability is introduced, and strategies to enhance the mechanical conformability, including materials, structures, and methods, are described in detail.

1.2 Mechanical Conformability of Electronic Skin

1.2.1 Definition and Advantages

The mechanical conformability of an electronic system means how easily the geometry of the system follows the surface morphology of target objects. Figure 1.3 shows possible geometries of membranes with different conformabilities laminated onto a wavy surface. A membrane with excellent conformability complies well with the surface morphology. On the other hand, a membrane with poor conformability remains almost flat rather than gets

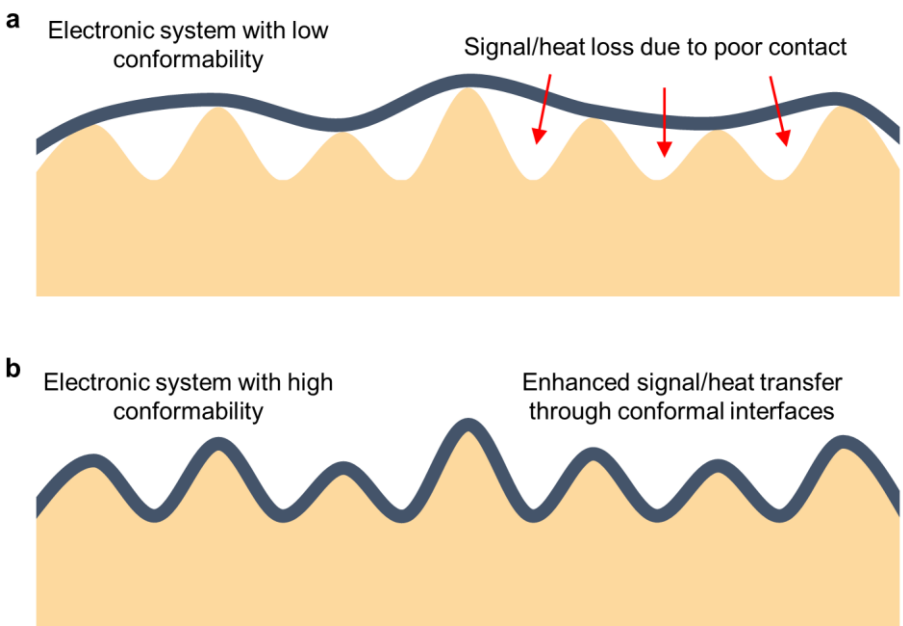

Figure 1.3 | Geometries of membranes with different conformabilities on a wavy surface. a, Poor contact and air gaps formed by the membrane with low conformability. **b**, Conformal contact formed by the membrane with high conformability.

deformed to conform to the wavy surface. More scientifically, electronic systems with high mechanical conformability require less force and, consequently, less work to deform them, which simultaneously suggests that they store low strain energy to restore their morphology. Therefore, they can form extremely soft interfaces with 3D surfaces, offering comfortability and imperceptibility when worn. Furthermore, high mechanical conformability enhances adhesion and contact quality between electronics and 3D environments by preventing air gaps and thereby facilitates the transfer of signals and heat through the interface. For example, the enhanced conformability of electrodes results in significant improvement in the electrical fidelity when measuring bioelectrical signals from the human body such as electroencephalogram (EEG), electrocardiogram (ECG), and electromyogram (EMG) [31].

Therefore, understanding governing parameters for the mechanical conformability of e-skin and engineering them are of great importance in designing and fabricating highly conformable e-skin. The mechanical conformability of an electronic system could be relatively but reliably quantified by bending moments and strain energy of the system under bending deformation. A bent system with lower bending moments and strain energy implies that the system requires less force and work while undergoing bending. Such a system can easily be bent and conform to a curvilinear surface. Therefore, high mechanical conformability will be achieved by reducing the potential bending moment and strain energy of the system for a specific bending radius. Suppose that an electronic system with a thickness of T and Young's modulus of E completely conformed to a curved surface

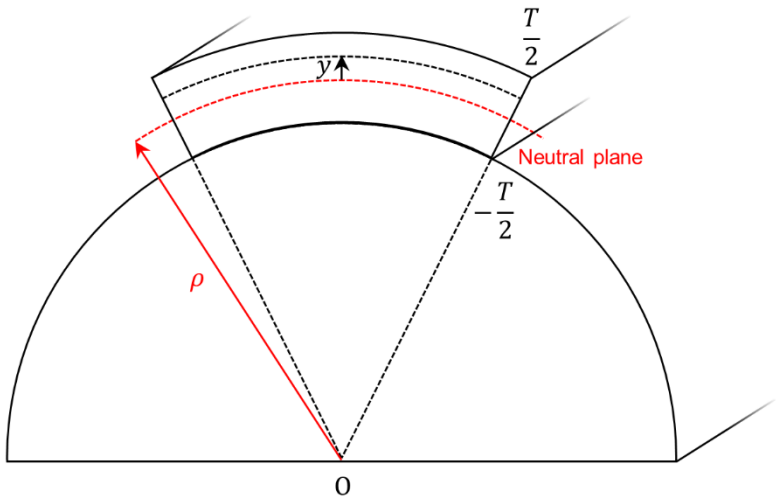

Figure 1.4 | Geometry of electronic system conforming to a curved surface.

with a bending radius of ρ, as depicted in Figure 1.4. From geometry, the bending strain ($\varepsilon_{\text{bending}}$) at the distance of y from the neutral plane can be written in the following form:

$$\varepsilon_{\text{bending}} = \frac{y}{\rho} \tag{1}$$

The corresponding bending stress (σ_{bending}) can be expressed using Hooke's law and Equation 1 as follows:

$$\sigma_{\text{bending}} = E\varepsilon_{\text{bending}} = E\frac{y}{\rho} \tag{2}$$

Note that because the x-axis lies along the neutral plane, the y value represents the distance from the neutral plane. The bending moment (M_{bending}) acting on a section per unit length along the z-axis can be written as follows:

$$M_{\text{bending}} = \int y\sigma_{\text{bending}} dA = \int y\sigma_{\text{bending}} dy \tag{3}$$

Substituting Equation 2 into Equation 3 suggests the following:

$$M_{\text{bending}} = \int_{-\frac{T}{2}}^{\frac{T}{2}} \frac{Ey^2}{\rho}\, dy = \frac{ET^3}{12\rho} \tag{4}$$

Here, $\frac{ET^3}{12}$ in Equation 4 is defined as flexural rigidity, which represents the bending moment required to increase one unit of curvature by bending. Therefore, the flexural rigidity of the system can be one good criterion for evaluating its mechanical conformability. The bending energy (U_{bending}) per unit area can be calculated by integrating the strain energy density (u) over the thickness as follows:

$$U_{\text{bending}}\ (\text{per unit area}) = \int u dy = \int_{-\frac{T}{2}}^{\frac{T}{2}} \frac{\sigma_{\text{bending}}^2}{2E}\, dy \tag{5}$$

Substituting Equation 2 into Equation 5 suggests the following:

$$U_{\text{bending}}\ (\text{per unit area}) = \int_{-\frac{T}{2}}^{\frac{T}{2}} \frac{Ey^2}{2\rho^2}\, dy = \frac{ET^3}{24\rho^2} \tag{6}$$

From Equations 4 and 6 for flexural rigidity and bending energy, governing parameters for engineering mechanical conformability of e-skin can be derived. Only E and T can change the flexural rigidity and bending energy for

a fixed ρ. In other words, mechanical conformability can be constantly and effectively enhanced by reducing the thickness or lowering the elastic modulus of an electronic system. This simple relationship suggests fundamental design rules for researchers who want to develop e-skin with high conformability: (1) Reducing the thickness of a system; (2) Softening the components. The details of each strategy will be explained in the following subsections.

1.2.2 Thickness-Based Conformability

Based on Equations 4 and 6, the most effective way to reduce flexural rigidity and bending energy, thus to improve the mechanical conformability of electronic systems, is to decrease the total thickness of an electronic system. In particular, decreasing a system thickness down to a few micrometers enables the system to make highly conformal contact with soft and complex geometries such as human skin (Figure 1.5) [32]. This strategy is powerful in that ultrathin forms of any materials and systems, regardless of their rigidity, can have high conformability. Therefore, it can be facilely applied to conventional thin film-based electronic devices and their fabrication methods without compromising their advantages, especially performance and device density. The simplest method to realize such ultrathin systems is to fabricate devices with thicknesses under a few hundreds of nanometers on plastic substrates several micrometers thick by conventional deposition techniques

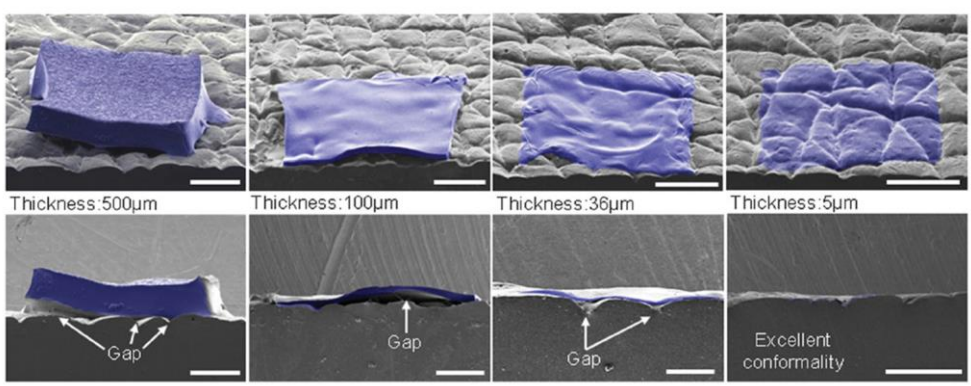

Figure 1.5 | Angled and cross-sectional SEM images showing degree of conformal contact between a silicone replica of the surface of the skin (grey) and various thicknesses of elastomer membrane substrates (blue) [32].

such as chemical vapor deposition, sputtering, and solution processes. Representative examples include touch sensors with thin-film transistor (TFT) arrays on ultrathin polyimide (PI) substrates [7], ultrathin organic photovoltaic systems [8], and ultraflexible organic light-emitting diodes (OLED) with thin-film passivation layers [9]. All of these ultrathin devices have total thicknesses < 3 μm, showing excellent conformability on various complex and time-dynamic surfaces due to their extremely low flexural rigidity. Pioneering researchers, otherwise, directly laminated ultrathin silicon-based devices on human skin, activating a variety of functionalities for health monitoring, medical treatment, and advanced human-machine interfaces [1,17,32]. These devices are interconnected by several-micrometer-thick serpentine inorganic ribbons that not only enable conformable lamination but also allow the system to respond to elastic deformation of human skin. Figure 1.6 summarizes the aforementioned examples of ultraflexible devices [7-9].

A significant additional advantage of an ultrathin design is that the mechanical durability of electronic devices under deformation is significantly improved. Because the bending strain is linearly proportional to the distance from the neutral plane as in Equation 1, when the thickness of the substrate decreases, the strain applied to the devices on the substrate decreases as well, significantly reducing the possibility of electrical failure. For example, minimum bending radii for a tensile strain at the surface not exceeding 5% are ~100 μm for a 10-μm-thick substrate but 10 μm for a 1-μm-thick substrate. It was reported that the TFT-based electronic system on a 1-μm-thick plastic foil withstood cyclic bending with a bending radius of 5 μm [7]. Furthermore, ultrathin electronics can be readily reconfigured to have stretchability by

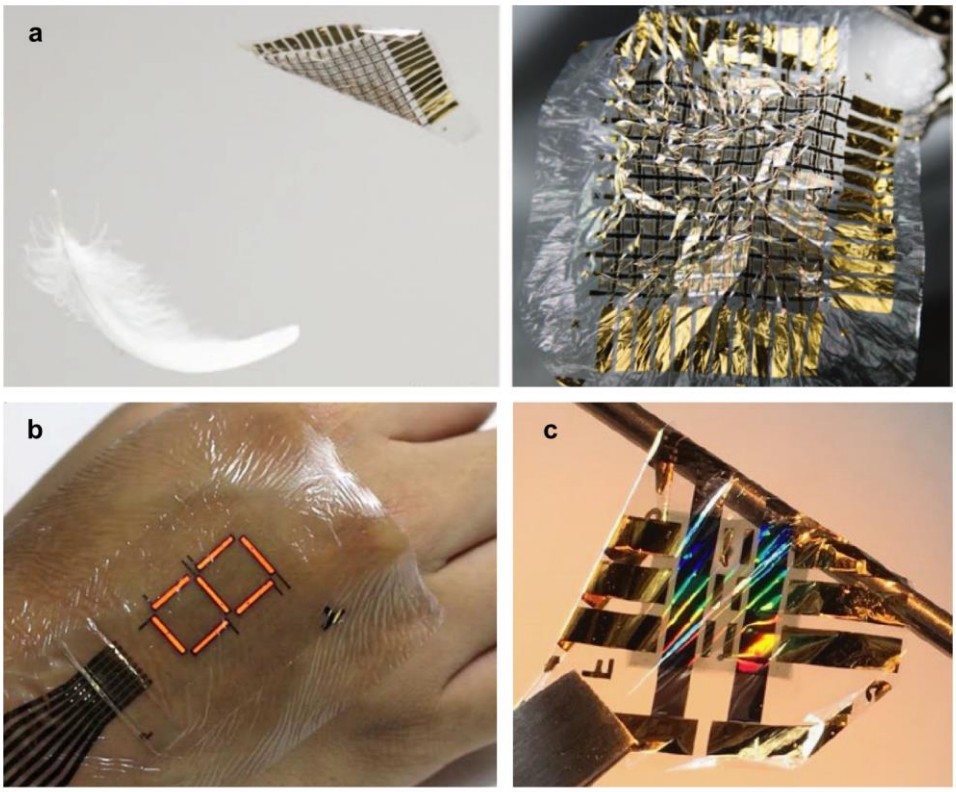

Figure 1.6 | Summary of ultraflexible devices. a, Touch sensors with TFT arrays on ultrathin PI substrates [7]. **b**, Ultraflexible OLEDs with thin-film passivation layers [8]. **c**, Ultrathin organic photovoltaic systems [9].

laminating them on pre-stretched elastomers. When the elastomers are compressed to the initial state, wrinkles that can accommodate tensile strain up to the pre-strain value form throughout the ultrathin systems (Figure 1.7) [7]. Due to their excellent mechanical reliability, ultrathin devices can endure the bending and releasing in the high-aspect-ratio sinusoidal wrinkles, providing opportunities to implement high-performance stretchable electronics such as stretchable displays and TFT arrays.

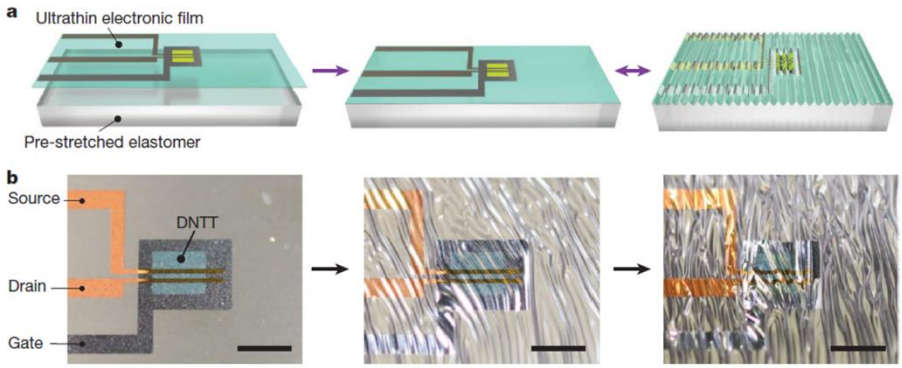

Figure 1.7 | Stretchable electronics using ultrathin devices [7]. a, Schematic illustration of stretchable ultrathin electronics. **b**, Sequential images of the formation of wrinkles in an ultraflexible transistor when the elastomer is released.

Although the thickness engineering strategy offers facile implementation of high-performance e-skin with a bunch of advantages, such as high conformability, mechanical durability, and process compatibility, it has a number of technical challenges to overcome. For example, an ultrathin design inherently brings about a thin-film passivation issue that has been one of the toughest challenges of long standing. Moreover, there is a large portion of electronic devices, whose thickness is difficult to decrease. For instance, in the case of thermoelectric generators that are promising energy harvesting sources for self-powered wearable electronics, their thickness cannot be constantly reduced because they require a sufficient thickness for retaining a thermal gradient. Miniaturization of optical and power systems is also challenging because downscaling such devices causes significant degradation in performance.

1.2.3 Softness-Based Conformability.

Another strategy to improve the mechanical conformability is to soften electronic components. This lowers the effective elastic modulus of the entire system and results in a decrease in flexural rigidity. Soft electrical devices designed for the improvement of mechanical conformability need to meet the following conditions: (1) low young's modulus of the device itself; (2) maintenance of the electrical properties under elastic deformation, especially tensile strain. In this regard, electronic devices in this regime definitely differ from stretchable electronics simply using structural approaches. For example, electrical circuits using spring-like rigid electrodes would be stretchable, but they might not be conformable due to their high Young's modulus. Therefore, the scope of this strategy is limited to "intrinsically stretchable" or equivalently "intrinsically soft" electronic devices that have low Young's modulus comparable to those of elastomers as well as the ability to maintain their electrical properties under tensile strain. Methods realizing such electronic devices are dominated by exploring novel soft materials or engineering materials in molecular and nano-/micro-scale levels. In the rest of this section, representative methods are introduced, and the pros and cons of these strategies are discussed.

Liquid metals have attracted considerable attention of researchers on the field of e-skin, due to their unique mechanical properties, such as shape-reconfiguring without electrical failure and self-healing *via* agglomerating. When reversible and elastic deformation is enabled by passivating them with elastomeric frames, they could be employed as intrinsically stretchable electrodes that can maintain their electrical conductivity under extreme

deformation [33-35]. Therefore, high conformability can be achieved by liquid metal-based electrodes. More interestingly, 3D stretchable circuits with liquid metals can be implemented *via* additive manufacturing technologies [36]. However, despite these attractive characteristics and potentials for highly stretchable electronics, their deleterious and unstable nature poses various technical issues and limits their designs and applications. For instance, direct interfaces between human skin and liquid metal-based electrodes are generally not available due to their liquid phase, precluding their bio-applications.

Researchers have developed another essential building block for realizing intrinsically stretchable components, *i.e.*, composites, by combining elastomer matrices and inorganic fillers. The composites simultaneously inherit mechanical properties from elastomers and electrical properties from inorganic materials, realizing soft forms of electrical devices. Especially, the composites for stretchable electronics require connected networks of inorganic fillers, *i.e.*, percolation paths, whose connection is maintained even when strained [37,38]. Unlike liquid metal-based electronics where the material choice and applications are extremely limited, composites can provide numerous electrical functionalities from plenty of combinations of elastomers and inorganic fillers. For instance, while silver nanowire (AgNW) networks embedded in elastomers are employed for intrinsically stretchable electrodes [39], zinc oxide (ZnO_2) nanowires embedded in elastomers can be exploited for stretchable ultraviolet (UV) detectors [40]. A variety of fillers (*e.g.*, nano-/micro-particles [41], carbon nanotubes (CNT) [42], and metal/metal oxide nanowires [39,40]) and matrices (*e.g.*, silicon rubbers [43], fluorine rubbers [44], and hydrogels [45]) are exploited to produce unique

electrical properties and mechanical properties, respectively, in meaningful applications (*e.g.*, displays [46], soft sensors [38], and energy textiles [47]). In particular, magnetic composites where the magnetic particles in elastomers are self-assembled by the magnetic field provide promising solutions for intensive percolation and facile patterning of fillers [41,48,49]. Most recently, other novel material designs in nanoscale have been considered as promising candidates for intrinsically stretchable systems. Inspiring works using nanoconfinement of conductive or semi-conductive polymers have significantly reduced their elastic modulus and thus improved the stretchability of electrodes and semiconductors without changing their electrical performances [4,5,50].

Figure 1.8 summarizes the examples mentioned above. Intrinsically soft devices enable not only conformal but also “adhesive” contact with 3D surfaces. Their elastic surfaces provided by rubbery matrices enhance the adhesion between electronics and target surfaces, significantly improving the signal transfer and its fidelity. Softness-based conformability enhancement could be powerful in areas where the system thickness cannot be sufficiently reduced. However, the integration of intrinsically soft devices into complex systems is still in its infancy. Furthermore, instability and viscoelasticity of rubbery matrices cause numerous technical issues to be overcome, such as low performance, slow response, and poor cyclic reliability.

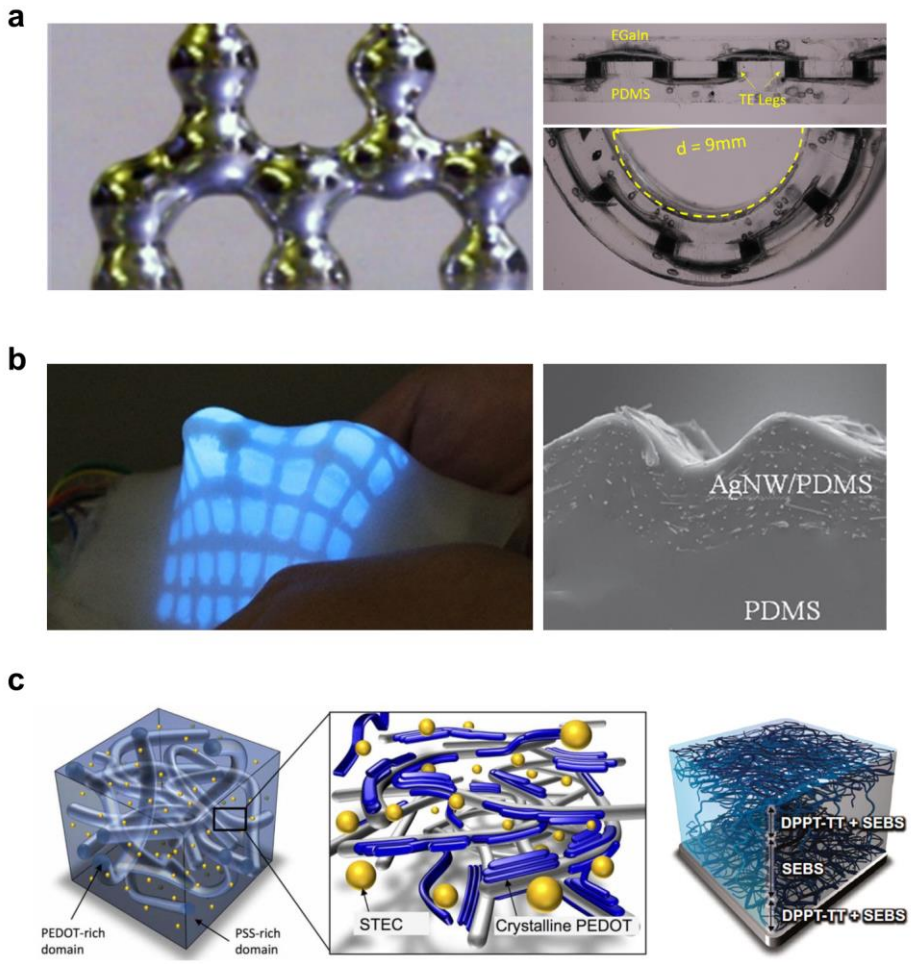

Figure 1.8 | Summary of intrinsically soft electronics. a, Liquid-metal-based devices [33,35]. **b**, Composite-based devices [39,46]. **c**, Novel material designs [4,50].

1.3 Conformability for Enhanced Signal/Heat Transfer in Wearable Sensors and Energy Devices

In wearable sensors and energy devices, which are essential building blocks for skin-like functionalities and self-power generation in wearable electronics, various forms of mechanical stimuli and energy such as heat are transferred from time-dynamic environments through numerous geometries and electrical devices. Therefore, the enhancement of the signal/heat transfer is of great importance in these devices in that it could significantly improve the signal fidelity or energy conversion efficiency. The mechanical conformability potentially enhances the signal/heat transfer by providing conformal geometries with the 3D sources. However, while enhancement of electrical fidelity *via* ultraflexible or intrinsically stretchable devices have been widely investigated, studies on their effect on the transfer of other mechanical signals and heat remain in their early stages. Furthermore, because active materials and their designs in sensors and energy devices have been optimized to maximize their performances, it is challenging to develop ultrathin or soft forms of active layers without compromising their performances. Therefore, careful and comprehensive approaches for conformability enhancement according to the unique properties of each device are required. In this section, two representative and essential wearable devices in these fields, *i.e.*, pressure sensors and thermoelectric generators, where limited conformability significantly have impeded signal/heat transfer are discussed, and there follow potential solutions for effectively improving conformability and its expected effect on signal/heat transfer.

1.3.1 Conformability for Spatial Signal Transfer in Pressure Sensors

For a tactile functionality of conformable e-skin, pressure sensors need to be readily integrated into the systems without reducing their conformability, *i.e.*, ultraflexibility or intrinsic softness. In this regard, many research groups have reported flexible and soft pressure sensors with their creative approaches [10-12,51]. However, soft pressure sensors employing composites of conductive fillers and rubbers usually suffer from low sensitivity, slow response time, and significant hysteresis due to the mechanical instability and viscoelasticity of the rubber matrices [21,52]. Alternatively, flexible pressure sensors show acceptable sensor performances [53-63]; however, the flexibility remains considerably low, *i.e.*, they are not highly conformable but merely bendable. It is due to their relatively thick sensing layers comprising complex microstructures, whose deformation under applied pressure changes resistance or capacitance. These bulky microstructures not only impede the direct integration of the sensing layers into conformable systems but also result in a slow response time and narrow working range with poor linearity.

Furthermore, such thick and inhomogeneous sensing structures could significantly distort the applied spatial pressure. Unlike other stimuli, the contact pressure is exceptionally vulnerable to geometries of receptors. For example, suppose that a contact object with a complex surface makes contact with a top surface of a thick sensing film, as depicted in Figure 1.9. The contact pressure should be transferred to the bottom surface of the sensing film, where the transduction of the spatial signal is actually performed. However, the spatial details of the contact pressure cannot be transferred to the bottom surface because the thick film cannot conform to the surface

morphology of the contact object (Figure 1.9a). On the other hand, an ultrathin and homogeneous sensing film may perfectly conform to the surface of the contact object and transfer the contact pressure with high spatial fidelity to the target surface (Figure 1.9b). In this regard, novel designs and methodologies for realizing ultrathin tactile sensing layers capable of transferring high-fidelity signals (spatial pressure distribution in this case) are highly required.

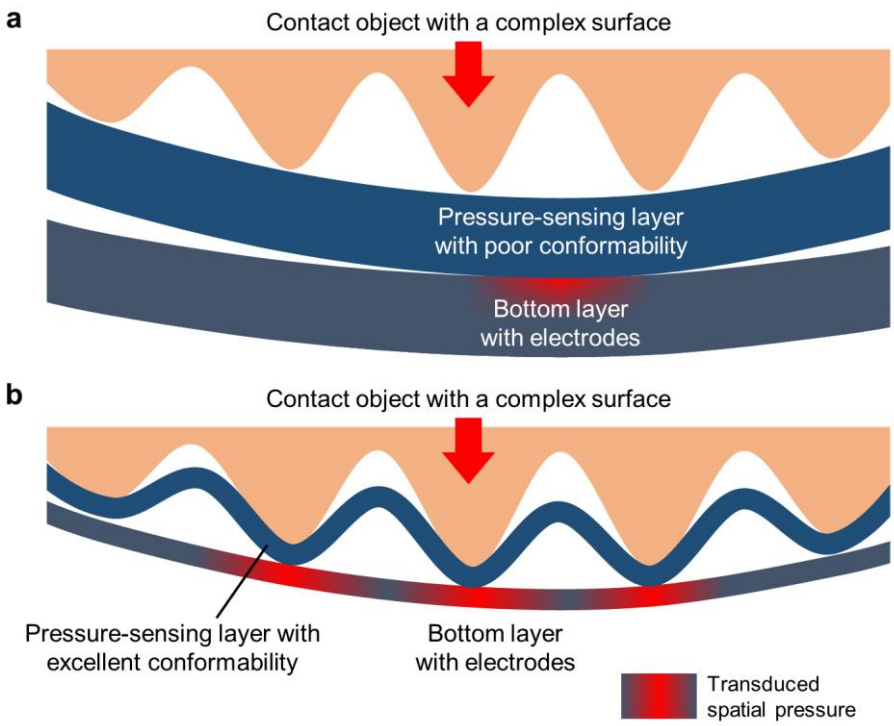

Figure 1.9 | Distortion in spatial pressure due to the thick sensing film. a and **b**, Schematic illustration of the spatial pressure transduced by pressure sensing films with poor (**a**) and excellent (**b**) conformability.

1.3.2 Conformability for Heat Transfer in Thermoelectric Generators

Thermoelectric generators (TEGs) have been regarded as one of the promising energy harvesters for self-powered wearable electronics, due to their ability of continuous power generation from body heat. Therefore, efforts to realize flexible and stretchable TEGs that could harvest thermal energy from 3D surfaces have been widely made [64-73]. However, flexible or soft TEGs based on organic thermoelectric (TE) materials are still in their infancy due to their much lower performance compared to inorganic TE materials. Meanwhile, an elastomeric body with rigid skeletons of inorganic TE legs and metal-based interconnections provides a certain degree of flexibility without compromising the high performance of inorganic TEGs [28,65-67]. However, they showed unexpectedly poor TE performances on 3D heat sources due to the parasitic heat loss in high-thermal-impedance polymer substrates and undesirable air gaps arising from limited mechanical conformability of rigid skeletons (Figure 1.10a). In other words, conformal and adhesive interfaces between TE materials and 3D heat sources with low thermal impedance are highly required to enhance heat transfer to the TE materials, and consequently, TE performance on 3D surfaces. However, as aforementioned, it is challenging to apply thickness-based conformability enhancement strategies to TEGs because they require a sufficient thickness to retain a thermal gradient. Therefore, strategies for softening such rigid skeletons such as metal-based interconnections, thereby enhancing conformability of wearable TEGs will play a critical role in this area (Figure 1.10b).

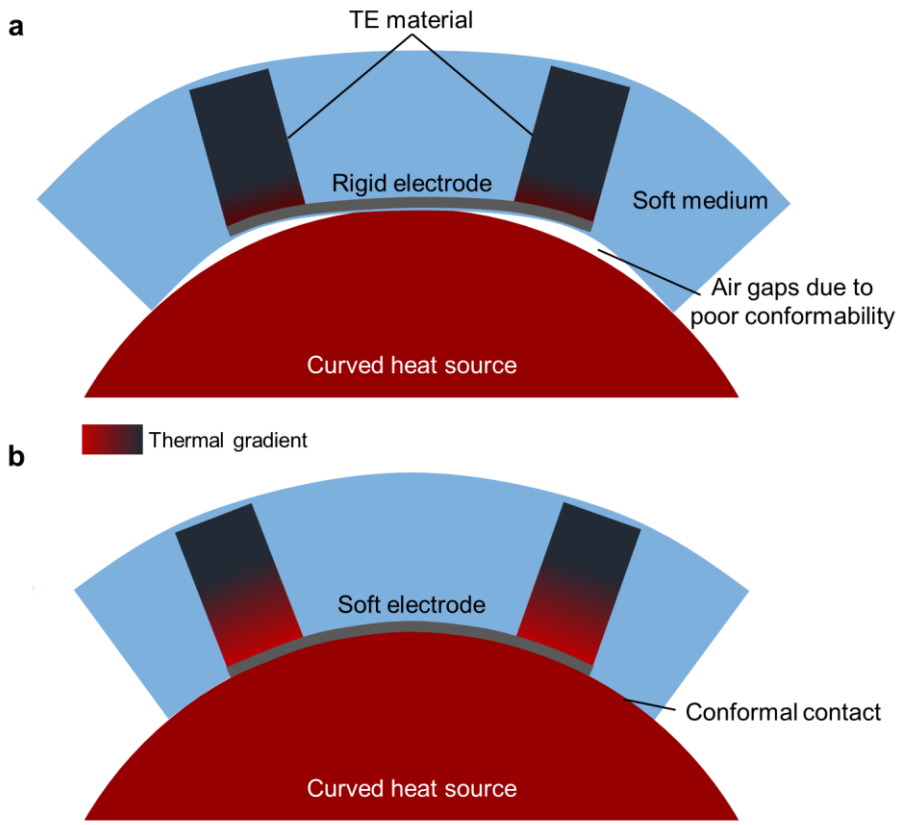

Figure 1.10 | Heat transfer impeded by the rigid electrodes. a and **b**, Comparison of the heat transfer in two wearable TEGs using rigid electrodes (**a**) and soft electrodes (**b**), respectively.

1.4 Motivation and Organization of This Dissertation

In this dissertation, to augment the functionalities of wearable sensors and energy devices, comprehensive studies on conformability enhancement *via* composite materials and its effect on signal/heat transfer, especially in pressure sensors and TEGs, are conducted. As explained in Section 1.3, to improve the conformability of a specific electronic device, a solution needs to be carefully optimized, taking account of the structure, characteristics, and potential advantages of the device. Therefore, in this dissertation, the most suitable one between thickness- and softness-based strategies for each device is first chosen. According to the selected strategy, appropriate designs, materials, and methods, especially exploiting composites, are developed. As a result, the mechanical conformability of each device is significantly enhanced, improving signal/heat transfer and consequently augmenting its functionalities, which have been considered as tough challenges in each area. The effect of the enhanced conformability on signal/heat transfer is systematically analyzed *via* a series of experiments and a finite element method (FEM). There follow demonstrations in the forms of wearable electronics to show the feasibility of the proposed strategies. In summary, a process to enhance the conformability of each device consists of (1) *choosing a strategy for conformability enhancement*, (2) *enhancement of signal transfer through the improved conformability*, (3) *augmented functionality*, and (4) *demonstration*. The details are as follows:

For wearable pressure sensors to capture high-spatial-fidelity pressure distribution, ultrathin piezoresistive layers are developed using cellulose/nanowire nanocomposites (CNNs) (*thickness-based strategy*). The

unique nanostructured surface morphology of the nanocomposite enables unprecedentedly high sensor performances such as ultrahigh sensitivity, great linearity over a wide working range, and a fast response time without thick microstructured sensing layers. Because the ultrathin pressure sensor can perfectly conform to contact objects, it can transduce pressure distribution with high spatial fidelity into conductivity distribution in a continuous domain (*enhancement of signal transfer*). When integrated with an ultrathin quantum dot-based electroluminescent film, the transferred high-resolution pressure distribution is directly visualized without the need for pixel structures (*augmented functionality*). A couple of demonstrations are shown, including real-time smart touch interfaces that can identify the user as well as touch force and location (*demonstration*).

As a solution for low TE performance of wearable TEGs on 3D surfaces due to their limited conformability, an intrinsically soft heat transfer and electrical interconnection platform (SHEP) is developed (*softness-based strategy*). The SHEP comprises an elastomer matrix in which AgNW networks for stretchable electrodes and magnetically self-assembled metal particles for soft thermal conductors (STCs) are embedded. The stretchable electrodes effectively lower flexural rigidity, and the STCs significantly enhance the heat exchange capability of the elastomer, maintaining its softness. As a result, soft TEGs with SHEP can make unprecedentedly conformal contact with 3D heat sources, thereby improving the heat transfer to the TE legs (*enhancement of heat transfer*). The improved heat transfer results in significant enhancement of TE performance on 3D surfaces (*augmented functionality*). Self-powered wearable warning systems

indicating an abrupt temperature increase with light-emitting alarms are demonstrated to show the feasibility of this strategy (*demonstration*).

This dissertation consists of six chapters, including Introduction and Conclusion. Chapter 1 briefly describes recent progress in wearable electronics and e-skin. As a key form factor that differentiates e-skin from other wearable electronics, mechanical conformability is introduced, and two representative wearable devices where lack of conformability have significantly impeded signal/heat transfer are discussed.

Chapter 2 introduces a CNN for ultrathin contact-resistance-based pressure sensors. A facile method using water-based ink is developed and described. The morphology and basic electrical and mechanical characteristics of the CNN are investigated. Furthermore, the performances of pressure sensors using CNNs are characterized, and the reason why the extremely superior performance, including extremely high sensitivity and wide working range, can be achieved without thick sensing layers is discussed.

Chapter 3 presents a novel ultraflexible electroluminescent skin that can visualize pressure distribution with high spatial fidelity. The methodology, morphology, and basic electrical characteristics of the electroluminescent skin are investigated. Especially, the superior spatial fidelity of the visualized pressure distribution enabled by the CNN-based ultrathin sensing layer is systematically analyzed *via* a series of experiments and a finite element method (FEM). Practical applications such as real-time smart touch interfaces are demonstrated to show the feasibility of the CNN and electroluminescent skin.

Chapter 4 introduces a SHEP for soft skeletons of wearable TEGs. Because the SHEP comprises two types of patterned fillers in an elastomer

matrix, the optimization of the method for facile and reliable implementation is of great importance. Therefore, a large part of this chapter is devoted to describing the optimization of the methodology. The morphology and basic electrical and mechanical characteristics of the SHEP are further investigated. In particular, the softness, electrical conductivity, and heat exchange capability of the SHEP are the main topics of this chapter.

Chapter 5 describes highly conformable TEGs using SHEPs implemented by fully automated integration of TE legs and SHEPs. The mechanical reliability and TE performances of the conformable TEGs are studied. Especially, the effect of the enhanced conformability on the heat transfer and TE performance above 3D surfaces is studied *via* a series of experiments and a FEM. Self-powered wearable systems using the conformable TEGs are demonstrated to show the feasibility of the methodology.

Finally, Chapter 6 summarizes the concepts, technologies, and demonstrations developed in this dissertation. The limitations and issues of this study and recommendations for future directions are also discussed.

Chapter 2

Ultrathin Cellulose Nanocomposites for High-Performance Piezoresistive Pressure Sensors

2.1 Introduction

Flexible and soft pressure sensors generally fall into two categories in terms of their operating principles: capacitive and resistive types. Capacitive type sensors are promising in that their high sensitivity and fast response time [51]. However, they require additional circuits to transform the capacitance signal into voltage and current. Furthermore, they need complicated microstructures for high sensitivity, which impedes the realization of conformable sensors. On the other hand, the resistance type sensors (or piezoresistive sensors) provide resistance, voltage, and current, which are useful and accessible in most applications. They have been developed in two different mechanisms: structure-resistance-based sensing and contact-resistance-based sensing. Structure-resistance-based pressure sensors have engineered structures between electrodes. The structures include rubber composites [21], porous and sponge-like microstructures [11]. When the pressure applied, the

structures are deformed and change their resistance. Although they can be employed as soft pressure sensors, they usually suffer from low sensitivity, slow response time, cyclic degradation, and significant hysteresis due to the mechanical instability and viscoelasticity of the rubber matrices [52]. Contact-resistance-based sensors use the contact resistance between engineered structures and electrodes to measure the applied pressure [53-63]. They show relatively high sensitivity, fast response time, and cyclic reliability compared to structure-resistance-based sensors. This type of sensors can be implemented as flexible pressure sensors; however, the flexibility remains considerably low, *i.e.*, they are not highly conformable but merely bendable. It is because they employ relatively thick and complex sensing layers such as microstructures [61-63], tissue paper [53-55], and sponges [58], whose deformation under applied pressure changes contact resistance between the structure and electrodes. These bulky microstructures result in not only poor conformability but also a slow response time and narrow working range. Furthermore, as described in Chapter 1, such thick and complex sensing layers significantly distort the spatial information of pressure distribution.

This chapter introduces an ultrathin and high-performance contact-resistance-based pressure sensor using CNNs with nanofibrillated cellulose and tellurium-poly(3,4-ethylenedioxythiophene):poly(styrenesulfonate) (Te-PEDOT:PSS) nanowires [74]. The dense 1-μm-thick sensing layer with a unique nanostructured surface morphology enables numerous advantages in sensor performance and mechanical reliability such as extremely high sensitivity, high linearity, wide working range, ultrafast response time, and excellent cyclic stability. The methodologies, morphology, and electrical and mechanical characteristics of the CNN and CNN-based pressure sensors are

described in detail. In particular, the mechanism of the high sensor performance is systematically analyzed in association with the unique morphology of the CNN. This unprecedentedly ultrathin pressure sensor not only facilitates highly conformable electronics but also significantly enhances the transfer of spatial pressure, thus realizing high-spatial-fidelity imaging of pressure distribution, which will be introduced in Chapter 3.

2.2 Experimental Section

2.2.1 Fabrication of the CNNs and Pressure Sensors

Te-PEDOT:PSS nanowires. Te-PEDOT:PSS nanowires were synthesized based on previously reported methods [75]. First, 1 g of L-ascorbic acid was dissolved in 45 mL of deionized water. Then, 1 mL of PEDOT:PSS (Clevios PH1000) solution filtered through a PVDF syringe filter was added to this solution. Subsequently, 0.07 g of Na_2TeO_3 was added to the mixture under stirring. The temperature of the mixture was then increased to 90 °C and maintained for 24 h. Te-PEDOT nanorods were collected by centrifugation of the reaction mixture and suspended in 5 mL of deionized water. The final dispersion had a concentration of 78 mg mL^{-1}. The fabricated Te-PEDOT:PSS nanowires had a length of 1 μm and a diameter of ~10 nm.

Nanocellulose. A homogeneously nanofibrillated cellulose suspension was fabricated and provided by Electronics and Telecommunications Research Institute (ETRI). A 1 wt% aqueous dispersion of cellulose powder (Aldrich) was chemically treated by potassium hydroxide (2 wt%) and sodium chloride (2 wt%) at 60 °C for 2 h to remove lignin and hemicelluloses. After the chemical treatment, the samples were rinsed with DI water until the residues were neutralized. This water slurry was passed 30 times through a high-pressure homogenizer under 1,500 bar (Nano Disperser, Suflux) and finally dispersed in DI water at a concentration of 90 mg mL^{-1}. The cellulose was nanofibrillated with a diameter of 10~20 nm and a length of 1~2 μm.

Water-based ink and CNN deposition. Aqueous dispersions of Te-PEDOT nanowires and cellulose nanofibers were mixed with various volume ratios (30:70, 40:60, 50:50). CNNs were deposited on PI substrates with thicknesses of 50 μm, 12 μm, and 1 μm. Spray-coating of the mixtures was performed onto the PI substrates held at 100 °C using a commercial airbrush at a distance of ~10 cm. Multiple-passes of airbrushing were performed until the desired thickness was reached. The coated substrates were then dried on a hotplate at 100 °C for 30 min to remove residual solvent.

CNN-based pressure sensors. Figure 2.1a shows the structure of CNN-based pressure sensors. For bottom Interdigitated Ag electrodes were deposited onto various substrates, including a glass and PI films 12 μm and 1 μm thick *via* inkjet-printing of nanoparticle-type Ag ink (DGP 40LT-15C, ANP). The total size of the finger electrodes for electrical characterization was 6 × 6 mm^2, and the width and gap of the electrodes were 400 μm and 200 μm, respectively (see Figure 2.1b). The CNN-deposited PI films were then laminated onto the electrode-printed substrates using double-sided adhesive tape. As a result, three types of the CNN-based pressure sensors were fabricated: (1) rigid sensors with 50-μm-thick top PI film and bottom glass substrate, (2) flexible sensors with 12-μm-thick top and bottom PI films, (3) ultraflexible sensors with 1-μm-thick top and bottom PI films.

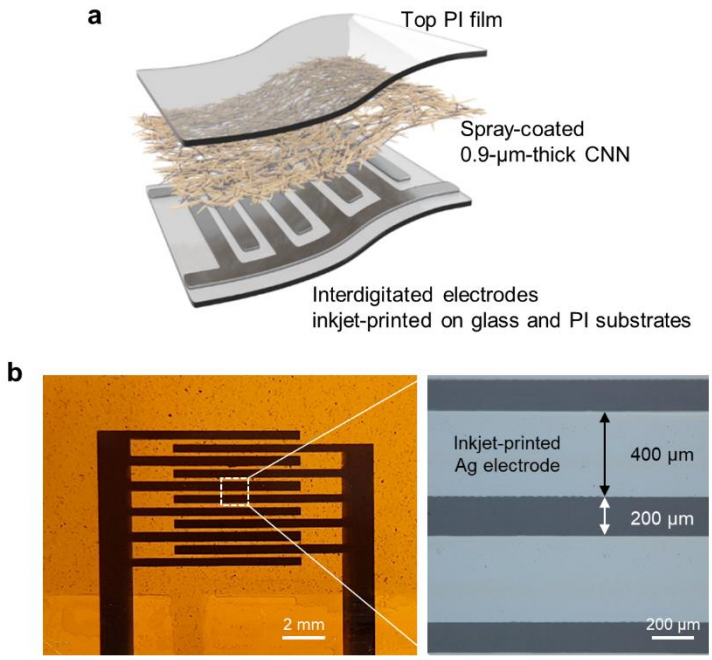

Figure 2.1 | Structure of the CNN-based pressure sensors [74]. a, Schematic illustration of the structure of the CNN-based pressure sensor. **b**, Optical images of the pressure sensors and the inkjet-printed interdigitated electrodes.

2.2.2 Measurements

Electrical and optical characterization. The sheet resistances and transmittances of the CNNs were measured using an ohmmeter with a four-point probe (FPP-RS 8, DASOL ENG) and a spectrometer (DH-2000-BAL, Ocean optics), respectively. The electrical characterization was carried out using Keithley 2400 SourceMeter and Agilent 4155c semiconductor parameter analyzer.

Piezoresistive characterization. Figure 2.2a shows the experimental setup for the piezoresistive characterization of the CNN-based pressure sensors. Static loads and continuous loading and unloading cycles were applied with an automatic force test stand (ASM-1000, a length resolution of 10 μm, Digitech) with a computer controller. For measurement of the pressure response, a 100-μm-thick PDMS buffer was placed between the pressure sensor and the force gauge for uniform pressure application on a precise area. The step-by-step pressures were applied by controlling the motorized z-stage, while measuring the current of the pressure sensor under a bias voltage of 1 V. The time-resolved current data was then converted into the current as a function of pressure (Figure 2.2b). The measurement was repeated more than once, to confirm the stability and reliability of the measurement (Figure 2.2c).

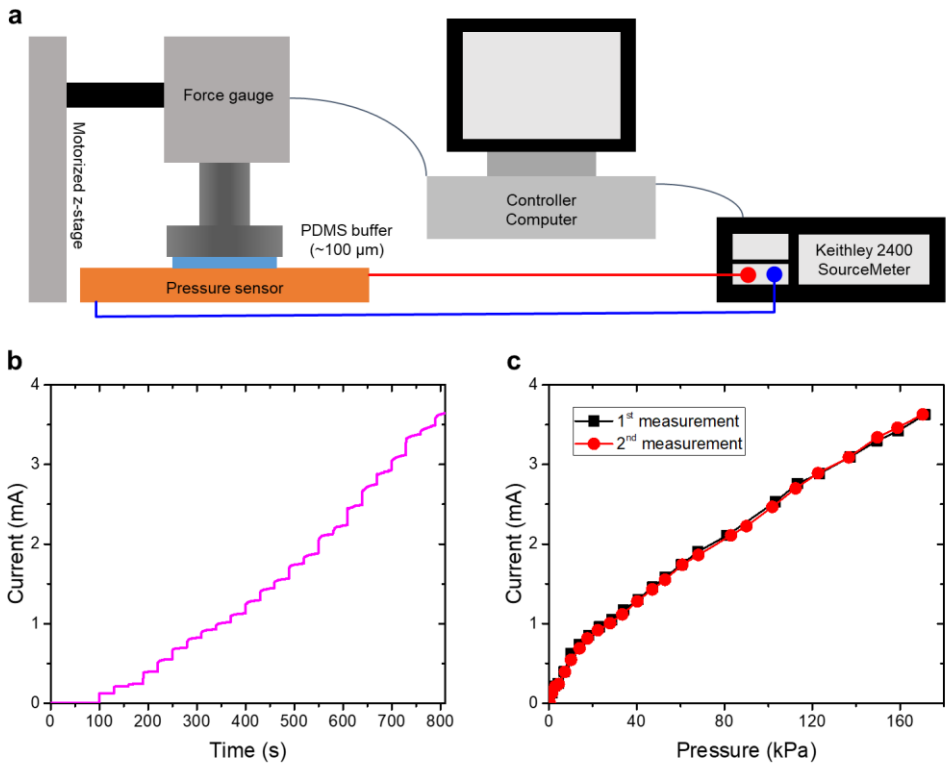

Figure 2.2 | Piezoresistive characterization [74]. a, Schematic illustration of the experimental setup for piezoresistive characterization of the CNN-based pressure sensors. **b**, Time-resolved raw data of the measured current while applying step-by-step pressure. **c**, Reliability and stability of the pressure response of the CNN-based pressure sensor. There is no significant difference between the two repeated measurements.

Response time of the CNN-based pressure sensors. For measurement of the extremely fast response time under a few milliseconds, a sudden change in pressure during no longer than a millisecond is needed. It is difficult to make a sudden change in pressure using the motorized z-stage due to its limited speed. Figure 2.3 explains the abrupt unloading process. The two

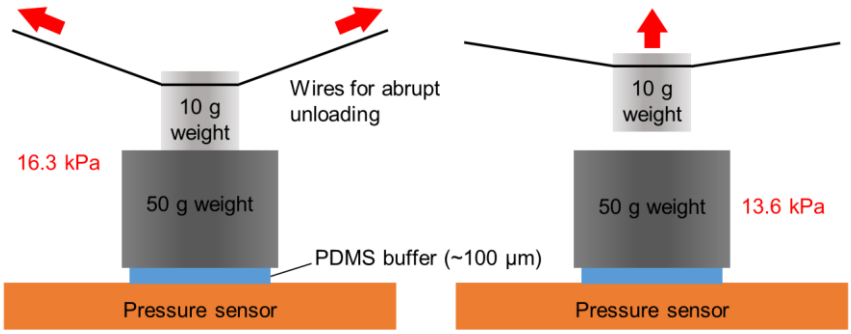

Figure 2.3 | Schematic illustration of an abrupt unloading process for response time measurement [74].

wires were used to unload a 10 g weight from a 50 g weight without undesired friction or touch during the unloading process. The 10 g weight was abruptly removed from the 50 g weight by pulling the two wires in the opposite directions, resulting in a sudden pressure decrease from 16.3 kPa to 13.6 kPa. The current was measured at 480-μs intervals using Agilent 4155c.

Mechanical reliability of flexible pressure sensors. The flexible pressure sensors were bent and folded by a home-made motorized bending machine to investigate the mechanical reliability of them. Specifically, the 25- μm-thick flexible sensor was bent 1000 times with a bending radius of ~1 mm, and the 3-μm-thick ultraflexible sensor was completely folded 1000 times. Before and after the bending cycles, the pressure response of both sensors was measured.

Humidity and temperature durability. To investigate the temperature dependence of the sensor performance, we measured the pressure response of

the sensor while maintaining a specific temperature using a programmable hotplate (Figure 2.4a). To investigate the humidity durability of the CNN-based pressure sensors, we measured the pressure response of the pressure sensor while maintaining a specific humidity using a humidifier and a hygrometer (Figure 2.4b).

SEM and TEM observation. The surface and cross-sectional morphologies of the CNN were examined using a scanning electron microscopy (SEM, FEI Sirion 400, SGC equipment) and transmission electron microscopy (TEM, Tecnai G^2 F30 S-TWIN, FEI). The samples were sliced using a focused ion beam (FIB) system (Dual Beam FIB Nova 200, FEI)

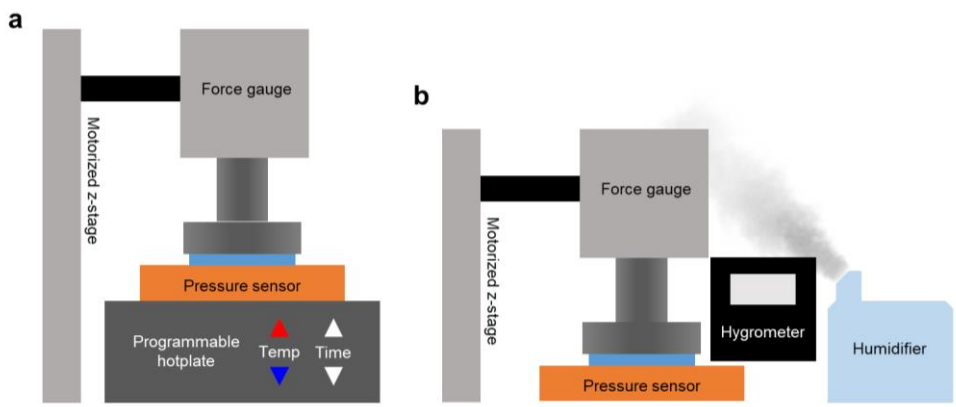

Figure 2.4 | Experimental setup for temperature and humidity dependency of the sensor [74]. a, Schematic illustration of the experimental setup for investigating the temperature dependence of the sensor performance. **b**, Schematic illustration of the experimental setup for investigating the humidity dependence of the sensor performance.

2.3 Results and Discussion

2.3.1 Morphology of CNNs

After fabrication of the aqueous dispersions of Te-PEDOT:PSS nanowires and cellulose nanofibers, the water-based ink for CNNs can be easily obtained by simply mixing the two dispersion. Uniform and ultrathin random networks of the nanowires and the nanofibers were deposited by spray-coating this aqueous mixture. The main advantage of this method is that the electrical characteristics, thickness, and transparency of the CNN can be easily controlled by the volume ratio of the mixture and spraying conditions. First, the morphological characteristics of the CNN were carefully observed. Figure 2.5 shows the morphologies of the fabricated Te-PEDOT:PSS nanowires,

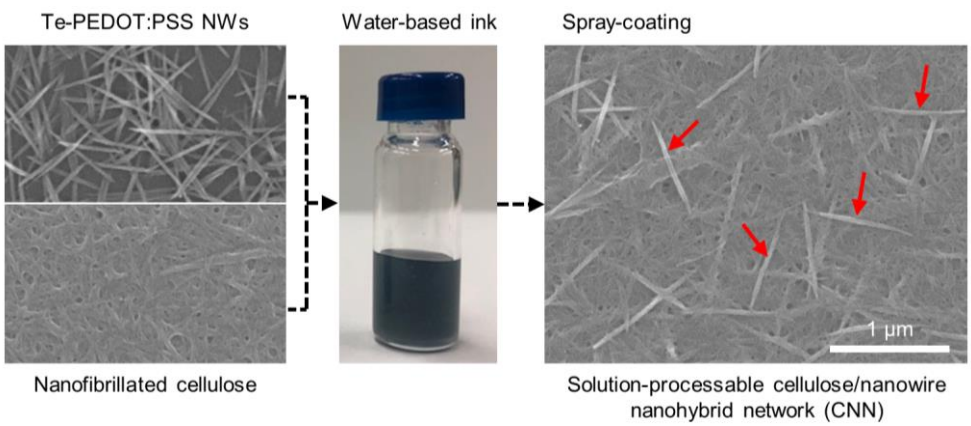

Figure 2.5 | Fabrication scheme and morphology of the CNN [74]. The left SEM images show Te-PEDOT:PSS nanowires and nanofibrillated cellulose, respectively. The middle photograph shows the water-based hybrid ink. The right SEM image shows the spray-coated CNN. Some Te-PEDOT:PSS nanowires are indicated by arrows.

nanocellulose, and CNN. Unlike previous cellulose-based pressure sensors, where microfibers are coated with conductive nanowires [53-56], the CNN features dense cellulose nanofibers encircling each Te-PEDOT:PSS nanowire, forming a nanostructured surface morphology. This nanostructured surface morphology plays critical role in extremely high performances of the CNN-based pressure sensors. Furthermore, the most important feature of the CNN

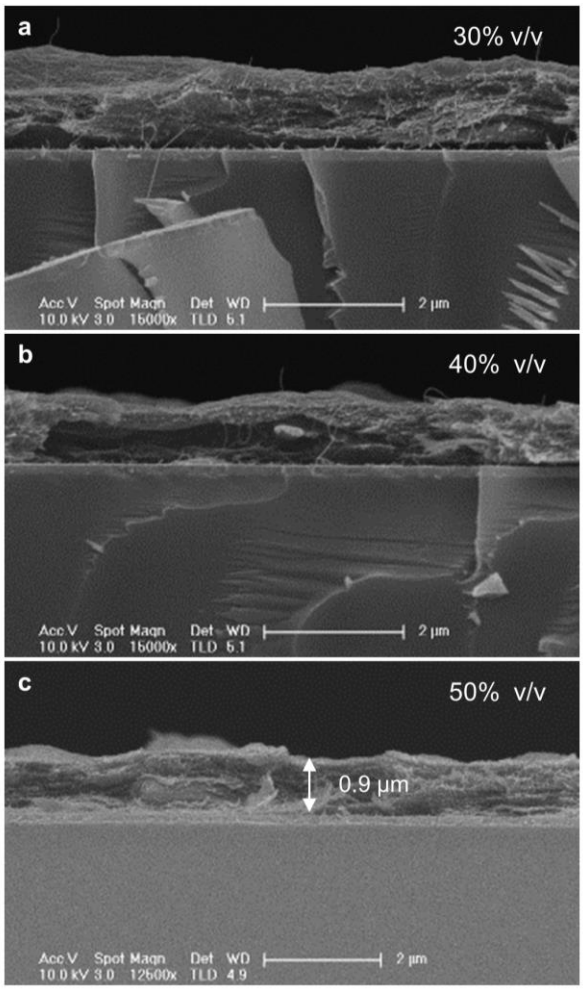

Figure 2.6 | Cross-sectional morphologies of the CNNs [74]. a, **b** and **c**, Cross-sectional SEM images of CNNs prepared using 6 mL of 30% (**b**), 40% (**c**) and 50% v/v ink (**d**).

is that its thickness was under 1 μm, which has not yet been achieved in previously reported contact-resistance-based pressure sensors. Figure 2.6 shows the cross-sectional SEM images of the CNNs deposited by spray-coating of the 6 mL inks with different mixing ratios. As the volume of the nanocellulose matrix decreased, the thickness of the CNN also decreased, and the thickness of the CNN with 50% v/v was ~0.9 μm. The thickness of the CNN can be easily controlled by changing the ink volume. This ultrathin morphology enables additional significant advantages that was not available in previous pressure sensors, such as great transparency and ultraflexibility. Figure 2.7 shows the transmittance of the spray-coated CNN as a function of the sheet resistance. The CNN shows variable transmittance from 60% at 50 kΩ sq^{-1} to 82% at 270 kΩ sq^{-1}.

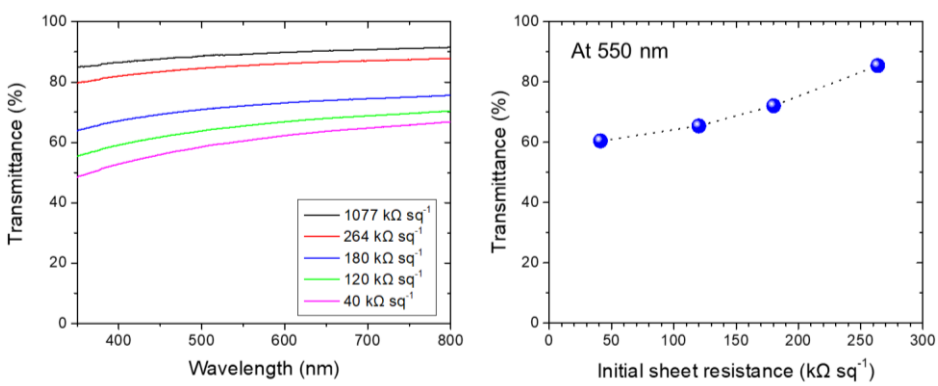

Figure 2.7 | Transmittance of the CNN as a function of sheet resistance [74].

2.3.2 Piezoresistive Characteristics of CNNs

To characterize the piezoresistive performance of the CNN, we fabricated a pressure sensor by laminating a CNN-coated PI film on a glass substrate where interdigitated Ag electrodes were inkjet-printed, as illustrated in Figure 2.1. Figure 2.8 shows a representative pressure response and the sensitivity of the pressure sensor with the 0.9-μm-thick CNN using a 50% volume ratio ink under a bias voltage of 1 V. The experimental details are described in the experimental section and Figure 2.2. The sensitivity is defined as $S = \delta(\Delta I/I_0)/\delta p$, where p denotes the applied pressure, ΔI denotes the current change under the applied pressure, and I_0 denotes the initial current without pressure. The CNN-based sensor showed a large sensing range (> 150

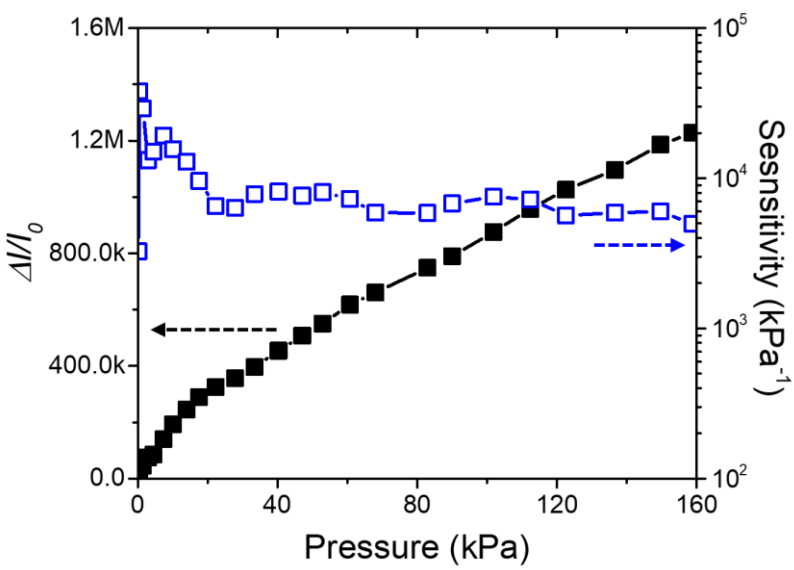

Figure 2.8 | Pressure response and sensitivity of the pressure sensor with the 0.9-μm-thick CNN using a 50% volume ratio ink under a bias voltage of 1 V [74].

kPa), maintaining its ultrahigh sensitivity (> 5000 kPa^{-1}) and high linearity. In the low-pressure regime (< 10 kPa), the sensitivity was > 10000 kPa^{-1}, which far exceeded those of previously reported high-sensitivity piezoresistive pressure sensors. The pressure response of the CNN was easily tuned by changing the volume ratio of the ink while maintaining high sensitivity and linearity. Figure 2.9 shows the pressure response of the CNN-based sensors using three different inks with 30, 40, and 50% v/v. Because the density of the surface-exposed Te-PEDOT:PSS nanowire increased as the volume fraction increased, the current level of the sensor increased. Interestingly, the pressure response of the sensor using the higher volume fraction ink maintained its linearity and working range. We further checked the pressure response of the CNN under higher pressure regime. We measured the pressure response of the CNN-based pressure sensor for a higher pressure

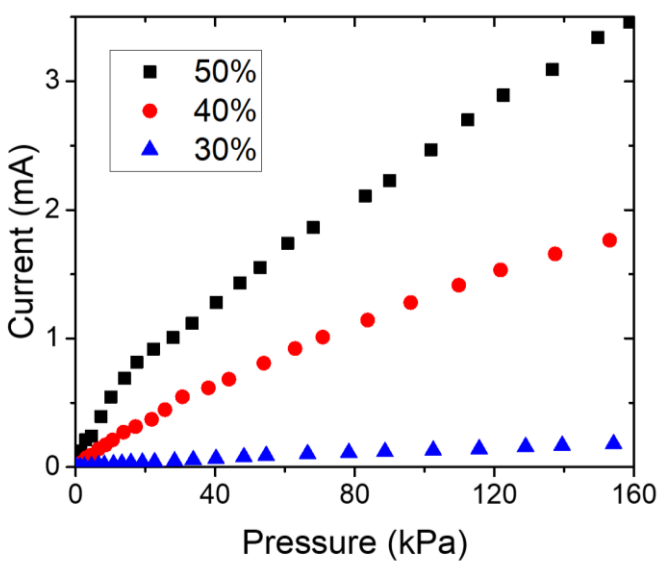

Figure 2.9 | Pressure response of the CNN-based sensors using inks with three different volume ratios (30, 40, 50% v/v) [74].

range up to 1 MPa. Because the upper limit of the force-measuring system is 1 kgf, which corresponds to ~270 kPa in an area of 6 × 6 mm^2 (size of finger electrodes), we had to reduce the pressure-applying area to 3 × 3 mm^2 to apply higher pressure up to 1 MPa. As shown in Figure 2.10, the sensor well responded to the higher pressure maintaining its linearity. Table 2.1 summarizes the performance of piezoresistive pressure sensors [11,53-63,76-78], including CNN-based sensors. It clearly shows that the CNN-based sensors show superior performances compared to ever-reported resistance-type pressure sensors in all categories, including sensitivity, response time, and working range.

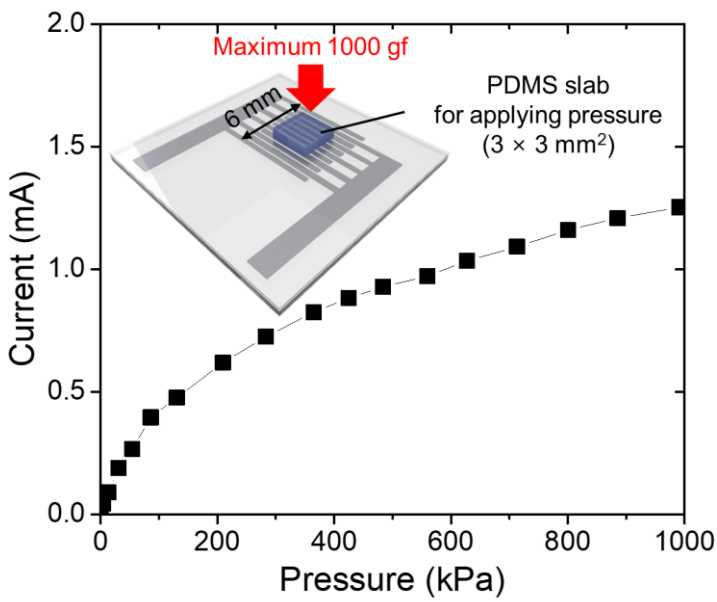

Figure 2.10 | Pressure response of the CNN-based pressure sensor for a high pressure range (up to 1 MPa). The inset illustrates an experimental setup for a high pressure reliability test [74].

Table 2.1 | Performance comparison of piezoresistive pressure sensors [11,53-63,74,76-78].

Reference	Materials and structures	Mechanism	Operating voltage (V)	Sensitivity (kPa^{-1})	Response time (ms)	Detection range (Pa)
[53] (2014)	AuNW/tissue paper	Piezoresistive (cellulose)	1.5	1.14 (< 5000 Pa)	< 17	13 – 5000
[54] (2017)	SWNT/tissue paper	Piezoresistive (cellulose)	0.1	2.2 (35 – 2500 Pa), 1.3 (2500 – 11700 Pa)	35 – 40	< 11700
[55] (2017)	rGO/paper	Piezoresistive (cellulose)		17.2 (1 – 2000), 0.1 (2000 – 20000)	45 – 75	< 20000
[56] (2016)	AgNW/cotton fibres	Piezoresistive (cellulose)		3.4 (< 200 Pa)	< 50	< 1000
[57] (2017)	CuNW aerogel	Piezoresistive (microstructure)		0.7	80	< 200
[58] (2013)	rGO/PU sponge	Piezoresistive (microstructure)		0.26 (< 2000 Pa), 0.03 (2000 – 10000 Pa)		9 – 10000
[11] (2014)	PPy foam	Piezoresistive (microstructure)		7.7 – 41.9 (< 100), 0.4 (> 1000)	50	< 100000
[59] (2017)	Sparkling graphene block	Piezoresistive (microstructure)	0.1	229 (0 – 120 Pa), 26.9 (400 – 1000 Pa)		10 – 1000
[60] (2014)	rGO foam	Piezoresistive (microstructure)		15.2 (< 300 Pa)		165 – 1200
[61] (2014)	PEDOT:PSS/PUD micro-pyramid array	Piezoresistive (microstructure)	0.2	10.3		13 – 8000
[62] (2014)	CNT/PDMS micro-dome array	Piezoresistive (microstructure)		15.1 (< 500 Pa)	40	0.2 – 70000
[63] (2016)	CNT/graphene/PDMS microstructures	Piezoresistive (microstructure)	0.03	19.8 (< 300 Pa)	16.7	0.6 – 6000
[76] (2017)	Carbonized silk nanofibre	Piezoresistive (nanofabric)	0.1	34.47 (0.8 – 400 Pa), 1.16 (400 – 5000 Pa)	16.6	0.8 – 5000
[77] (2019)	AgNW with air gap	Piezoresistive	10	16.1		< 40000
[78] (2018)	Carbonized crepe paper	Piezoresistive (fabric)	1	2.56 - 5.67 (0 – 2530 Pa)	30	0.9 – 20000
[74] (2020)	CNN	Piezoresistive (nanocellulose)	1	> 10000 (< 10000 Pa), ~5000 (10000 – 170000 Pa)	< 1	< 170000

2.3.3 Mechanism of High Sensitivity and Great Linearity

High sensitivity. The superior performance of the CNN-based pressure sensors can be attributed to the unique nanohybrid structure of the CNN (Figure 2.11). From the definition of sensor sensitivity $S = \delta(\Delta I/I_0)/\delta p$, the I_0 is the most important factor for high S, *i.e.*, low I_0 results in high S. Here, a conductive contact area (CCA) is introduced, which denotes a contact area between electrodes and conductive nanomaterials to explain the initial current change of the sensors. As shown in Figure 2.11a, previously reported contact-resistance-based pressure sensors generally feature that the highly conductive nanomaterials decorate cellulose microfibers or engineered microstructures. The high-density conductive materials on the microstructures form a bulky initial CCA, resulting in high I_0 and consequent low S (Figure 2.11b). On the other hand, in the case of the CNN, each Te-PEDOT:PSS nanowire is encircled by the dense nanocellulose, forming a nanostructured surface with low-density Te-PEDOT:PSS nanowires exposed on it (Figure 2.11c). A small initial CCA arising from the low-density surface-exposed nanowires results in an extremely low I_0 and consequent high S (Figure 2.11d). Furthermore, the Te-PEDOT:PSS nanowire has a lower conductivity (~20 S cm^{-1}) [74] than metallic nanowires such as AgNWs and AuNWs, which results in high contact resistance between the nanowires and the printed finger electrodes, contributing to the extremely low I_0.

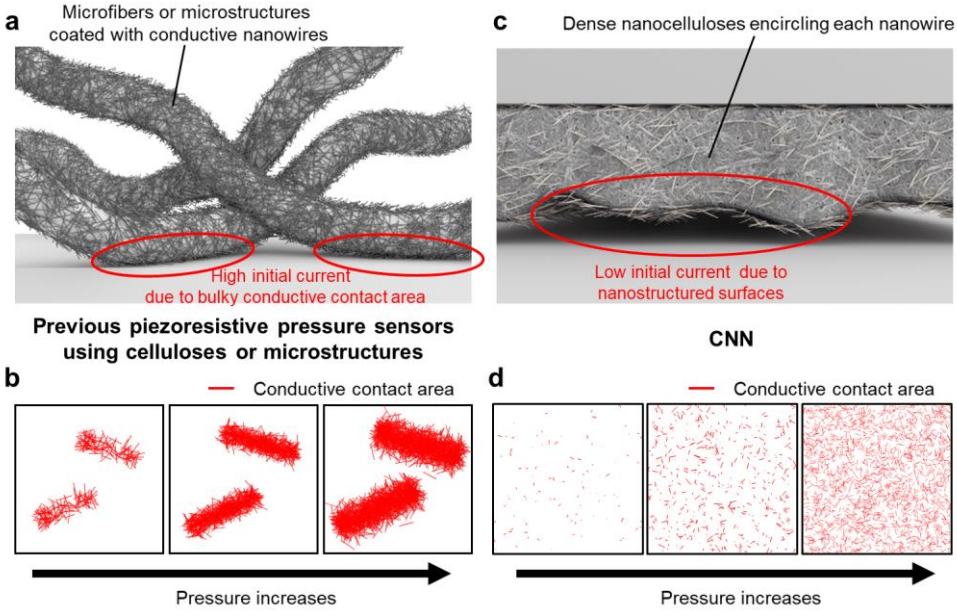

Figure 2.11 | Mechanism of the ultrahigh sensitivity and great linearity [74]. **a** and **b**, Schematic illustration of the structural difference between previous piezoresistive pressure sensors using cellulose or microstructures (**a**) and the CNN (**b**). **c** and **d**, Schematic illustration of the CCA change in previous sensors (**c**) and the CNN (**d**) when pressure is applied.

High linearity over a wide working range. The nanostructured surface with low-density conductive nanowires also contributes to high linearity and a large working range of the CNN. To analyze the current change of previous sensors and CNN-based sensors in the working range, we introduce a resistance model of contact-resistance-based pressure sensors as illustrated in Figure 2.12. In this model, the total electrical conductance as a function of the applied pressure can be defined as

$$G_{\text{total}}(P) = \frac{1}{R_{\text{total}}(P)} = \frac{1}{R_{\text{electrodes}} + R_{\text{film}} + R_{\text{contact}}(P)} \qquad (2.1)$$

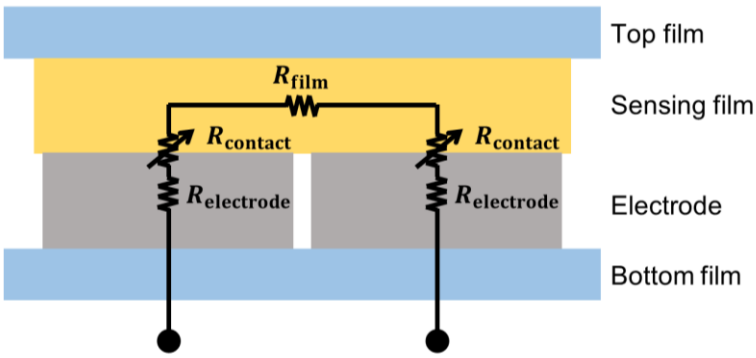

Figure 2.12 | Resistance model of contact-resistance-based pressure sensors.

Here, $R_{electrodes}$ is the resistance of the finger electrodes, R_{film} is the resistance of the sensing film between the electrodes, and $R_{contact}(P)$ is the contact resistance between the sensing film and electrodes as a function of the applied pressure. In most cases, when the pressure is applied, the change of R_{film} is negligible as compared to the change of $R_{contact}(P)$. In particular, the R_{film} of the CNN was not changed when the pressure was applied, due to their dense and ultrathin morphology. Therefore, in this dissertation, R_{film} is assumed constant. If $R_{contact}(P)$ is much higher than $R_{electrodes} + R_{film}$, the total conductance is

$$G_{total} \approx \frac{1}{R_{contact}(P)} = G_{contact}(P) \tag{2.2}$$

In other words, the current of the sensor is totally proportional to the $G_{contact}(P)$. When the $R_{contact}(P)$ becomes sufficiently small compared to the $R_{electrodes} + R_{film}$, after the saturation pressure ($P_{saturation}$) is applied, the total conductance becomes

$$G_{\text{total}} \approx \frac{1}{R_{\text{electrodes}}+R_{\text{film}}} \quad (2.3)$$

which suggests the additional pressure no longer significantly changes the G_{total}. According to these equations, the conditions for high linearity and a wide working range can be inferred as follows:

(1) For high linearity in a linear region ($P < P_{\text{saturation}}$), the $\frac{\delta G_{\text{contact}}}{\delta P}$ should be maintained without significant change throughout the pressure range.

(2) For a wide working range, $R_{\text{contact}}(P)$ should be maintained much higher than $R_{\text{electrodes}} + R_{\text{film}}$ up to a high pressure range.

From these two conditions, it is concluded that for high linearity with a wide working range, the $\frac{\delta G_{\text{contact}}}{\delta P}$ should be a small constant value, maintaining $R_{\text{contact}}(P)$ much higher than $R_{\text{electrodes}} + R_{\text{film}}$. Because the bulky CCA in the microstructure-based pressure sensors results in high $\frac{\delta G_{\text{contact}}}{\delta P}$ when the small pressure applied, the R_{contact} rapidly decreases in a low-pressure regime. Furthermore, the microstructure requires large deformation to further increase the CCA in a higher pressure range. For these reasons, the microstructure-based pressure sensors show a narrow linear region. In contrast, because of the low density of the surface-exposed Te-PEDOT:PSS nanowires and relatively low conductivity of them, $\frac{\delta G_{\text{contact}}}{\delta P}$ can be maintained at a small value in the CNN. In addition, the densely nanostructured surface increases the CCA uniformly and consistently, preventing $\frac{\delta G_{\text{contact}}}{\delta P}$ from diminishing up to a higher pressure range.

2.3.4 Fast Response Time of CNN-Based Pressure Sensors

The response time of the CNN-based pressure sensors was measured by the sudden unloading process described in experimental section and Figure 2.3. The pressure was suddenly decreased from 16.3 kPa to 13.6 kPa, while the current was measured at 480-μs intervals. Figure 2.13 shows the current change during the sudden pressure decrease. The CNN-based pressure sensor well responded to the sudden pressure decrease, and an ultrafast response time of < 1 ms was observed in the three repeated measurements. After each unloading process, oscillation occurred due to the PDMS buffer and was also captured by the pressure sensor, proving the extremely fast response time.

Although contact-resistance-based pressure sensors generally show an improved response time < 100 ms compared to the slow response time of the rubber-based pressure sensors, the CNN-based pressure sensor shows a much faster response time < 1 ms, which have not been observed in the previous sensors (Table 2.1). This fast response time of the CNN arises from the ultrathin design and dense nanohybrid structure. Previously reported pressure sensors generally have thick, microporous sensing layers where bulky deformation occurs in the microstructures when the pressure is applied. For example, in pressure sensors using tissue paper, microscale fibers are bent and strained when the pressure is applied. This micro/millimeter-scale deformation and recovery in the sensing layer affect the response time of the sensor. In contrast, the dense nanocellulose and conductive nanowires form a nanohybrid structure in the CNN whose thickness is < 1 μm. Therefore, the current change arises mainly from the surface-exposed conductive nanowires.

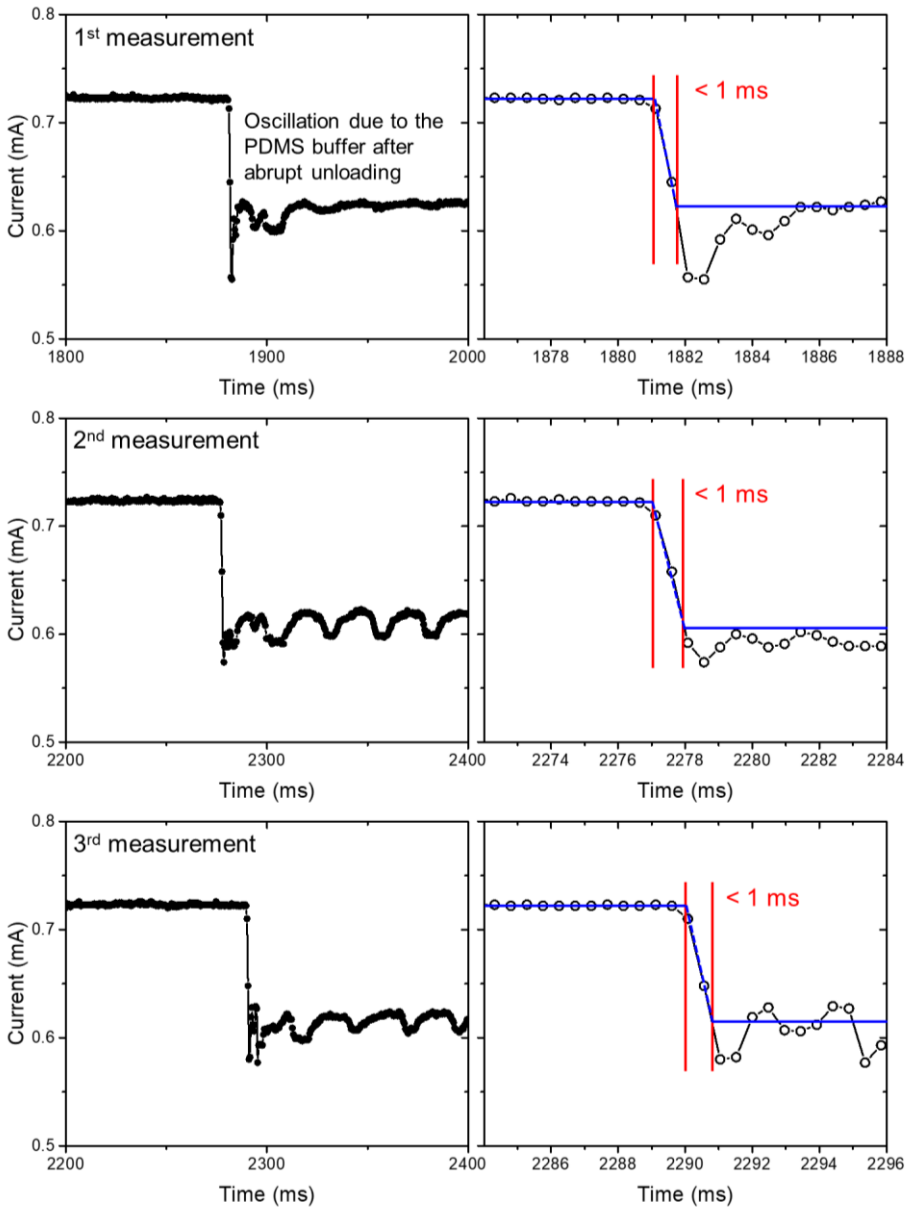

Figure 2.13 | Responses of the CNN-based pressure sensor to the sudden pressure change [74]. The right graphs are the expanded views of the left three measurement results.

Consequently, much smaller deformation occurs even when the high pressure is applied, enabling an ultrafast response and recovery time.

The ultrafast response time of the CNN was further demonstrated by real-time sensing of cell phone vibration. Figure 2.14a shows the experimental configuration for sensing cell phone vibration. A polydimethylsiloxane (PDMS) slab, a 50 g weight, and a cell phone were stacked on the sensor, where an initial pressure of ~55 kPa was applied. Figure

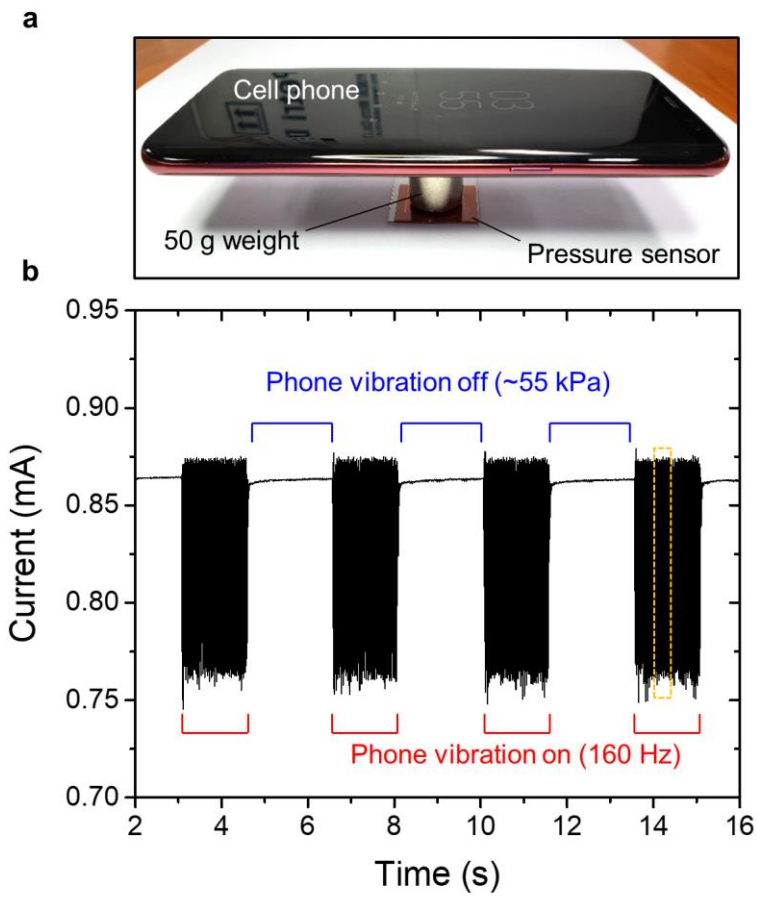

Figure 2.14 | Phone vibration sensing [74]. a, Photograph showing the experimental setup for sensing cell phone vibration. **b**, Sensing result of cell phone vibration (160 Hz) using the pressure sensor.

2.14b presents the vibration sensing results. When the phone vibrated at 160 Hz, the current measured at 480-μs intervals showed a 160-Hz oscillation with peak values of 0.88 mA and 0.76 mA, which correspond to ~60 kPa and ~45 kPa, respectively. Figure 2.15a shows the enlarged view of the yellow box in Figure 2.14b. The graph of the measure current shows a well-defined 160 Hz sinusoidal waveform. The fast Fourier transform of the signal in Figure 2.15b supports that the sensor responded well to the 160 Hz vibration without any sign of damping.

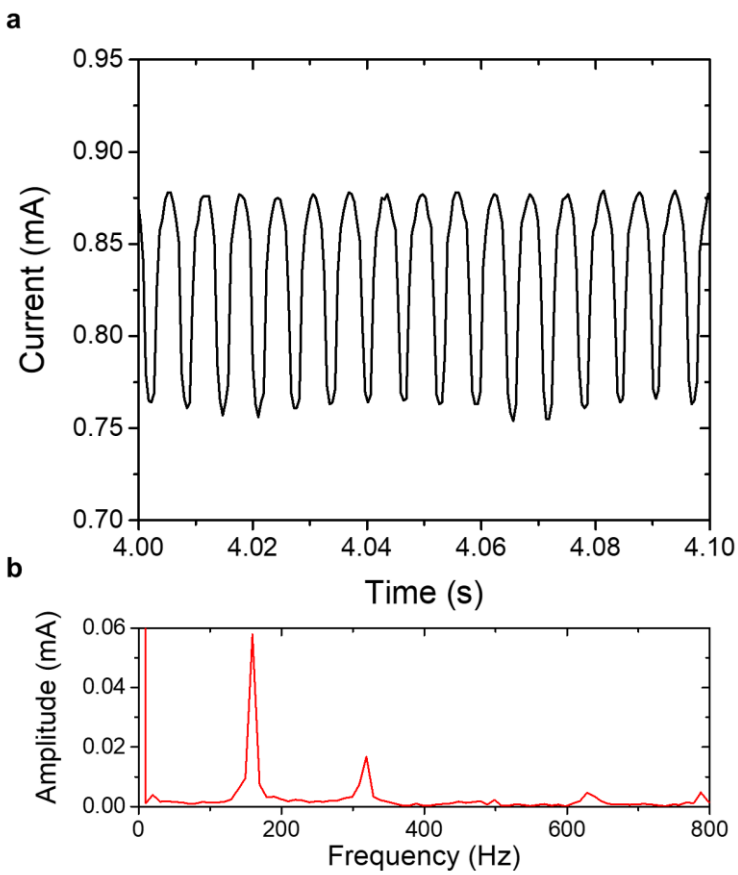

Figure 2.15 | Enlarged view of phone vibration sensing [74]. a, Enlarged view of the yellow box in Figure 2.14. **b**, Fast Fourier transform of the signal in **a**.

2.3.5 Cyclic Reliability of CNN-Based Pressure Sensors

To investigate the cyclic stability of the CNN-based pressure sensors, we applied continuous pressure cycles on the sensor from 0.1 kPa to 120 kPa with a 120 kPa s^{-1} loading rate. Note that the applied cycle condition is extremely harsh as compared to previously reported studies on contact-resistance-based pressure sensors [53-56]. Figure 2.16a shows the current of the sensor during the cyclic loading and unloading process. The CNN-based pressure sensor showed no significant change in the pressure response during and after 10000 loading-unloading cycles, maintaining its low I_0 and high sensitivity. Figure 2.16b presents the enlarged view of the measured current in Figure 2.16a after 4000 cycles, showing the stable and reliable cyclic change. To confirm the cyclic stability of the sensors under a higher pressure

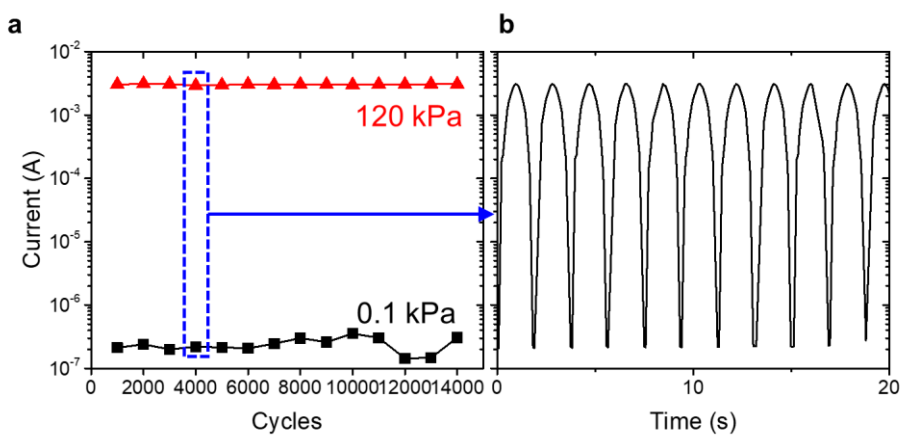

Figure 2.16 | Cyclic reliability of the CNN-based pressure [74]. a, Current of the CNN-based pressure sensor under continuous loading and unloading cycles from 0.1 kPa to 120 kPa. **b**, Enlarged view of the recorded data in **a** after 4000 cycles.

regime, we further measured the cyclic response of the sensor by applying 1000 cycles each for 180 kPa, 500 kPa, and 1 MPa. The sensor showed the cyclic current change corresponding to each pressure without significant degradation during the whole cycle test (Figure 2.17a and b). Figure 2.17c is an enlarged view of the current change during 1 MPa cycles showing great stability and reversibility. Figure 2.18 presents microscope images of the CNN on a PI film containing a boundary of the pressure applying area before and after the whole cyclic test. There was no noticeable damage after the cycle

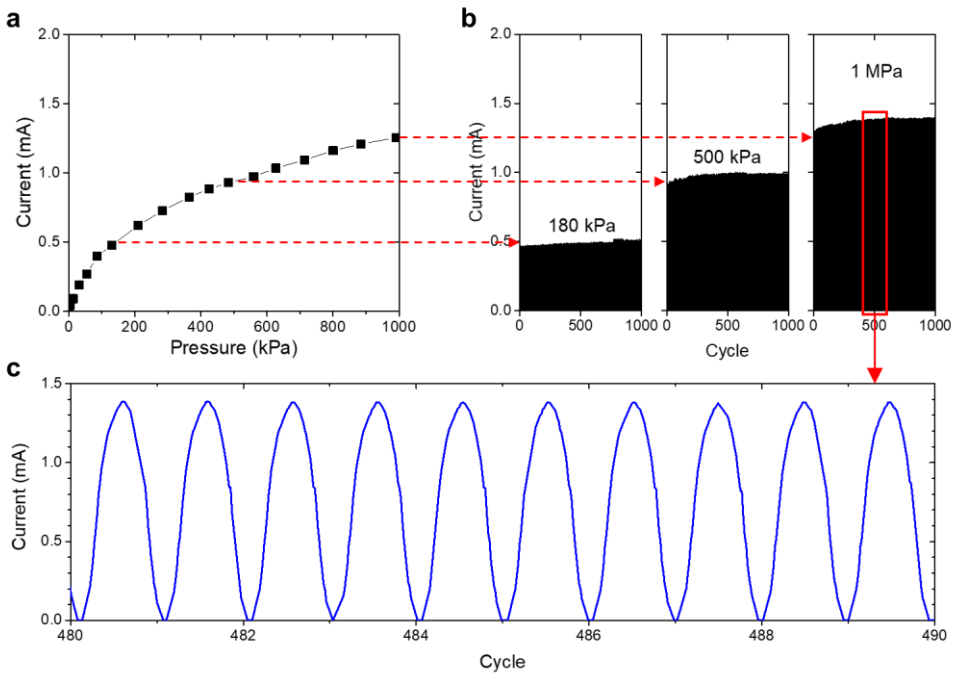

Figure 2.17 | Cyclic reliability under higher pressure [74]. a, Pressure response of the CNN-based pressure sensor for a high pressure range (up to 1 MPa). **b**, Cyclic response of the CNN-based pressure sensor during 1000 cycles each for 180 kPa, 500 kPa, and 1 MPa. **c**, Enlarged view of the cyclic current response during 1 MPa cycles.

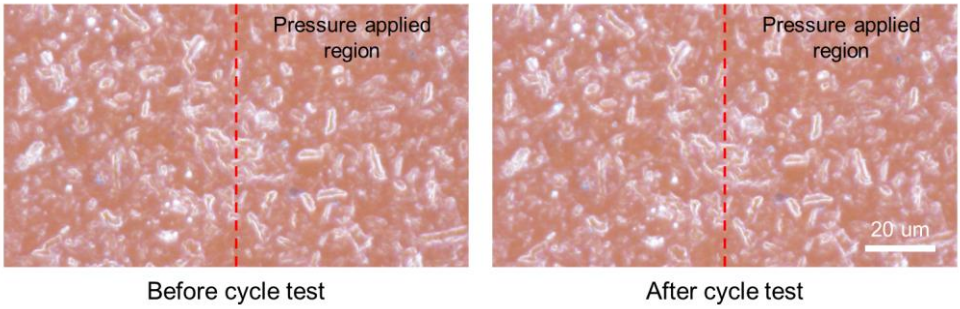

Figure 2.18 | Microscope images of the CNN on a PI film containing a boundary of the pressure applying area before (left) and after (right) the whole cyclic test [74].

test in the pressure applying area. These experimental results show that the CNN-based pressure sensor has great cyclic reliability even under a high-pressure condition. This great mechanical stability and durability of the CNN-based pressure sensor under cyclic stress can be explained by the following three reasons:

First, high Young's modulus of the PI substrate primarily protects the CNN from large deformation. Because the supporting PI film has a high Young's modulus (> 3 GPa), high stress (yield strength of ~100 MPa) is required to irreversibly deform the PI film. This mechanical durability of the PI film primarily prevents the plastic deformation of the CNN from the extreme deformation such as tensile stress.

Second, an ultrathin design reduces the bending strain applied to the CNN. The CNN is ultrathin (< 1 μm) and the thickness of the PI substrate can also be reduced to 1 μm. As many previous works have reported[9-10], this ultrathin design enables high mechanical durability by reducing the bending strain applied to the devices on the substrate. For example, minimum bending

radii for a bending strain not exceeding 5% are ~100 μm for a 10-μm-thick PI film and 10 μm for a 1-μm-thick PI film, respectively.

Third, an ultrathin and dense nanohybrid structure prevents the internal deformation of the CNN. As explained in the previous subsection, unlike earlier pressure sensors that generally have thick and porous sensing layers, the dense and ultrathin morphology of the CNN reduces the possibility of the irreversible plastic deformation when external stress was applied.

2.3.6 Mechanical Reliability and Conformability

The CNN and CNN-based pressure sensors show great mechanical durability due to their ultrathin and dense nanohybrid structure. We investigated the mechanical reliability of the pressure sensor under various deformation conditions using flexible and conformable pressure sensors that have different total thicknesses.

Flexible pressure sensors with a total thickness of 25 μm. A flexible pressure sensor was fabricated by laminating a 12-μm-thick PI film coated with a CNN and another 12-μm-thick PI film where the electrodes are printed, respectively. Therefore, the total thickness of the sensor including the CNN layer is ~25 μm. The sensor with such thickness is mechanically flexible rather than fully conformable to micro-textures due to the relatively thick PI film. The first prerequisite of such flexible sensors is that they have to maintain their performance while and after bending stress is applied. Therefore, a bending cycle test was performed for the 25-μm-thick sensor, and the performance of the sensor was measured before and after the bending cycles. First, the pressure sensor was repeatedly bent and relaxed 1000 times with a bending radius of ~1 mm while the current change was monitored (Figure 2.19a). The current increased up to 2 μA when the sensor was completely bent due to the contact pressure arising from the bending (Figure 2. 19b). This current repeatedly oscillated during the whole bending cycles and it reverted to the initial state after the bending cycles. Figure 2. 19c shows the pressure response of the sensor measured before and after 1000 bending cycles. There was no significant change in the pressure response before and

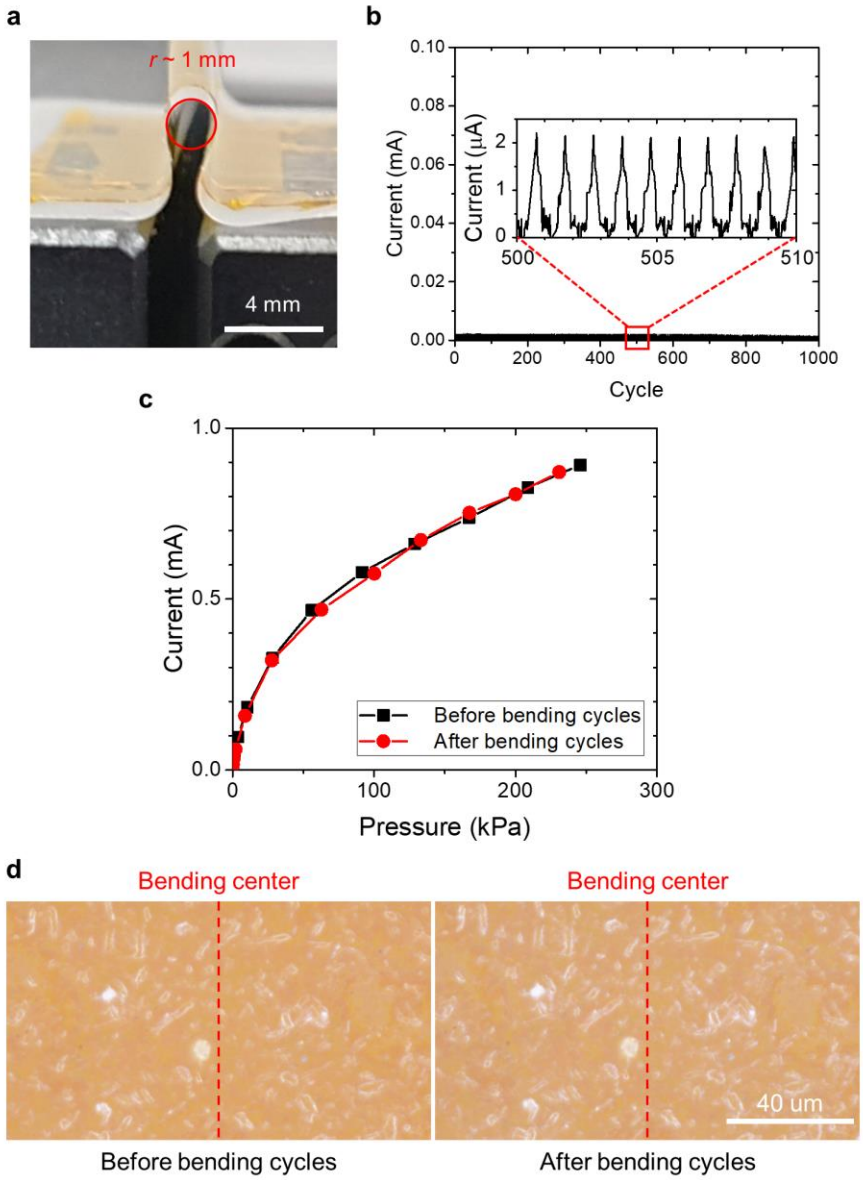

Figure 2.19 | Mechanical reliability of flexible sensors under cyclic bending [74]. a, Photograph of the 25-μm-thick sensor that is bent with a bending radius of 1 mm. **b**, Current change of the 25-μm-thick sensor during 1000 bending cycles with a bending radius of 1 mm. **c**, Pressure response of the CNN-based pressure sensor before and after the bending cycles. **d**, Microscope images of the CNN surface before and after the bending cycles.

after the cyclic bending. Figure 2. 19d presents microscope images of the CNN surface before and after the bending cycles. There was no noticeable damage or delamination of the CNN after the cycle test. We also measured the performance of the sensor after attaching it to a hand replica, to investigate their performance change under a bent state. Optical images in Figure 2.20a show the experimental setup. Figure 2.20b compares the pressure response of the sensor measured on the flat glass and hand replica, respectively. The sensor showed no significant performance degradation on the curved surface. These results reveal that the CNN-based flexible sensors have high mechanical durability under bending stress.

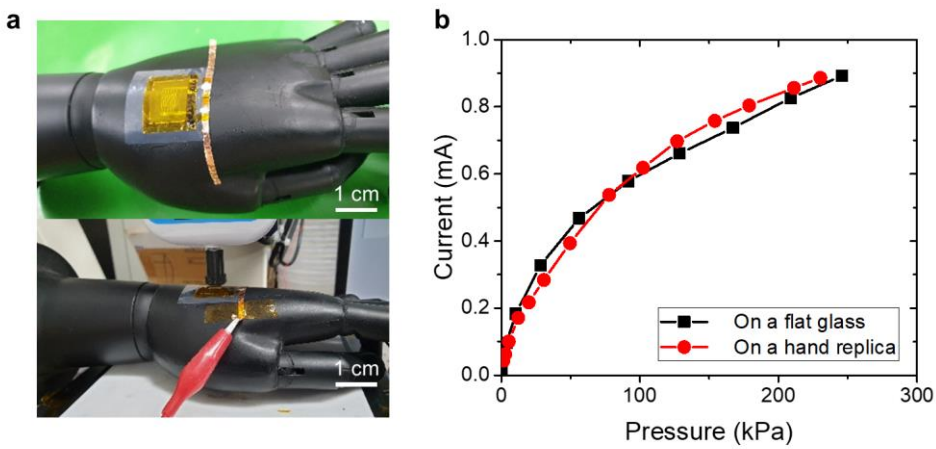

Figure 2.20 | Mechanical reliability of flexible sensors on a curved surface [74]. a, Optical images of the 25-μm-thick sensor attached to a hand replica. **b**, Comparison of pressure response of the 25-μm-thick sensor attached to a flat glass and hand replica, respectively.

Ultraflexible pressure sensors with a total thickness of ~3 μm. An ultrathin pressure sensor was also fabricated by laminating a 1-μm-thick PI film coated with a CNN and another 1-μm-thick PI film where the electrodes are printed, respectively. Therefore, the total thickness of the sensor including the CNN layer is ~3 μm. Optical images in Figure 2.21a shows the ultrathin sensor. It can easily conform to the skin and be crumpled. Figure 2.21b presents an optical image of the ultrathin sensor that is completely folded. Because of the ultraflexibility and high conformability of the 3-μm-thick sensor, it is used to investigate the mechanical durability under harsh deformation conditions such as crumpling and folding. The sensor performance was measured three times, before and after completely folded 1000 times, and crumpled by a hand. Figure 2.21c shows the experimental results. The sensor showed no significant change in the pressure response before and after 1000 folding cycles and crumpling. As shown in Figure 2.22a, the performance of the sensor was further measured when the sensor was conformably attached to the finger of a hand replica. Figure 2.22b compares the pressure response of the sensor measured on the flat glass and the finger, respectively. The ultrathin sensor showed the same pressure response as that of the sensor on a flat glass.

In summary, the CNN-based pressure sensors showed no performance change under various deformation conditions. All the CNN-based sensors with different total thicknesses (25 μm and 3 μm) endure the external deformation without significant degradation or delamination during the deformation tests. These experimental results support the mechanical robustness of the CNN-based pressure sensors arising from the structural properties explained in the previous subsection.

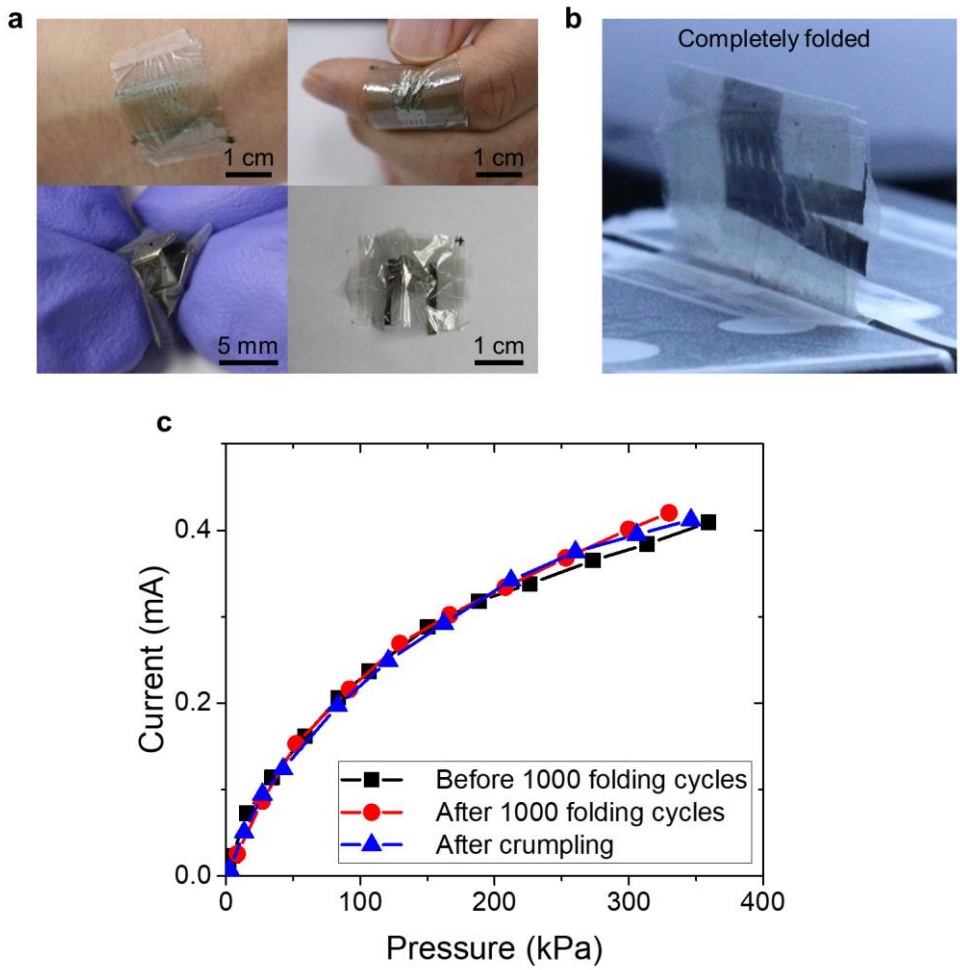

Figure 2.21 | Mechanical reliability of ultraflexible sensors [74]. a, Optical images of the ultrathin sensor under various deformation conditions. **b**, Photograph of the completely folded sensor. **c**, Pressure response of the 3-μm-thick sensor before deformation (black), after 1000 folding cycles (red), and after crumpling (blue).

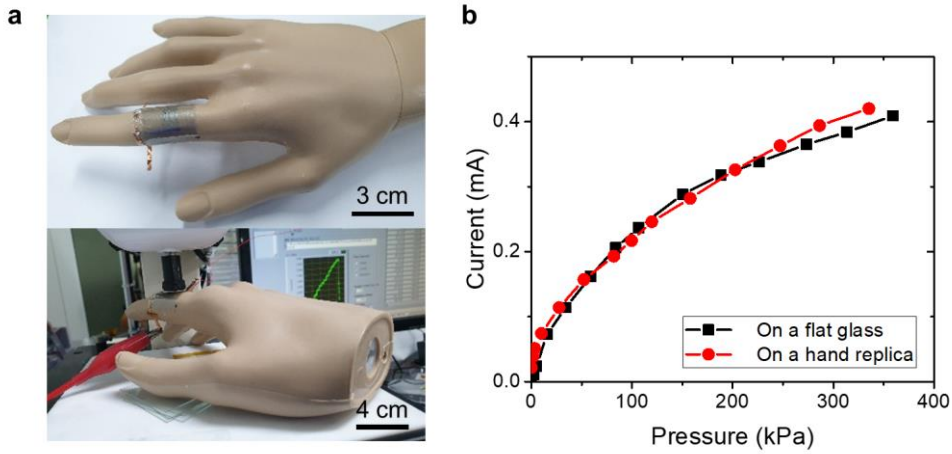

Figure 2.22 | Mechanical reliability of ultraflexible sensors on a curved surface [74]. a, Optical images of the 3-μm-thick sensor attached to a finger of a hand replica. **b**, Pressure response of the 3-μm-thick sensor attached to a finger of a hand replica.

2.3.7 Temperature and Humidity Tolerance

We measured the performance of the CNN-based pressure sensor under different temperature and humidity conditions. For temperature tolerance, the pressure response of the sensor was measured while maintaining a specific temperature using a programmable hotplate, as described in the experimental section and Figure 2.4a. Figure 2.23 shows the pressure response of the sensor under different temperature conditions. The current of the CNN-based pressure sensor increased as the temperature increased from room temperature (20 °C) to 80 °C. After cooling the pressure sensor, the pressure response was recovered to the initial state. This reversible temperature dependence of the pressure sensor can be attributed to the well-known

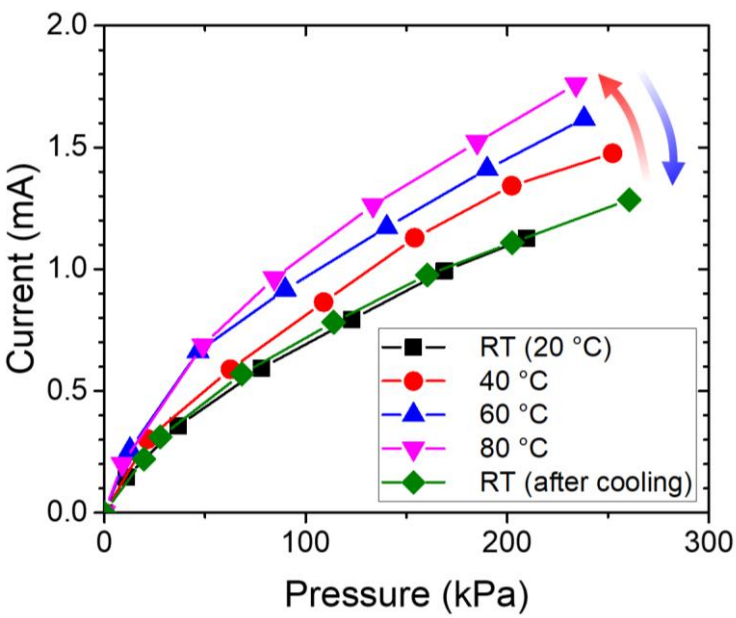

Figure 2.23 | Pressure response of the CNN-based pressure sensor under different temperature conditions [74].

temperature dependence of electrical conductivity of the PEDOT:PSS in various forms [79,80]. From the variable range hopping model, the electrical conductivity of the PEDOT:PSS can be expressed as $\sigma(T) = \sigma_0 exp[-\left(\frac{T_0}{T}\right)^{\alpha}]$, where σ_0, T_0, and α are varied by structures and obtained by best fit [79]. The equation well explains that the conductivity of the PEDOT:PSS nanowire network is positively correlated with temperature. Although the pressure response of the CNN-based sensor varies with temperature, it should be noted that the current change arising from temperature is totally reversible and predictable. Therefore, the change in pressure response can be calibrated by an electrical circuit with a temperature sensor in practical applications.

To investigate the humidity dependence of the sensor performance, we measured the pressure response of the CNN-based pressure sensor while maintaining a specific humidity using a humidifier and a hygrometer, as described in the experimental section and Figure 2.4b. Figure 2.24 shows the pressure response of the sensor under different humidity conditions. The CNN-based pressure sensor showed good humidity tolerance without significant change in the pressure response under different humidity conditions.

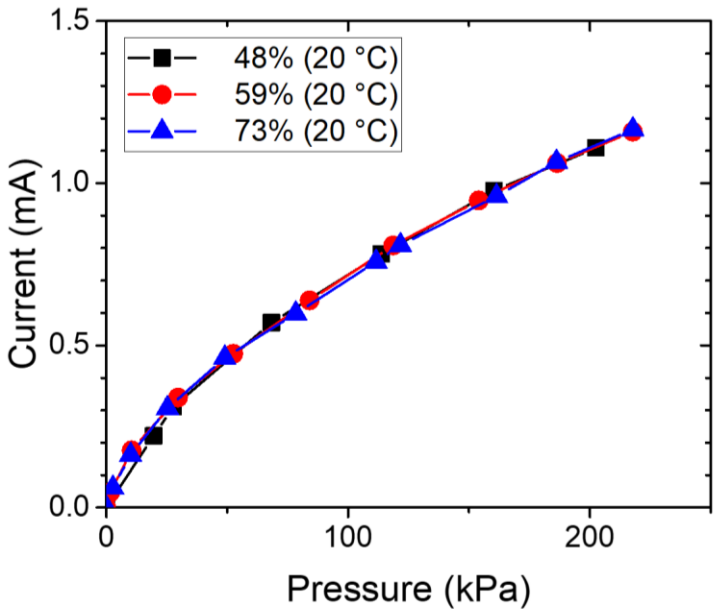

Figure 2.24 | Pressure response of the CNN-based pressure sensor under different humidity conditions [74].

2.4 Conclusion

In summary, this chapter introduced ultrathin pressure sensors employing a CNN. The CNN has three important features unprecedented in previously reported contact-resistance-based pressure sensors: (1) an ultrathin design (< 1 μm) with a dense nanohybrid structure, (2) controllable, low-density conductive nanowires exposed on the nanostructured surface, and (3) relatively low electrical conductivity of the Te-PEDOT:PSS nanowire. These three features play critical roles in the superior performance of the CNN-based pressure sensors. Feature (2) and (3) result in extremely low initial current and consequent ultrahigh sensitivity. Feature (1), (2), and (3) enable constant and small $\frac{\delta G_{contact}}{\delta P}$, enabling high linearity with a wide working range. Feature (1) allows small deformation in a CNN under pressure, contributing to an ultrafast response time and excellent cyclic reliability. In addition to the listed sensor performance, the CNN structure has many other advantages such as high transmittance and mechanical durability arising from the ultrathin design and the use of Te-PEDOT:PSS nanowires. In conclusion, novel structural and material properties of the CNN are key to achieving high-performance, ultraflexible, and transparent pressure-sensing devices with high compatibility with various wearable applications. In the next chapter, another important advantage of the ultrathin pressure-sensing layer, capturing of pressure distribution with significantly enhanced spatial fidelity, will be described.

Chapter 3

Ultraflexible Electroluminescent Skin for High-Resolution Imaging of Pressure Distribution

3.1 Introduction

Beyond detection at a specific point, spatial mapping of a mechanical stimulus, such as pressure, over complex three-dimensional (3D) surfaces would greatly augment the potential applications of e-skin such as skin prosthesis [23,24] and artificial sensory systems for soft robotics [2,25], and offer potential opportunities to verify numerical analysis for mathematical physics [81]. In this regard, many researchers have tried to map spatial pressure by employing a deformable sensor array with a matrix design [82-85]. However, they cannot fully comprehend this analog signal because of low pixel density or crosstalk among pixels. In particular, unlike other stimuli, spatial pressure could be severely distorted by the device structure itself, such as thick or uneven sensing layers and structural inhomogeneity between the pixel and non-pixel areas. Moreover, bulky electrical wires for data acquisition cause unstable operation of the devices on complex surfaces.

Recently, methods for the direct imaging of spatial pressure with "human-/machine-readable visual output" have been proposed to avoid this complicated data acquisition process [86-90]. When incorporated with pre-established digital imaging technology, such devices can wirelessly transmit the measured information to the machine. Enabling technologies include an integrated active matrix of pressure sensors and organic light-emitting devices [86], the mechanoluminescent effect of inorganic phosphors [90], and a piezoelectric nanowire light-emitting diode (LED) array [87-89]. Although they showed promising concepts and applications, these existing methods suffer from limited spatial resolution, respond to only dynamic pressure change, or show extremely low sensitivity. In particular, piezoelectric fluorescent materials have great potential for pressure sensing and imaging without an external power source [90]; however, they respond to only dynamic pressure change. Although pressure-imaging devices using piezoelectric nanowire LEDs have achieved high pixel resolution [87-89], their extremely low sensitivity and low fill factor degrade the image quality and hinder their practical applications. Furthermore, most of the previous works cannot offer pressure imaging over arbitrary surfaces due to their limited conformability. In other words, there have not yet been fully conformable electronics capable of imaging real-time pressure distribution in a practical range with high spatial and temporal fidelity at the same time. Realization of such devices demands comprehensive development of new materials and manufacturing methods for high-sensitivity pressure sensors and appropriate device design for capturing undistorted spatial pressure with high information density.

In this chapter, as a comprehensive solution for the aforementioned

issues, an ultraflexible, transparent, and pressure-sensitive electroluminescent skin (or photonic skin for short) employing the CNN in Chapter 2 is introduced [74]. Due to the enhanced transfer of spatial pressure *via* extremely high conformability of the photonic skin, unprecedentedly high-spatial-fidelity pressure imaging is enabled. The main concept, methodologies, and characteristics of the photonic skin are covered in detail. In particular, the effect of the high conformability of the device on the output pressure image is systematically investigated. At the end of this chapter, the proposed device is applied to novel smart touch interfaces that can identify the user as well as touch force and location to show the feasibility of the proposed concept and developed device.

3.2 Main Concept

Figure 3.1 illustrates the concept and structure of the pressure-sensitive photonic skin. The device has a notably straightforward and pixel-less structure where a top film coated with a cathode and CNN as a transparent piezoresistive layer is in contact with an electron transport layer (ETL) of a quantum-dot light-emitting diode (QLED) on a bottom film. Unique morphology and superior piezoresistive performance of the CNN play a critical role in the design and performance of the photonic skin. Especially, the ultrathin morphology (~1-μm-thick) of the CNN and other films allows pressure imaging with extremely high spatial fidelity by enhancing the transfer of spatial pressure. In other words, superfine and high-fidelity pressure imaging is enabled by incorporation of the high sensitivity of the CNN and the high conformability of the two ultrathin films. When two 3D objects make contact with both sides of the photonic skin, the top and bottom films conform to each contact object. The CNN on the top film then touches the top surface of the ETL, forming conductivity distribution between the cathode and the ETL linearly proportional to the pressure distribution with a high conversion factor of S (sensitivity of the CNN) in a continuous domain. Because the two films are sufficiently thin so they can perfectly conform to each surface of the contact objects, high-spatial-fidelity pressure distribution with minimal distortion is transferred to the contact surfaces between the CNN and ETL, forming well-defined conductivity distribution. This spatially patterned conductivity results in fast (< 1 ms) and high-resolution (> 1000 dpi) electroluminescent analog imaging under a bias voltage where the local light intensity quantifies the local pressure with high sensitivity and linearity.

Because all spatial signals from pressure to light intensity are transduced in an analog manner, the device visualizes pressure distribution without the need for pixel structures. Due to the high sensitivity and superior spatial resolution, the device even clearly visualizes pressure distribution arising from micro-textures of soft bodies such as a fingerprint, which are abundantly demonstrated in the result and discussion section.

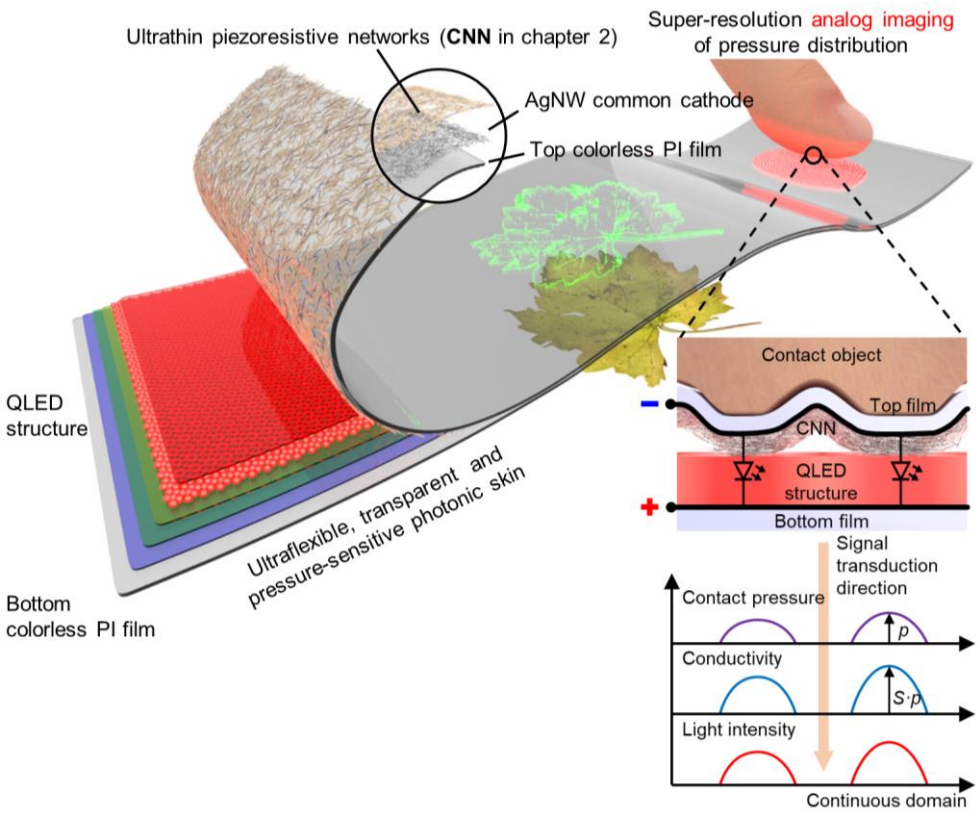

Figure 3.1 | Conceptual illustration of an ultraflexible, transparent and pressure-sensitive photonic skin [74].

3.3 Experimental Section

3.3.1 Fabrication of Pressure-Sensitive Photonic Skin

Figure 3.2 illustrates the fabrication process of the pressure-sensitive photonic skin. A colorless PI varnish was gently provided by KOLON Corporation, Korea. A 1-μm-thick colorless PI film (bottom PI) was coated on a glass substrate at 5000 r.p.m. and then cured at 150 °C for 10 min and 200 °C for 2 h on a hotplate. Then, an ITO electrode (150 nm) was deposited by sputtering onto the colorless PI film. The ITO-coated colorless PI film on carrier glass was treated with O_2-plasma for 30 s. PEDOT:PSS (Batron P VP AI 4083, filtered through a 0.45 μm PES filter) as a hole injection layer (HIL) was spin-coated on the ITO anode at 2000 r.p.m. for 30 s, followed by annealing at 150 °C for 10 min. Poly(9-vinylcarbazole) (PVK, in chlorobenzene, 10 mg mL^{-1}) as a hole transport layer (HTL) was spin-coated on the HIL at 4000 r.p.m. for 30 s, followed by annealing at 120 °C for 10 min. An emissive layer of colloidal CdSe/ZnS quantum dots (QDs, in toluene, 10 mg mL^{-1}, Mesolight) was spin-coated on the HTL at 4000 r.p.m. for 30 s and annealed at 60 °C for 20 min. A ZnO nanoparticle dispersion (diluted in 1-butanol, 5 wt%, Avantama AG) was spin-coated on the QD layer at 4000 r.p.m. for 30 s and annealed at 60 °C for 20 min. The top colorless PI film (1-μm-thick) was coated on the other glass substrate at 5000 r.p.m. and then cured at 150 °C for 10 min and 200 °C for 2 h on a hotplate, and AgNWs (0.5 wt%, NANOPYXIS) were spin-coated as a common cathode and annealed at 120 °C for 10 min. The CNN (50% v/v) was spray-coated onto the AgNW cathode, followed by baking at 100 °C for 30 min. The top PI film on the supporting glass was

scribed on all four edges before lamination and then laminated on the bottom PI film on the bottom glass using 20-μm-thick double-sided adhesive tape. The top glass was detached from the top PI film, leaving the top PI film attached onto the bottom film. Subsequently, the whole device was cut on all four edges and was mechanically detached from the bottom supporting glass.

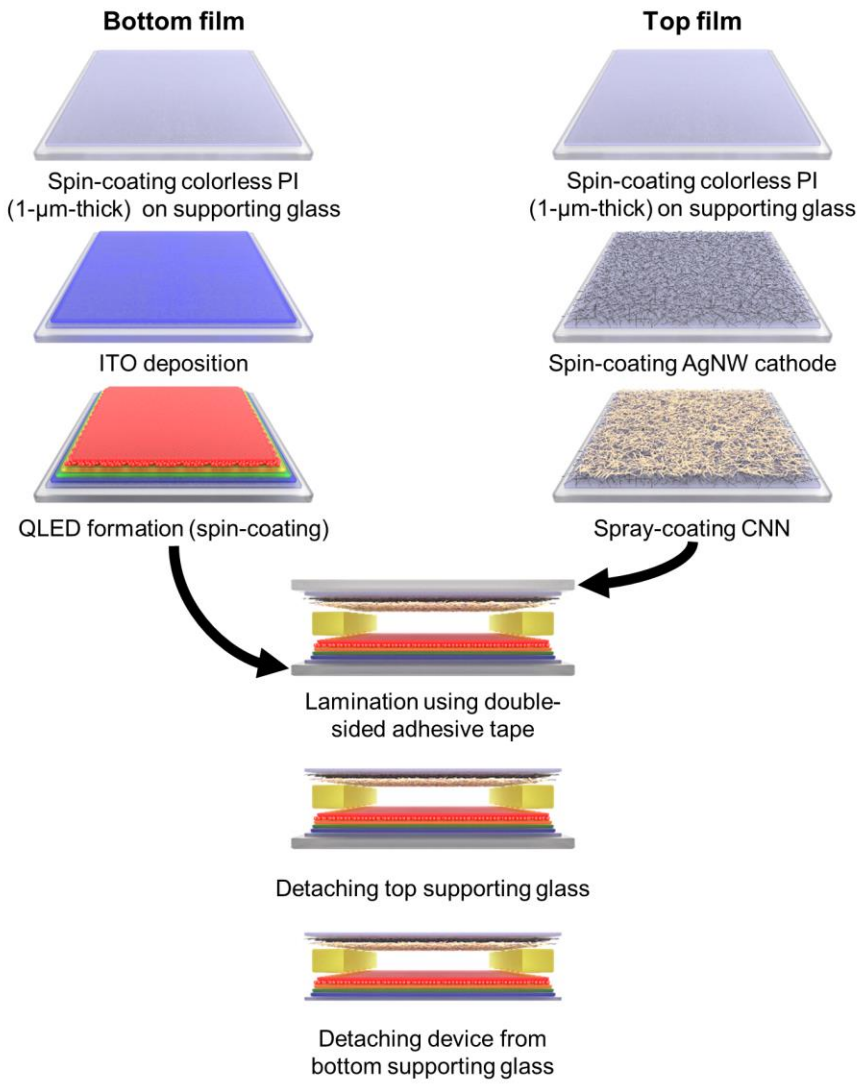

Figure 3.2 | fabrication process of the pressure-sensitive photonic skin [74].

3.3.2 Characterization of Photonic Skin

The pressure responses of the photonic skin were basically studied using devices on supporting glass substrates. The luminance of the photonic skin was measured using a color and luminance meter (CS-200, Konica Minolta) while applying loads with a 6 × 6 mm^2 square PDMS slab attached to a portable digital force gauge (FGN-50B, SHIMPO).

PDMS stamps with various shapes were fabricated by replica moulding processes using 3D-printed prototype models. A PDMS precursor (Sylgard 184, Dow Corning) was poured on the 3D-printed models and cured at 100 °C for 2 h. The PDMS master moulds were detached from the prototypes. Monolayers of 1H,1H,2H,2H-perfluorooctyltrichlorosilane (FOTS) were vapour-deposited on the O_2-plasma-treated surfaces of the PDMS master moulds for anti-stiction. A PDMS precursor was then poured on the master moulds and cured at 100 °C for 2 h. After being detached from the mater moulds, PDMS stamps with various shapes were obtained. A PDMS replica of a mint leaf was fabricated using the same process except that the leaf replaced the 3D-printed prototypes.

PU micropillar arrays for a spatial resolution study were fabricated by similar replica moulding processes using micro-patterned silicon substrates as master moulds. In this study, 20-μm-deep square holes with various sizes were patterned on the silicon substrates by photolithography. Next, a 300-nm-thick aluminium film was sputtered on the silicon substrate. The aluminium film was patterned by inductively coupled plasma (ICP) etching through a patterned photoresist. After removal of the remaining photoresist, the silicon substrate was etched using deep reactive ion etching

(DRIE) through the aluminium mask to obtain 20-μm-deep square holes. Finally, the remaining aluminium mask was removed using ICP etching to obtain micro-patterned silicon master moulds.

A PDMS micro-bump array was fabricated by microsphere lithography. A closely packed, hexagonal monolayer of polystyrene (PS) microspheres with a diameter of 25 μm (Aldrich) was first formed on a PDMS substrate by a previously reported rubbing method [91]. Another flat PDMS substrate was used for rubbing the microspheres. After the rubbing process, the PDMS substrate was etched by reactive-ion etching (RIE) process for 80 min using the PS microsphere monolayer as an etching mask. Oxygen (O_2) and tetrafluoromethane (CF_4) with a ratio of 1:5 were used for process gases. After removing the remaining PS microspheres from the PDMS substrate using adhesive tape, a hexagonally aligned PDMS micro-bump array was obtained.

3.4 Results and Discussion

3.4.1 Structure and Morphology of Photonic Skin

Figure 3.3 illustrates the structure of the photonic skin. The photonic skin has a notably straightforward and pixel-less structure where a top film coated with a cathode and CNN as a transparent piezoresistive layer is in contact with an ETL of a QLED on a bottom film. The fabrication process of the pressure-sensitive photonic skin is facile and low-cost, showing high potential for practical applications. A QLED structure excluding a top cathode was formed on a bottom colorless PI film (~1-μm-thick) by a well-controlled solution process. The TEM image in Figure 3.3 shows the cross-sectional view of the deposited QLED structure on the bottom PI film. The thickness of the QLED structure was < 300 nm. A AgNW transparent electrode as a common cathode and a CNN were sequentially deposited on a top colorless PI film (~1-μm-thick) by spin-coating and spray-coating, respectively. The top film was, in

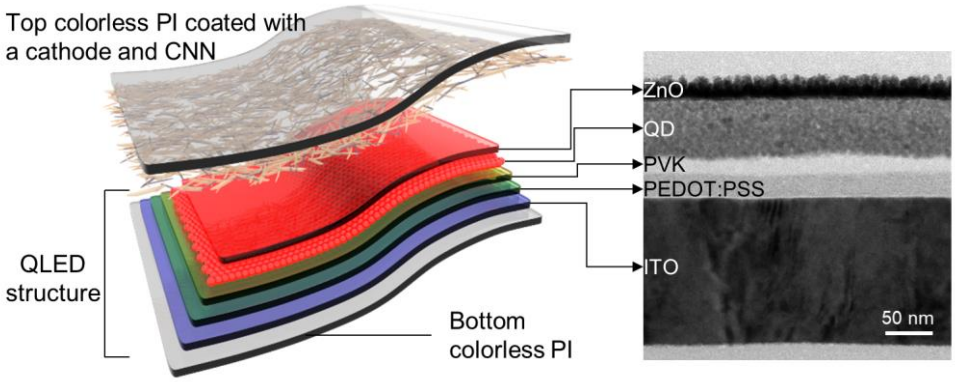

Figure 3.3 | Structure of the photonic skin [74]. The right inset is a TEM image showing the cross-sectional view of the QLED structure.

turn, laminated on the bottom film. The detailed fabrication process and the device structure are depicted in the experimental section and Figure 3.2. After delamination from the supporting glass substrate, an ultraflexible and transparent two-terminal device was obtained. The total thickness of the device was ~3 μm, including a CNN layer. These ultrathin morphologies of each film and device play a critical role in the imperceptible and conformable mechanical properties of the photonic skin. Furthermore, the ultraflexibility enables high-spatial-fidelity imaging of pressure distribution, which will be further discussed in Subsection 3.4.3. Figure 3.4 presents the optical images

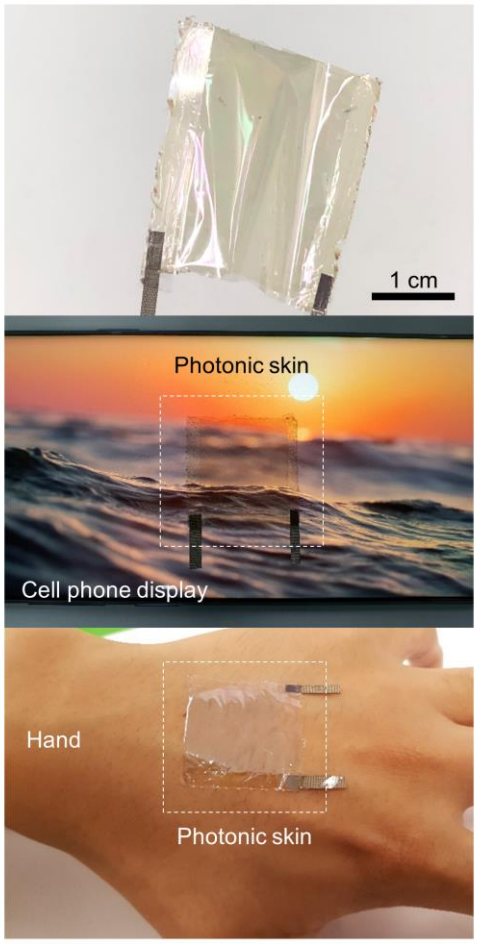

Figure 3.4 | Optical images of the photonic skin [74].

of the fabricated photonic skin. The device can be laminated on any type of surface, such as a curved display and human skin, conformably and imperceptibly in terms of the senses of both touch and vision. Figure 3.5 shows the transmittances of the colorless PI film, top pressure-sensing film, and bottom electroluminescent film. The bare colorless PI film showed high transmittance > 95% in the visible spectral region (Figure 3.5a). After deposition, the transmittances of the top and bottom films were ~75% (Figure 3.5b and c). The transmittance of the photonic skin was ~60% (Figure 3.5d).

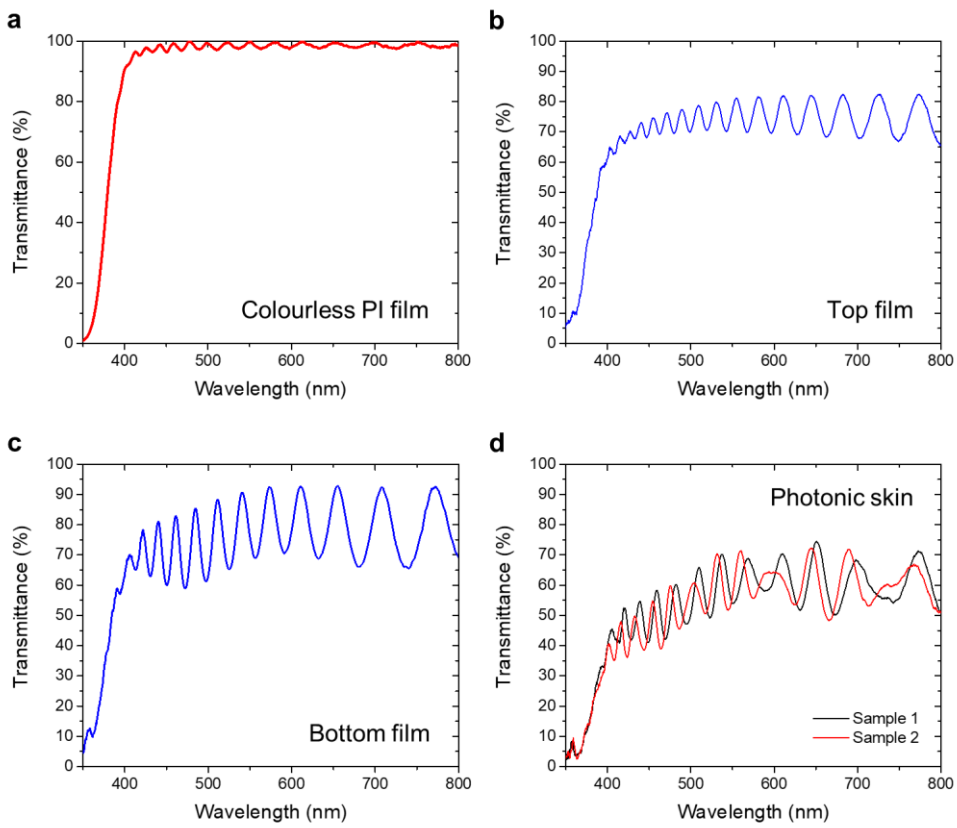

Figure 3.5 | Transmittances of the photonic skin [74]. **a**, **b**, **c**, and **d**, Transmittances of the colorless PI film (**a**), top film (**b**), bottom film (**c**), and photonic skin (**d**).

3.4.2 Pressure Response of Photonic Skin

When pressure is locally applied to the photonic skin under a bias voltage, the CNN on the top film touches the surface of the ETL, forming local conductivity as a function of the applied pressure. Because the engineered CNN passively controls the local current density flowing into the QLED when pressure is applied, the photonic skin understandably inherits its high sensitivity, high linearity, fast response time, and great stability. Furthermore, due to the pixel-less and ultrathin design, the photonic skin displays a seamless and continuous image of the pressure distribution. To investigate the pressure response of the photonic skin, we first applied spatially patterned pressure to the photonic skin laminated on a glass substrate with PDMS stamps (Figure 3.6a). Uniform light was emitted from the continuous area where the stamp was in contact with the device, visualizing the precise shape of the stamp, such as triangle, square, and rectangle (Figure 3.6b). The photonic skin also clearly showed the patterned pressure applied with more complicated stamps, such as a character shape.

The pressure response of the device was investigated by measuring the current density and the luminance when a specific local pressure was applied using a 6 × 6 mm^2 square PDMS slab. Figure 3.7 shows representative pressure response of the photonic sensor under a bias voltage of 15 V. The current density and the luminance increased with high linearity up to 400 kPa. Specifically, the luminance was ~125 Cd m^{-2} as the pressure reached 400 KPa. The sensitivity of the electroluminescence can be defined as $\delta(\Delta L/L_0)/\delta p$, where ΔL denotes the luminance change under the applied pressure and L_0 denotes the initial luminance without pressure. Figure 3.8 plots the calculated

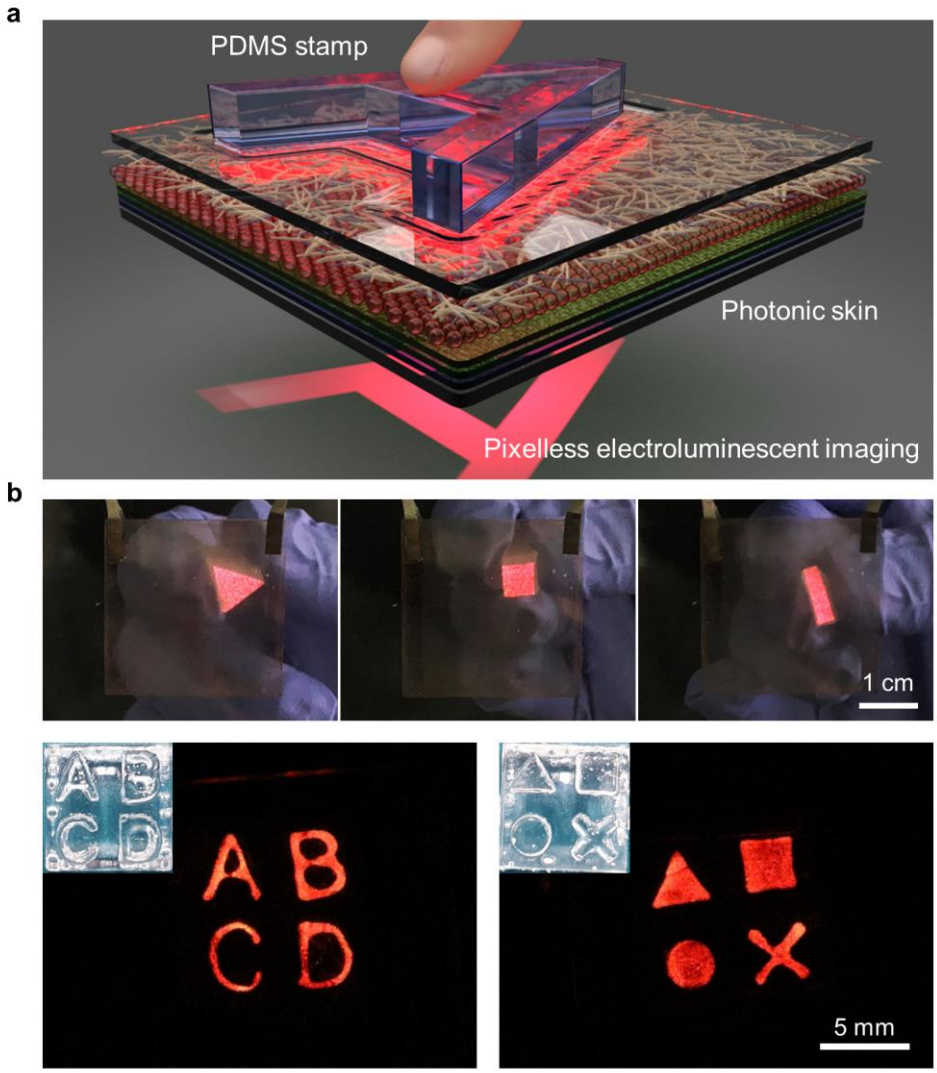

Figure 3.6 | Visualization of the pressure applied by PDMS stamps [74]. **a**, Schematic illustration of pixel-les imaging of spatially patterned constant pressure using PDMS stamps. **b**, Photographs of the photonic skin visualizing the pressure applied by PDMS stamps with various shape. The insets show the PDMS stamps.

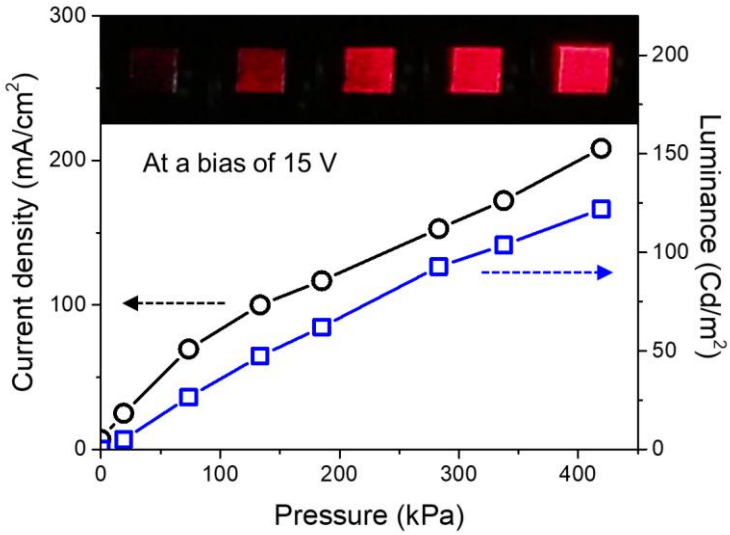

Figure 3.7 | Current density and luminance as a function of the pressure applied with a 6 × 6 mm^2 PDMS slab under a bias of 15 V [74].

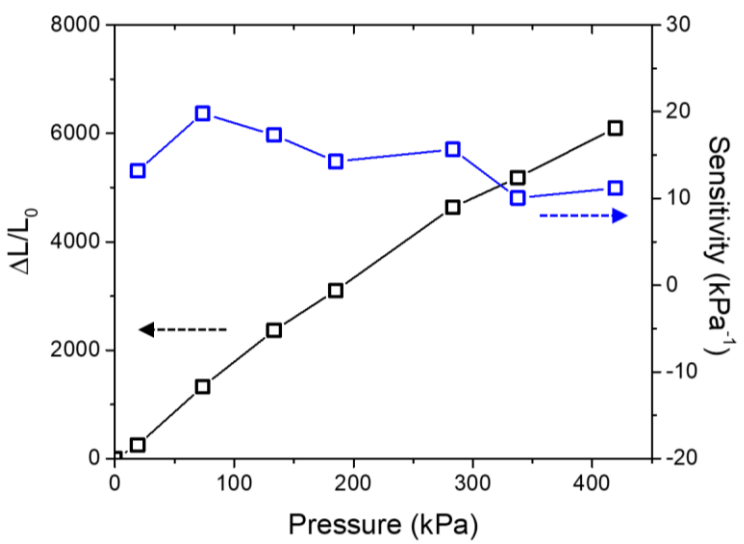

Figure 3.8 | Ratio of luminance change (ΔL) to initial luminance (L_0) and sensitivity as a function of the applied pressure [74].

sensitivity for every measured point in the linear region. The sensitivity remained > 10 kPa^{-1} throughout the linear region. Because the electroluminescence is based on the QLED structure, the pressure response is sensitive to the bias voltage. Figure 3.9 compares the pressure response of the photonic skin under different bias voltages. Higher luminance at a specific pressure can be achieved by increasing the voltage between the cathode and anode.

The response time of the photonic skin was investigated by an abrupt unloading process, as illustrated in Figure 3.10a. Figure 3. 10b shows the current measured when the pressure was suddenly decreased from 4.5 kPa to 2.7 kPa. The current was decreased from 0.115 mA to 0.076 mA in 1 ms, suggesting that the response time of the photonic skin is < 1 ms. The fast response time of the photonic skin was also demonstrated by capturing the

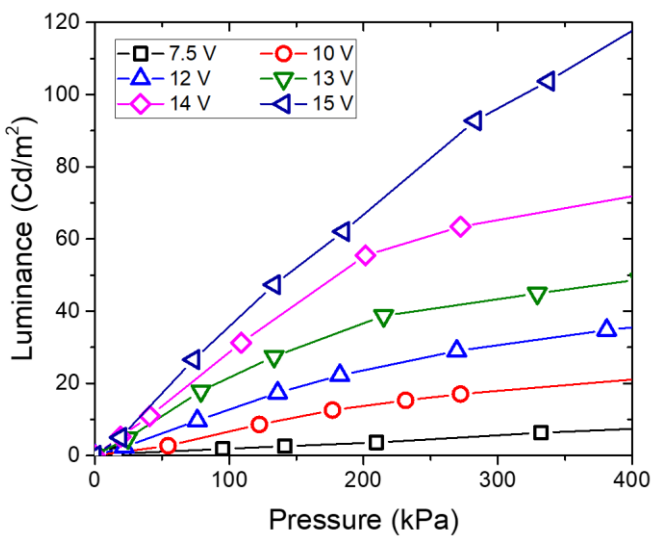

Figure 3.9 | Ratio of luminance change (ΔL) to initial luminance (L_0) and sensitivity as a function of the applied pressure [74].

pressure image using a high-speed camera (1000 fps) while the tip of a polyurethane (PU) fragment was rapidly sliding on the photonic skin (Figure 3.11a). As shown in Figure 3.11b, each frame captured at 1 ms intervals showed the exact touch position of the PU tip without any trace or delay, revealing that the photonic skin has an ultrafast response time of < 1 ms.

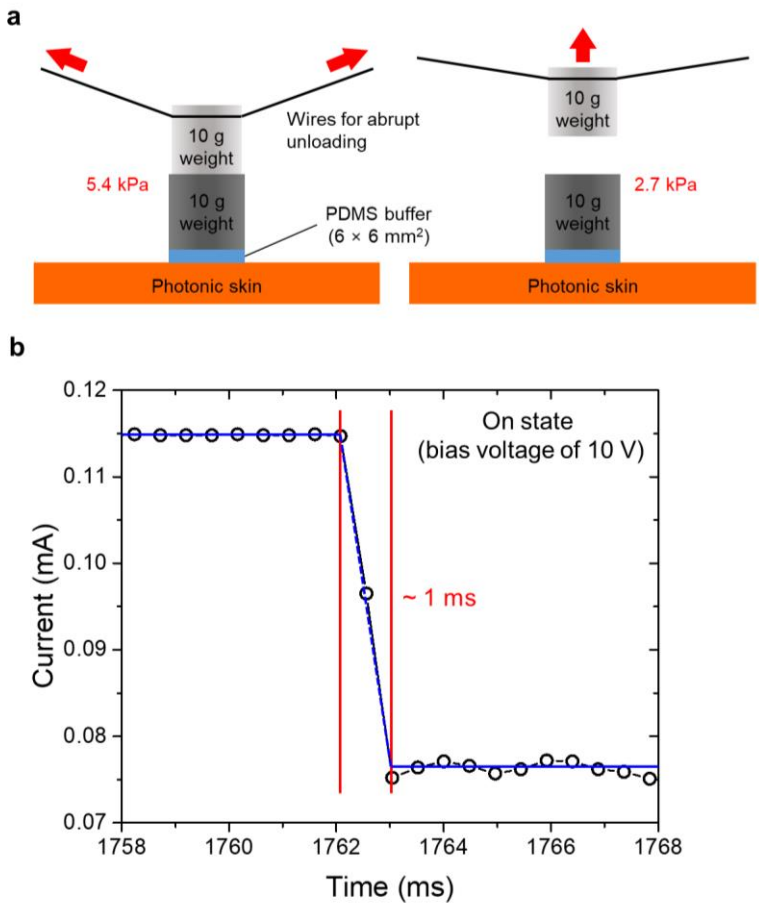

Figure 3.10 | Response time of the photonic skin [74]. a, Schematic illustration of an abrupt unloading process for response time measurement of the photonic skin. **b**, Current response of the photonic skin to the sudden pressure change.

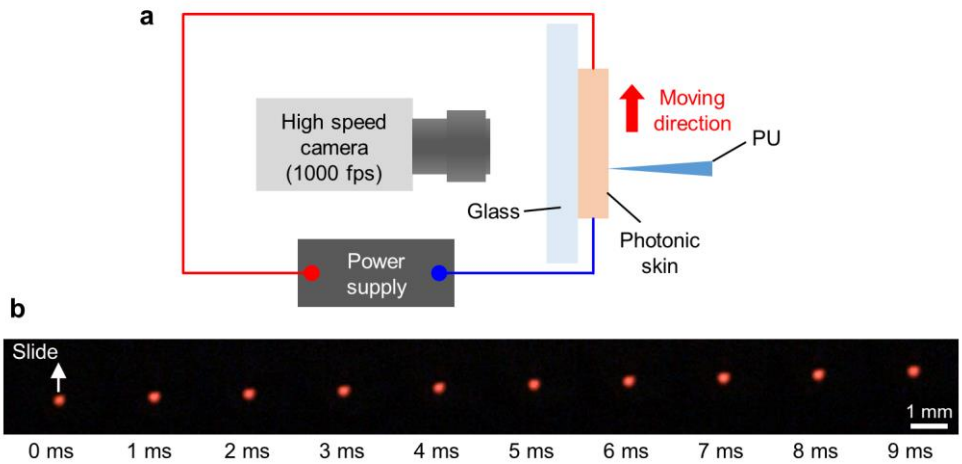

Figure 3.11 | Response time of the photonic skin [74]. a, Schematic illustration of the response time measurement using a high speed camera. **b**, Photographs of the pressure image captured by a high-speed camera at 1 ms intervals while a tip of a PU fragment was rapidly sliding on the photonic skin, showing a fast response time of the photonic skin.

3.4.3 Effect of Conformability on Spatial Resolution

When the spatial pressure is applied to the photonic skin, the spatial signal undergoes the following transmission process in a continuous domain: the pressure distribution applied to the top film (P_{input}), transferred contact pressure distribution between the CNN and the ETL (P_{contact}), electrical conductance distribution between the CNN and the ETL (G_{contact}), and light intensity distribution of the QLED (L_{QLED}). The flow of the spatial signal is illustrated in Figure 3.12. Because the L_{QLED} is proportional to the G_{contact} in the pixel-less QLED and the CNN linearly convert the P_{contact} into the G_{contact}, if the P_{input} is transduced into the P_{contact} without distortion, the L_{QLED} perfectly represents the P_{input}. Therefore, the distortion in the P_{contact} determines the quality of the output image and the spatial resolution of this analog imaging. To investigate the $P_{\mathrm{input}}/P_{\mathrm{contact}}$ function and the

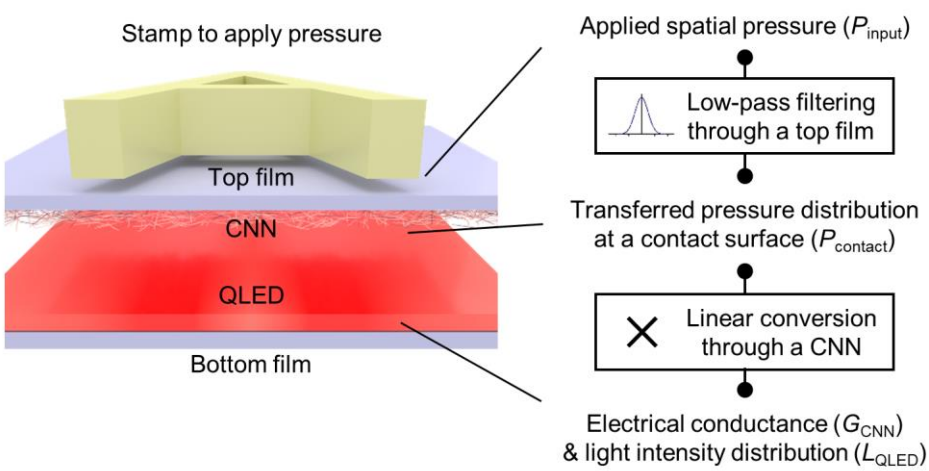

Figure 3.12 | Schematic illustration of the signal transfer flow when the P_{input} is applied to the top film of the photonic skin [74].

spatial resolution of the photonic skin, we carried out a systematic finite element analysis (FEA) calculating the P_{contact} between the top and bottom films when spatially patterned P_{input} was applied to the top film.

Theoretical postulation. Assume that a rectangular pulse (width of W_0 and amplitude of P_0) of spatial pressure was applied to the top surface of the top film with a thickness of t_{top} as P_{input}.

$$P_{\text{input}} = \begin{cases} P_0, & -\frac{1}{2}W_0 < x < \frac{1}{2}W_0 \\ 0, & \text{otherwise} \end{cases} \tag{3.1}$$

The situation is analogous to that a rigid stripe vertically presses the top film, as shown in Figure 3.13. If the top film is thin compared to W_0, it will conform to the rigid stripe. The bottom film feels as if a stripe with a larger width and rounded edges touches it, which can be seen as spatial low-pass filtering of a larger pulse P'_{input}.

$$P'_{\text{input}} = \begin{cases} P'_0 = P_0 \cdot \frac{W_0}{W'_0}, & -\frac{1}{2}W'_0 < x < \frac{1}{2}W'_0 \\ 0, & \text{otherwise} \end{cases} \tag{3.2}$$

where W'_0 is the increased width of the larger pulse (effective width), and P'_0 is the reduced amplitude of the pulse due to the increased width. If the low-pass filter is assumed to be a Gaussian filter, the spatial Fourier transform of P_{contact} can be expressed as

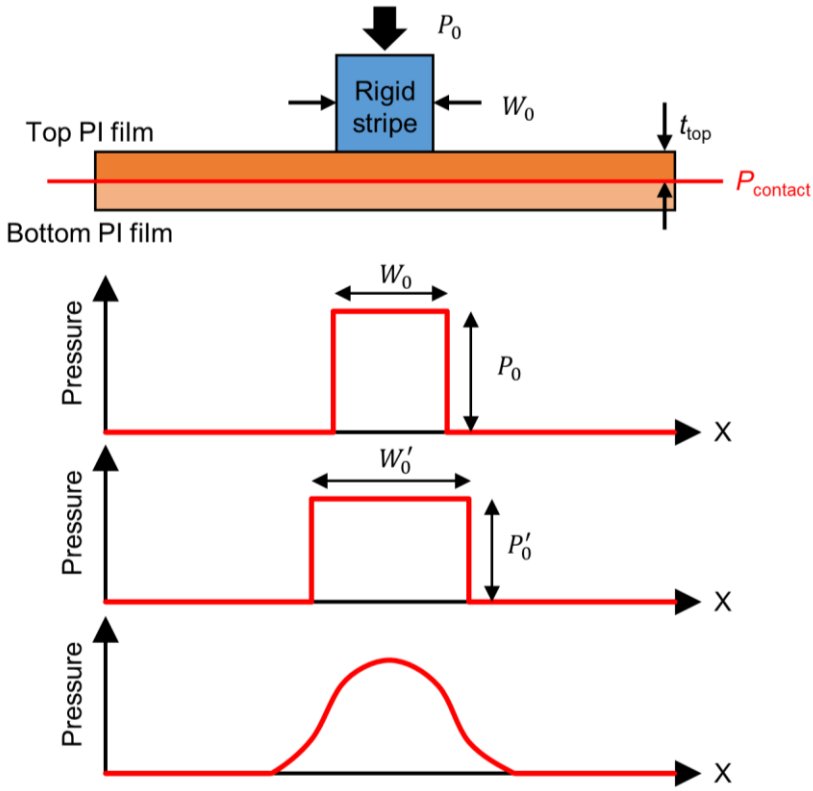

Figure 3.13 | Schematic illustration of the signal transfer through the top film when a rectangular pulse is applied to the top film [74].

$$P_{W_0',\sigma_f}(f) = P_0' \cdot W_0' \cdot \mathrm{sinc}(W_0' f) \cdot g_{\sigma_f}(f) \tag{3.3}$$

where $g_{\sigma_f}(f)$ is a normal probability density function with a mean of 0 and a standard deviation of σ_f. If we compare the estimated values calculated using Equation 3.3 with the FEA results for a specific t_{top}, and determine σ_f and W_0' for a best fit between them, we can quantitatively explain the effect of t_{top} on the output images, especially a passband of the low-pass filtering.

2D FEA. First, a 2D FEA was carried out, where one 10-μm-wide PU stripe pressed the top film, as depicted in Figure 3.14a. As expected, the P_{contact} becomes a blurred form of P_{input} as t_{top} increases (Figure 3.14b). For each t_{top}, we found the specific W_0' and σ_{f} that made the residual sum of square (RSS) between the FEA results and Equation 3.3 the smallest, *i.e.*, the W_0' and σ_{f} with which Equation 3.3 mostly fits the simulation results. For

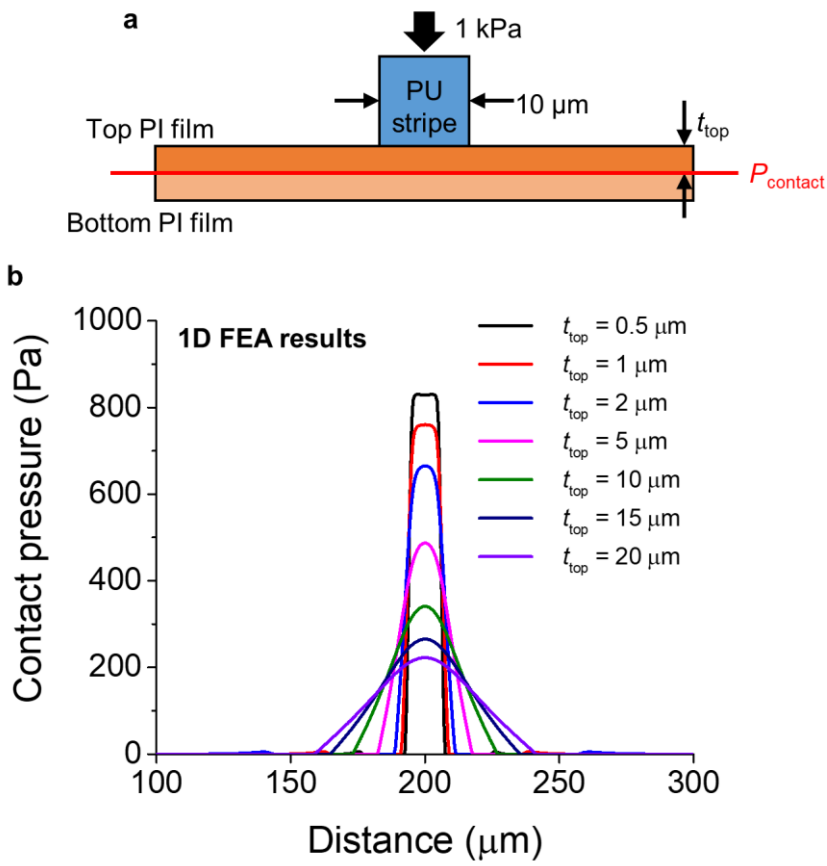

Figure 3.14 | 2D FEA results [74]. a, Modelling details for the 2D FEA simulation. **b**, FEA results showing P_{contact} for various t_{top} values.

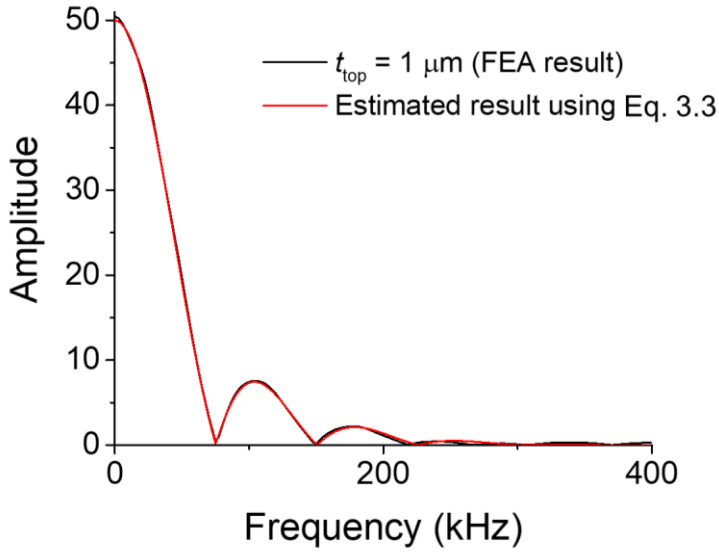

Figure 3.15 | Comparison between the Fourier transform of the FEA result for $t_{\mathrm{top}} = 1\ \mu\mathrm{m}$ and Equation 3.3 with $W_0' = 13.28\ \mu\mathrm{m}$ and $\sigma_{\mathrm{f}} = 1.22e5$ [74].

example, in the case of $W_0 = 10\ \mu\mathrm{m}$ and $t_{\mathrm{top}} = 1\ \mu\mathrm{m}$, the values calculated using Equation 3.3 with $W_0' = 13.28\ \mu\mathrm{m}$ and $\sigma_{\mathrm{f}} = 1.22e5$ well fit the simulation result with the minimum $R^2 = 0.9998$ (Figure 3.15). Figure 3.16a and b plot the found solution (W_0' and σ_{f}) as a function of t_{top}. The graphs reveal that a thicker top film results in a larger W_0' (thus smaller P_0') and a smaller σ_{f} that is corresponding to a narrower passband of the low-pass filtering. These results quantitatively explain that the masking of the top film acts as a spatial low-pass filter, where the passband is inversely proportional to the thickness of the masking film. This effect suggests an essential design rule to improve spatial resolution of pressure mapping. For instance, if the top film including a sensing layer is thick as compared to the width of the applied pressure pulse, *i.e.*, stripe width in this case, the pressure

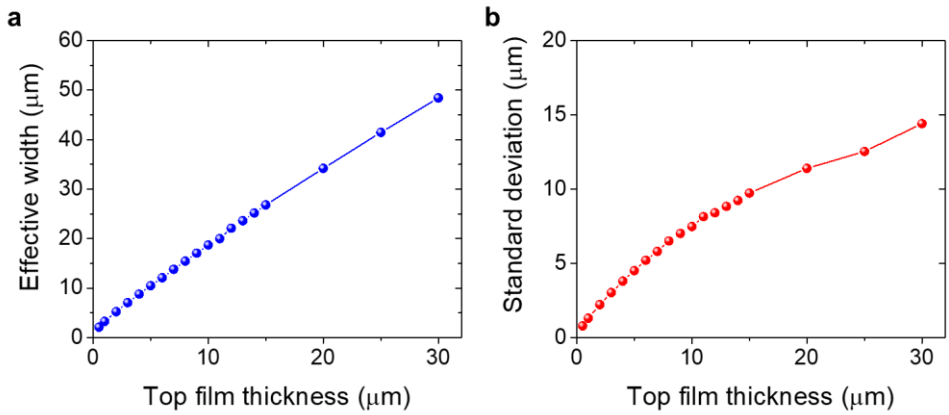

Figure 3.16 | Solutions for W_0' and σ_f as a function of t_{top} [74]. a and **b**, W_0' (**a**) and σ_f (**b**) as a function of t_{top} with which Equation 3.3 mostly fits the simulation results.

transferred through the thick film was widened and smoothed, making it difficult to distinguish two adjacent pulses. Therefore, reducing the thicknesses of the top film and sensing layer is truly important for contact-resistance-based pressure sensors to map high-resolution pressure distribution.

3D FEA and experimental results. 3D FEA was carried out using modelling details illustrated in Figure 3.17 where a pillar array with a 50 μm width and a 50 μm gap (254 dpi) pressed the top films with different t_{top} values, to further study this "masking effect" of the top film. Figure 3.18a visualizes the top view of the $P_{contact}$ on the contact surface for each t_{top} value and Figure 3.18b shows the line profiles of the $P_{contact}$ along the middle of the contact plane. As the t_{top} increased from 1 μm to 20 μm in the FEA, the $P_{contact}$ at the contact plane became a blurred form of the P_{input}, showing

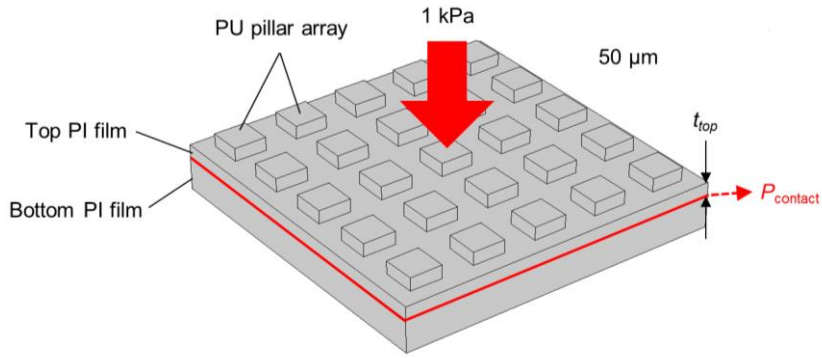

Figure 3.17 | Modelling details for the 3D FEA [74].

good agreement with 2D FEA results. Especially, the increase in both W_0' and σ_f were observed in the line profile of the 3D FEA results.

A series of experiments were conducted to verify the FEA results using 254 dpi PU micropillar array and photonic skins with t_{top} ~1 μm and t_{top} ~10 μm. Figure 3.19a presents the experimental details and optical image of the 254 dpi PU micropillar array. The detailed fabrication process for the pillar array is explained in the experimental section. Figure 3.19b shows the experimental results obtained when the photonic skin with t_{top} ~10 μm was pressed by the 254 dpi pillar array. The optical images in Figure 3.19b shows that the photonic skin with t_{top} ~10 μm generated a distorted and collapsed pressure image rather containing the large-area topography of the pillar array due to the uneven pillar height and noise due to the top film roughness. On the other hand, the optical images in Figure 3.19c shows that the device with t_{top} ~1 μm displayed a high-quality and distinct image of the spatial pressure patterned with the 254 dpi pillar array. The experimental results show good agreement with the FEA results in the

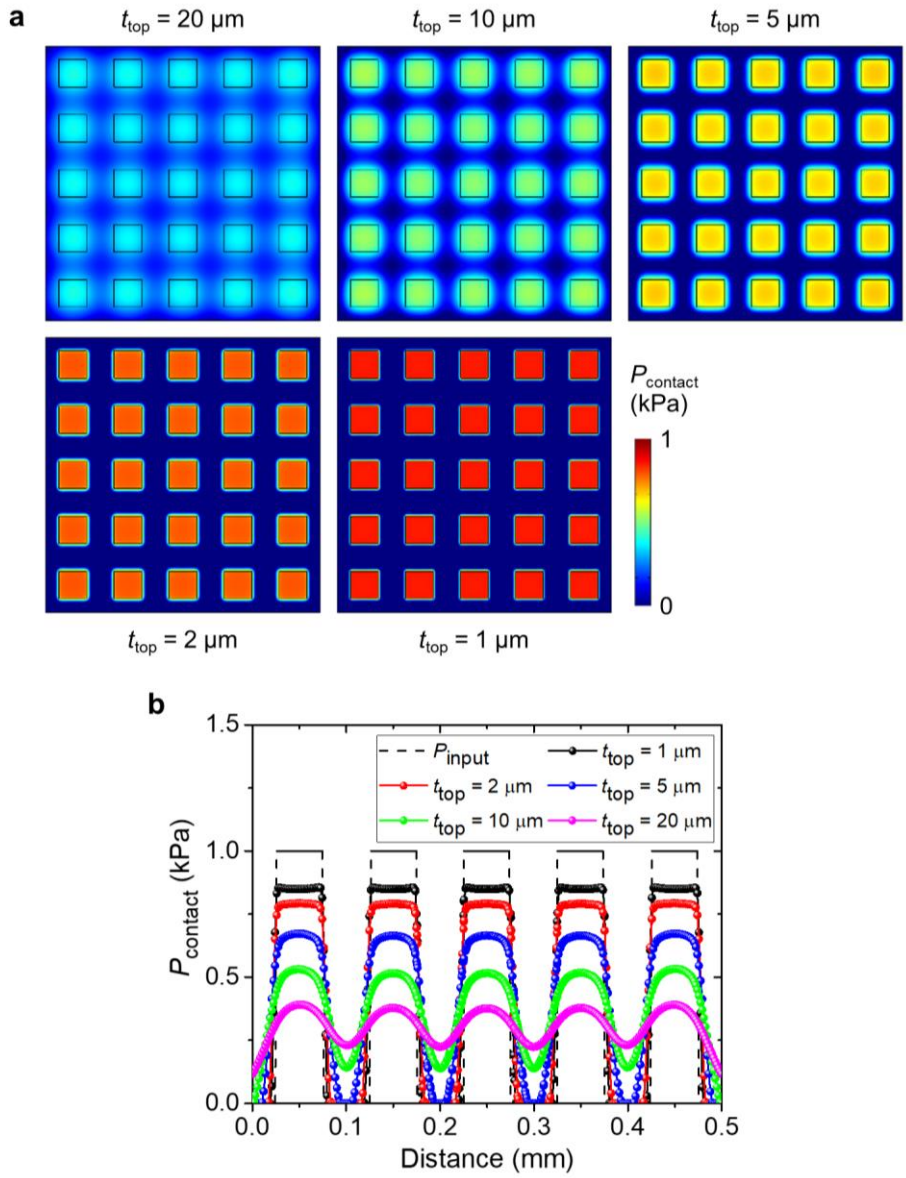

Figure 3.18 | 3D FEA results [74]. a, Top views of the P_{contact} on the contact surface for different t_{top} values. **b**, Line profiles of the P_{contact} along the middle of the contact plane for different t_{top} values.

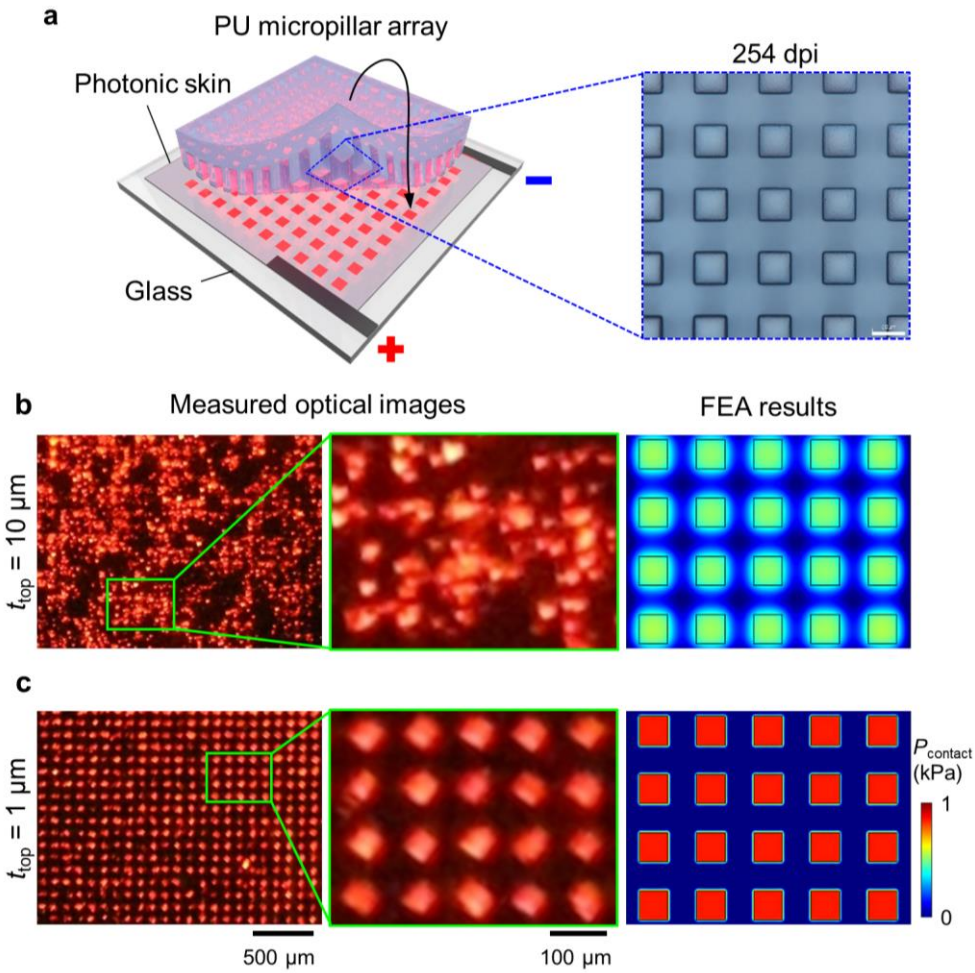

Figure 3.19 | Effect of the t_{top} on the output image of the photonic skin [74]. **a**, Schematic illustration of the experimental setup. The right inset is an optical image of the fabricated 254 dpi PU micropillar array. **b** and **c**, photographs where the 254 dpi PU pillar array pressed photonic skins with t_{top} ~ 10 μm (**b**) and t_{top} ~ 1 μm (**c**). The rightmost images present FEA results showing $P_{contact}$ for the corresponding t_{top} values.

rightmost column of Figure 3.19b and c. This filtering effect of the thick film was also observed using higher-density micropillars. The optical images in Figure 3.20 were obtained when the 635 dpi PU micropillar array pressed the photonic skins with t_{top} ~1 μm and t_{top} ~10 μm, respectively. The photographs in the left column show that the pressure image generated by the device with t_{top} ~10 μm was a distorted, collapsed, and low-pass filtered form of the original pattern, whereas the photographs in the right column show that the device with t_{top} ~1 μm clearly visualized the patterned pressure applied with 635 dpi micropillars. To test the resolution limit of the ultrathin photonic skin, we fabricated 1016 dpi hexagonal micro-bumps and applied pressure with them. Figure 3.21a shows the fabricated 1016 dpi

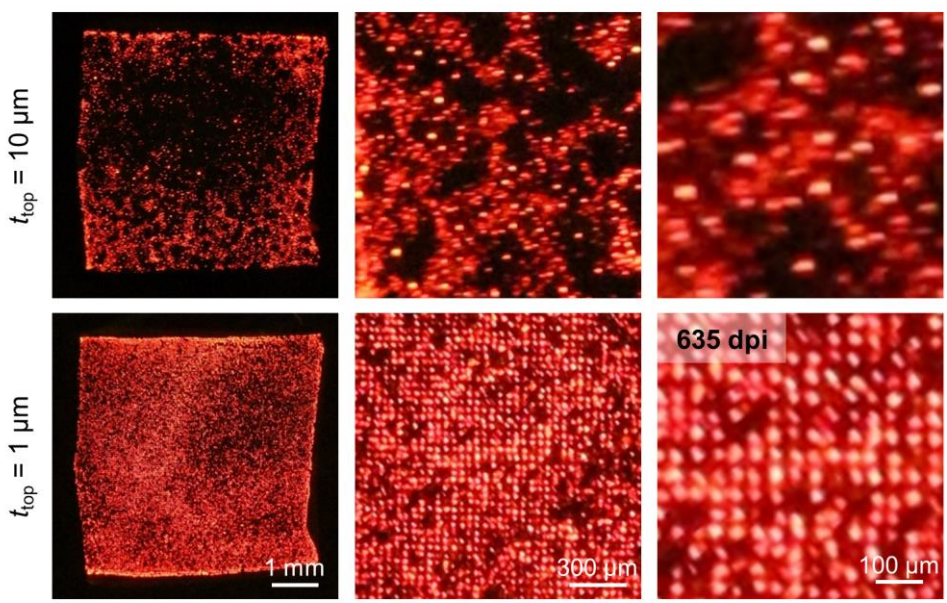

Figure 3.20 | Optical images where the 635 dpi PU pillar array pressed the photonic skins with t_{top} ~ 10 μm (left column) and t_{top} ~ 1 μm (right column) [74].

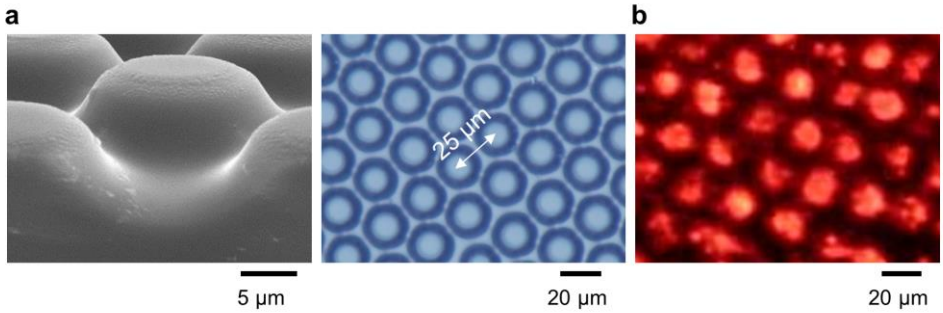

Figure 3.21 | Photonic skin visualizing the pressure applied with 1016 dpi micro bumps [74]. a, SEM and optical images of 1016 dpi PDMS hexagonal micro-bumps. **b**, Optical image of the device with t_{top} ~ 1 μm visualizing the pressure applied with the 1016 dpi hexagonal micro-bumps.

micro-bump array. When the photonic skin was pressed with the micro-bumps, it clearly visualized the hexagonal pressure patterns as shown in Figure 3.21b, which suggests the photonic skin with t_{top} ~1 μm has a much higher resolution than 1016 dpi.

Spatial resolution calculation. The spatial resolution in analog imaging that does not have pixels, such as the case of the photonic skin, can be defined as the minimum distance between two impulses that are resolvable. The impulse function in the spatial pressure is difficult to realize both in the FEA and experimentally. Instead, the spatial resolution was calculated using 1-μm-wide pillars. Figure 3.22a shows the top views of P_{contact} when 1-μm-wide pillars with different distances pressed the top film with t_{top} = 1 μm. A minimum distance of 4 μm (6350 dpi) was concluded by the FEA, where the half maximum is located in the middle of the two pillars, as shown by the line

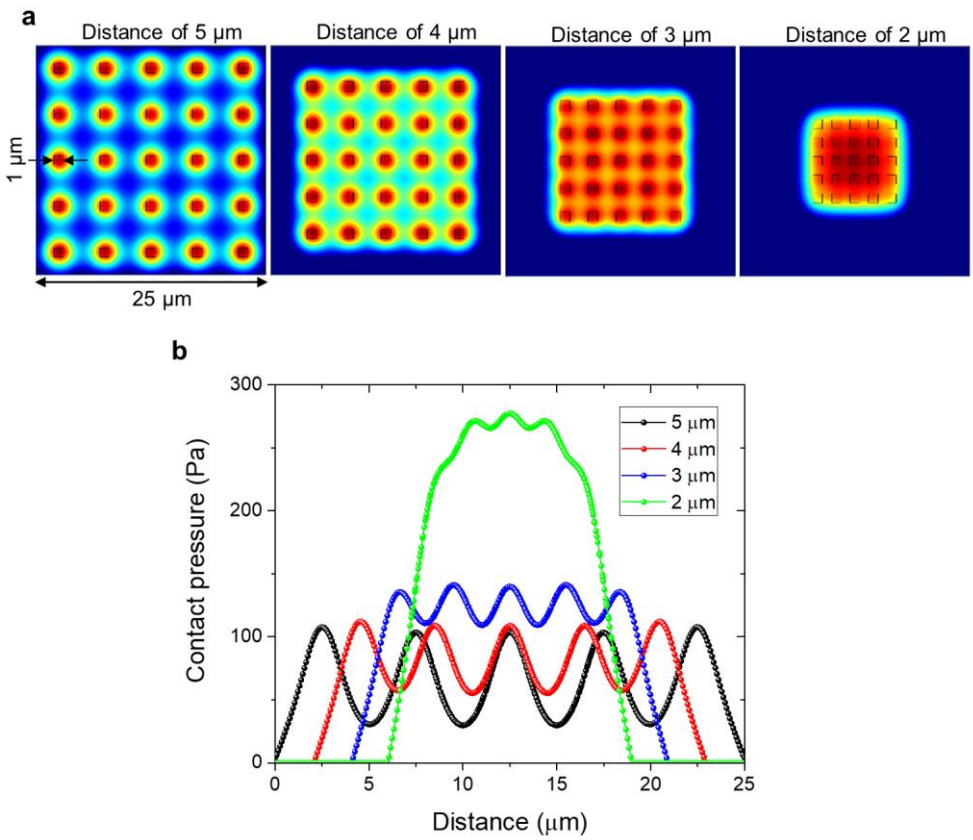

Figure 3.22 | Spatial resolution calculation [74]. a, FEA results showing P_{contact} between the two films when 1-μm-wide pillars with different distances pressed the top film with t_{top} = 1 μm. **b**, Line profiles (y = 12.5 μm) for the results in **a**.

profiles in Figure 3.22b. Due to the limited experimental environment, we were not able to obtain experimental evidence for this calculation, but it should be noted that the spatial resolution of the photonic skin far surpasses the experimentally measured value, *i.e.*, 1016 dpi, which could be observed by using higher-resolution micropillars and constructing an appropriate measuring system.

The results in this subsection reveal that “a pixel-less structure” and “ultrathin design” of the photonic skin are key to high-resolution analog imaging of pressure distribution unprecedented in previously reported pressure mapping devices. For a 1-μm-thick top film, a resolution of > 6000 dpi is calculated by the FEA, and the experimental results show a clear pressure map generated by micropillars of > 1000 dpi. Obviously, both values from the experiments and FEA are much higher than those of previous sensor-array-based pressure-mapping devices that are generally under 100 dpi. Table 3.1 summarizes the performance of various pressure-mapping/imaging devices including piezoelectric fluorescent materials, piezoelectric nanowire LEDs, and the photonic skin [7,11,82-88,90,92]. Although pressure-imaging devices using piezoelectric nanowire LEDs have achieved high pixel resolution (~6000 dpi) [87], their extremely low sensitivity, low fill factor, and lack of conformability hinder their practical applications. In particular, due to their low sensitivity (a few tens of GPa^{-1}), such devices cannot detect the practical pressure distribution applied by soft bodies such as a fingerprint. Furthermore, their low fill factor that is ~11% can cause critical distortion in sensing pressure distribution, for example, the pressure applied in a small area could not be detected. In contrast, due to the structural novelties, the pressure-sensitive photonic skin visualizes real-time high-resolution pressure image with an ultrafast response time (< 1 ms), a high fill factor (continuous spatial image), great sensitivity (> 10 kPa^{-1}), and a wide and practical pressure range (1 kPa – 1 MPa).

Table 3.1 | Comparison of pressure mapping devices [7,11,74,82-88,90,92].

Reference	Mapping type	Mechanism	Sensing type	Working range	Sensitivity	Spatial resolution	Spatial fill factor	Response time
[7] (2013)	Electrical Mapping	PSR and TFTs	Touch	-	-	~4 dpi (pixelated)	-	-
[11] (2014)	Electrical Mapping	Piezoresistive sensors	Real-time pressure	0.8 Pa – 10 kPa	133.1 kPa^{-1}	~4.2 dpi (pixelated)	-	< 50 ms
[92] (2019)	Electrical Mapping	Piezoresistive sensors	Real-time pressure	0 Pa – 200 kPa	0.97 kPa^{-1}	~5.1 dpi (pixelated)	-	24 ms
[82] (2010)	Electrical Mapping	PSR and NW TFTs	Real-time pressure	0 Pa – 15 kPa	~11.5 μS kPa^{-1}	~10 dpi (pixelated)	-	< 100 ms
[83] (2013)	Electrical mapping	Triboelectric sensors	Real-time pressure	2.1 Pa – 40 kPa	0.31 kPa^{-1}	~1 dpi (pixelated)	-	< 5 ms
[84] (2016)	Electrical mapping	Triboelectric sensors	Real-time pressure	1 kPa – 150 kPa	0.06 kPa^{-1}	5 dpi (pixelated)	-	70 ms
[85] (2017)	Electrical mapping Mechanoluminescent imaging	Triboelectric sensors (low pressure) Piezoelectric fluorescence (high pressure)	Real-time pressure (low pressure) Pressure change (high pressure)	60 Pa – 200 kPa 600 kPa – 20 Mpa	0.006 kPa^{-1} 0.000037 kPa^{-1}	100 dpi (pixelated)	-	50 ms ~9 ms
[86] (2013)	Electroluminescent Imaging	Pixelated OLED, TFT, and PSR	Real-time pressure	10 kPa – 100 kPa	42.7 Cd m^{-2} kPa^{-1}	~14 dpi (pixelated)	~44%	< 100 ms
[87] (2013)	Electroluminescent Imaging	Piezoelectric nanowire LEDs	Real-time pressure	~1 MPa –	12.88 GPa^{-1}	6350 dpi (pixelated)	11%	~90 ms
[88] (2015)	Electroluminescent Imaging	Piezoelectric nanowire LEDs	Real-time pressure	~1 MPa –	39.09 GPa^{-1}	6350 dpi (pixelated)	3%	-
[90] (2015)	Mechanoluminescent imaging	Piezoelectric fluorescence	Pressure change	1 MPa – 50 MPa	2.2 cps kPa^{-1}	254 dpi (pixelated)	25%	10 ms
[74] (2020)	Electroluminescent Imaging	Ultrathin layers of CNN and QLED	Real-time pressure	1 kPa – 1 MPa	10 kPa^{-1}	> 1000 dpi (continuous)	~100%	1 ms

The limitations of each technology are highlighted in red.

3.4.4 Demonstration of High-Resolution Pressure Imaging

Notably, this high-resolution and high-linearity pressure imaging enables 3D surface mapping of an elastic object because the contact pressure between the device and the elastic body is proportional to the compressive strain normal to the contact plane. For a proof of concept, a 3D surface of a mint leaf was mapped by capturing and processing of the image generated on the device where a PDMS replica of the mint leaf was fully pressed. Figure 3.23a illustrates the experimental setup, and Figure 3.23b and c present the optical images of the mint leaf and molded PDMS replica, respectively. Photographs in Figure 3.24 show that the device distinctly displayed the surface

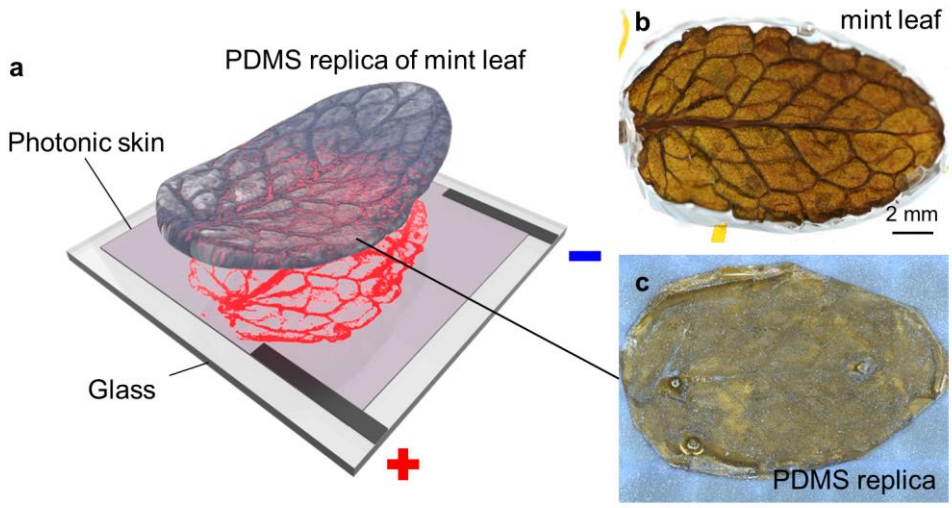

Figure 3.23 | Surface morphology imaging of a mint leaf replica [74]. a, Schematic illustration of the experimental setup for the surface morphology imaging of a mint leaf replica. **b**, Optical photograph of the original mint leaf. **c**, Optical image of the PDMS replica of the mint leaf.

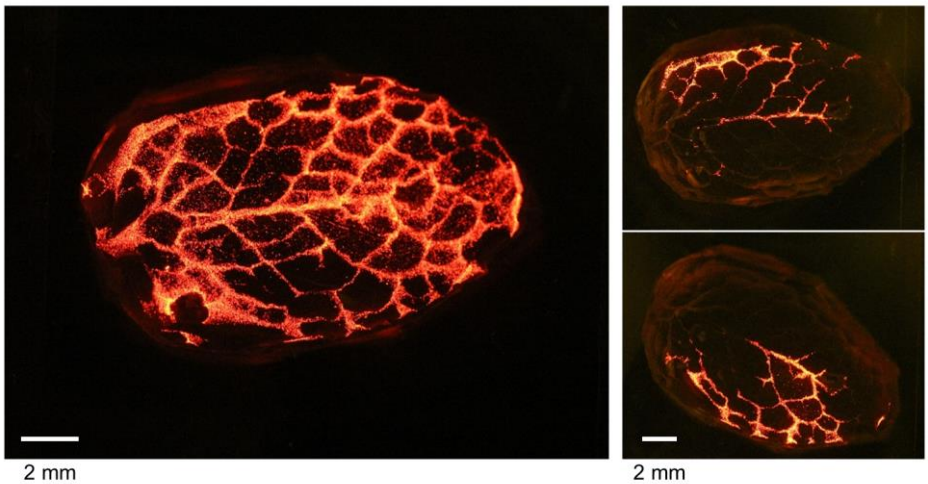

Figure 3.24 | Optical photographs of the photonic skin visualizing the pressure applied with a PDMS replica of a mint leaf when the replica was fully pressed and partially pressed [74].

morphology of the compressed part of the leaf replica, including major veins and a more detailed skeleton. The higher light intensity corresponds to the higher pressure and higher height of the PDMS replica. The as-captured image contains noise arising from the device uniformity and concentrated pressure peaks due to the microtextures of the leaf replica. Therefore, the Gaussian filter is applied to the captured image to remove the noise and micro-texture information, after which only the large-area morphology remained in the pressure image. Figure 3.25 shows the images Gaussian filtered with different standard deviations. The image filtered with higher standard deviation was much smoothed, where the detailed texture was completely removed. After the post-processing of the captured image, a 3D pixel intensity map was generated. Figure 3.26 compares the pixel intensity

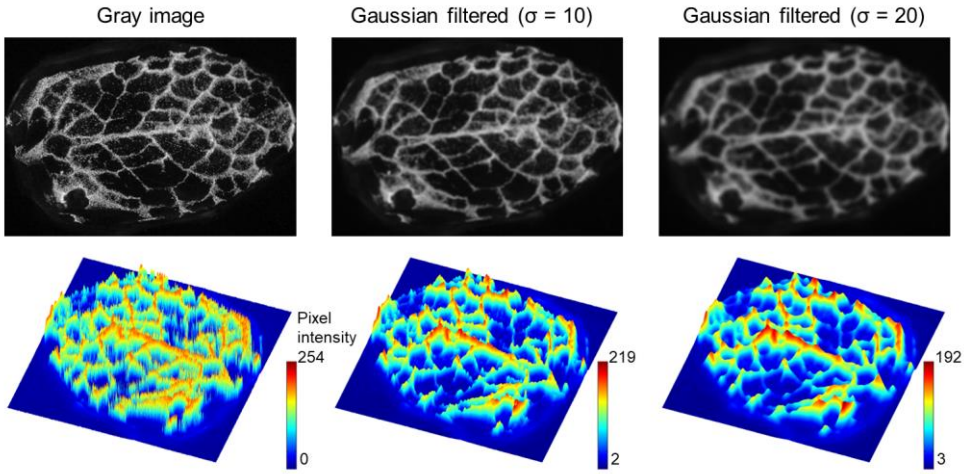

Figure 3.25 | Gaussian-filtered pressure images [74]. a, Greyscale image of the optical pressure image generated by the photonic skin when the mint leaf replica was fully pressed on it. **b** and **c**, Gaussian-filtered images of **a** using σ = 10 (**b**) and 20 (**c**).

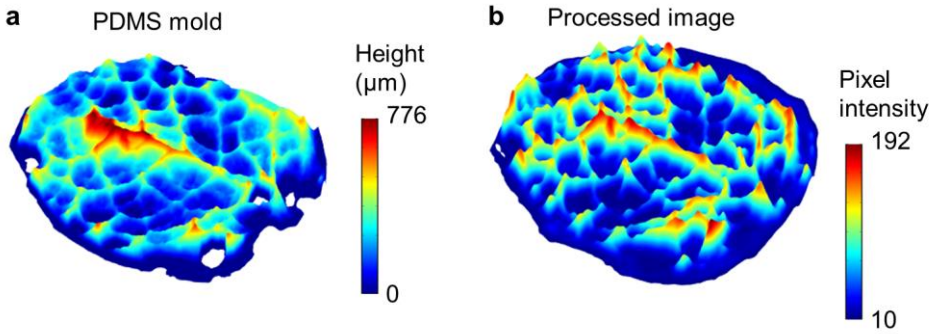

Figure 3.26 | Comparison between the mold surface and pressure image [74]. a, 3D surface image of the PDMS replica measured with a surface profiler. **b**, 3D plot of pixel intensity of the Gaussian-filtered image using σ = 20 in Figure 3.25c.

map with the 3D surface image of the PDMS replica measured using a surface profiler. The pressure image well represented the height map of the PDMS replica, proving the reliability of the pressure imaging of the photonic skin. The distortion mainly arose from the incomplete compression and the unevenly applied pressure.

Moreover, the photonic skin generates high-quality and high-contrast images of valuable micro-textures such as a fingerprint (Figure 3.27). A clear fingerprint pattern appeared with the light intensity corresponding to the touch force when the device was touched. Photonic skins with a green QLED and a yellow polymer light emitting diode (PLED) were also demonstrated, showing the universality of the method for photonic skin. The left photograph in Figure 3.27 shows a device with a green QLED touched with a finger. The right photographs in Figure 3.27 show a device with a yellow polymer light

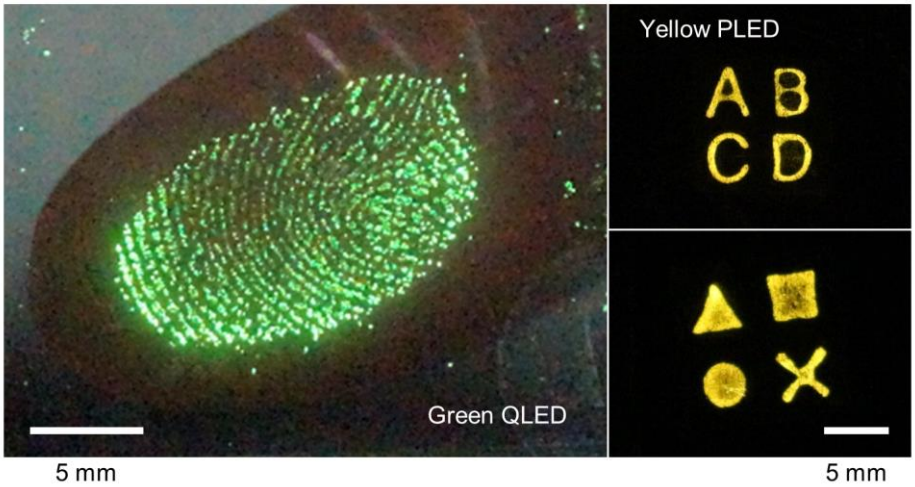

Figure 3.27 | Optical photographs of the photonic skins with various light-emitting devices, incuding a green QLED and yellow PLED [74].

emitting diode (PLED) touched with PDMS stamps. The most compelling advantage of the pressure-sensitive photonic skin is that it can operate while conformably laminated on 3D surfaces, just like “real skin.” The operation of the ultraflexible devices laminated on human skin and a plastic fiber is shown in Figure 3.28. When a finger and a glass rod touched the photonic skins attached onto the hand and the plastic fiber, they showed touch information in real time. The device also visualized the pressure at valleys of wrinkles generated around the location of touch, which could be a good example of the device visualizing even unintended force, implying its high sensitivity and reliability.

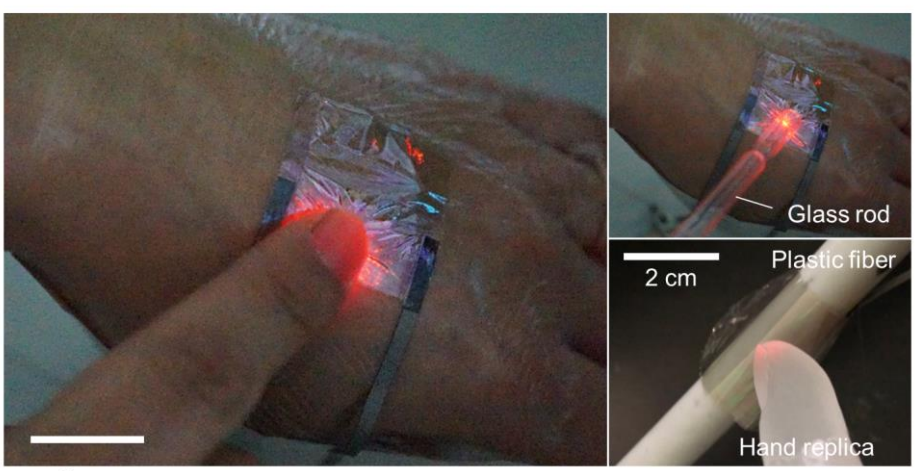

Figure 3.28 | Optical photographs of pressure imaging with freestanding devices laminated on various 3D surfaces [74].

3.4.5 Pressure Data Acquisition

This high-fidelity analog imaging with unprecedented response time (< 1 ms) can be rapidly digitized by digital imaging technologies (e.g., high-resolution charge coupled devices (CCDs)) in real-time, which could be challenging in high-resolution sensor arrays due to the complicated data acquisition process and scanning time of a large number of pixels. Once the light intensity distribution is captured, it can be transformed into actual pressure data based on a lookup table or pre-calibrated data. The luminance as a function of the applied pressure in Figure 3.7 is a great example of such lookup tables because the luminance is one of the absolute measurements of the light intensity. Alternatively, the pixel intensity from a CCD as a function of the applied pressure could be another simple option. For demonstration of the whole data transformation process, the digitized electroluminescent image was transformed into actual pressure distribution using a lookup table for pixel intensity (Figure 3.29). First, the mean pixel intensity was calculated for an electroluminescent image captured by a CCD for a specific uniform pressure applied with a 6×6 mm^2 square PDMS slab (Figure 3.29 a). Using this lookup table, the pressure distribution was directly calculated from the photograph captured by a CCD when the photonic skin was pressed with a B-shaped stamp (Figure 3.29b). For simplicity, the linear interpolation was used to calculate the pressure values between the two measured points. Figure 3.29c shows the pressure distribution data calculated from the photograph using the lookup table. This simple demonstration highlights the feasibility of the data transformation from the electroluminescent image of the photonic skin to the actual pressure distribution.

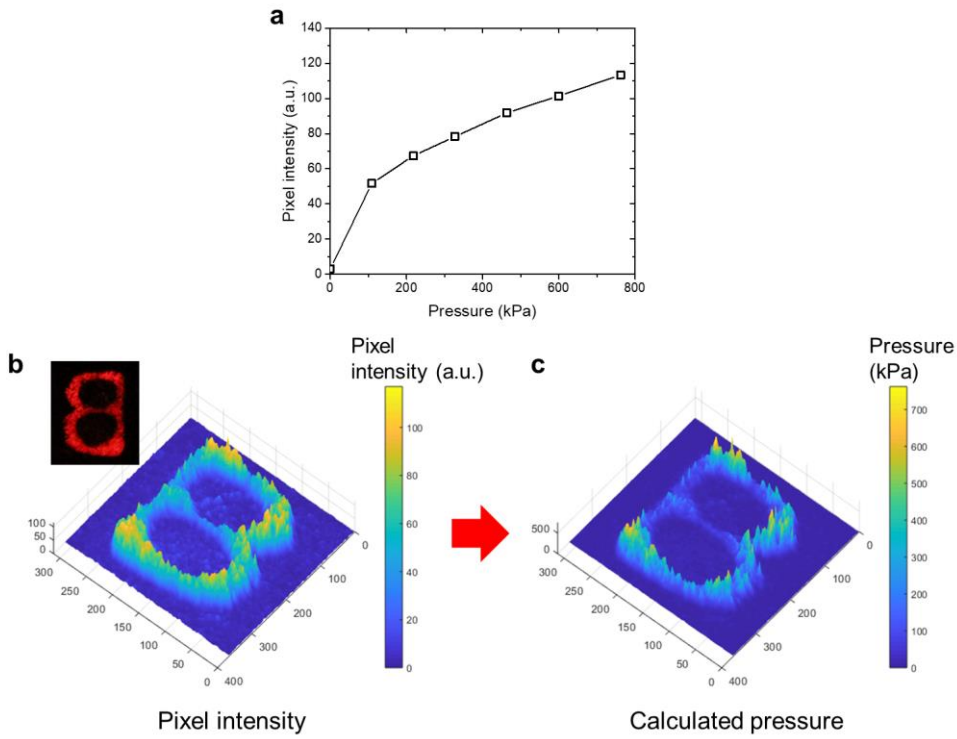

Figure 3.29 | Pressure data acquisition [74]. a, Pixel intensity as a function of the pressure applied with a 6 × 6 mm^2 PDMS slab under a bias of 15 V. **b**, Pixel intensity map of the photograph captured by a CCD when the photonic skin was pressed with a B-shaped stamp. **c**, Pressure distribution calculated from the photograph in **b** using the lookup table in **a**.

3.4.6 Application to Smart Touch Interfaces

Novel real-time high-information-density human-machine interfaces is further demonstrated using the photonic skin, namely, "smart touch interfaces." Figure 3.30a illustrates the concept of the smart touch interface, which is capable of identifying the user in addition to sensing the touch force and location in real time. In terms of the data dimension, it can be regarded as 4D touch interfaces compared to the 3D touch interfaces that can additionally detect touch force. From this type of touch interface, a variety of new machine actions could be generated. Furthermore, because the

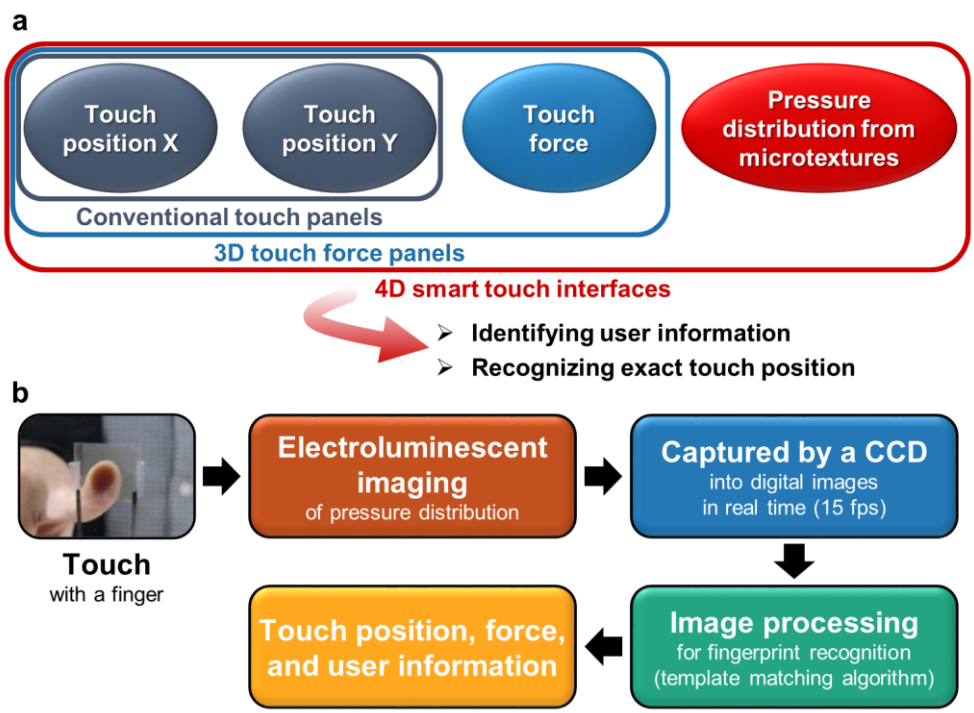

Figure 3.30 | Conceptual illustration of smart touch interfaces. a, Concept diagram of smart touch interfaces. **b**, Data transformation flow for smart touch interfaces.

microtexture information of the touch object can be recognized, the exact touch position can be obtained, and the unintended touch can be filtered. The data transformation flow of smart touch interfaces is explained in Figure 3.30b. When the photonic skin is touched with a finger, it visualizes the pressure distribution on it. Then the generated images are recorded by a CCD at 15 frames per second. These images are transferred to a computer that performs fingerprint recognition by a simple template matching algorithm and examines the exact touch location and relative force in real time. For a proof of concept, the device was touched with a finger three times with different positions, forces, and durations. The mean pixel intensities (MPIs) of the full image and the region detected as a fingerprint of the user are plotted as a function of the frame number in Figure 3.31a. Although the MPIs for both the full area and detected region well represented the relative touch force, the MPI of the detected region was more sensitive as a result of excluding the untouched area. Figure 3.31b shows the three frames containing the detected regions when the touch force reached the maximum value during each touch. These images show that the smart touch interface can calculate the exact location of the touch from the micro-texture information even if there is an unintended touch or the size of the contact area varies. The 3D plots of the pixel intensities in the detected regions in Figure 3.31c further provide the detailed fingerprint morphology and the associated pressure profile. This demonstration highlights the feasibility of fast and high-resolution pressure imaging with the photonic skin for demanding applications.

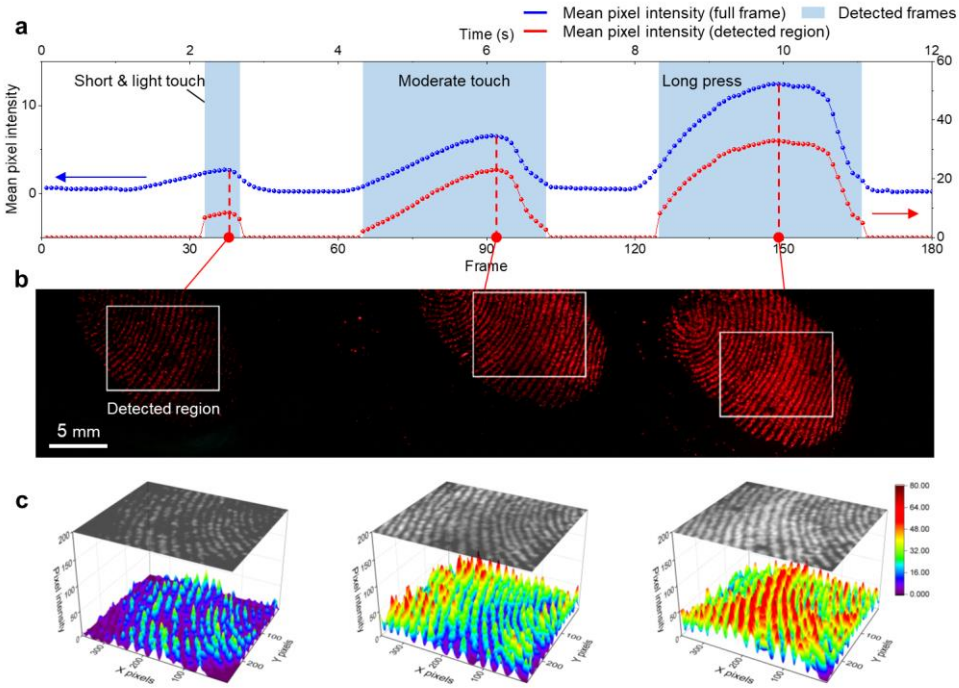

Figure 3.31 | Demonstration of real-time smart touch interfaces [74]. a, MPIs of the images captured by a CCD at 15 fps where the device was touched with a finger three times with different positions, forces and durations (blue dots: MPIs of full-size images, red dots: MPIs of the regions detected as a fingerprint of the user). **b**, Three frames containing the detected regions when the touch force reached the maximum value during each touch. White rectangles denote the regions detected as a fingerprint of the user. **c**, Pixel intensity maps for the Gaussian-filtered images (σ = 3) of the detected regions in **b**.

3.5 Conclusion

In summary, this chapter introduced the fully conformable and imperceptible electronics capable of imaging pressure distribution with high spatial and temporal fidelity without the need for pixel structures. The proposed pixel-less device offers numerous unique advantages that previous works employing patterned active pixels cannot realize. Owing to the homogeneous and ultrathin design, the device can transfer high-resolution pressure distribution into the light intensity distribution on a continuous surface. The ultrahigh sensitivity and great linearity of the CNN further facilitate high spatial fidelity of the pressure imaging. The results here provide a new experimental and theoretical framework for revealing an accurate stimulus profile by exploiting the conformability of an ultrathin film. Theoretical postulation and an FEA reveal that the top film acts as a spatial low-pass filter for the applied force and that the thickness of the film determines the spatial resolution. For a device with 1-μm-thick films, a resolution of > 6000 dpi is calculated by the FEA, and the experimental results reveal that the analog imaging of the device has a much higher resolution than 1000 dpi. Future work would include theoretical analyses of pressure transferring through a thin film, practical improvements in device performance such as encapsulation of the device, and integration with pre-established and emerging technologies such as microfluidics and deformable displays. These directions may satisfy the demand for fully understanding a spatial stimulus in future applications such as display-integrated advanced user interfaces, implantable bio-imaging systems, and nervous systems in soft robotics.

Chapter 4

Intrinsically Soft Heat Transfer and Electrical Interconnection Platforms Using Magnetic Nanocomposites

4.1 Introduction

Recently, self-powered wearable electronics have been demonstrated using various energy harvesting devices such as photovoltaic [8], piezoelectric [26], and triboelectric [27] generators. Although they show promising concepts and applications, these existing methods have at least one of the following limitations: low energy conversion efficiency, limited working conditions, or unstable waveforms of generated electricity. Thermoelectric generators (TEGs) have been regarded as one of the promising alternatives, due to their ability of continuous and stable power generation from body heat. Therefore, efforts to realize wearable forms of TEGs with flexibility or stretchability that could harvest thermal energy from 3D surfaces have been widely made [64-73].

The power harvested by a TEG can be written as $P = \frac{\eta_o(zT)}{T_{\mathrm{H}}} \Delta T_{\mathrm{TE}} Q_{\mathrm{TE}}$ [64], where η_o, T_{H}, ΔT_{TE} and Q_{TE} are the energy conversion efficiency depending on the figure of merit (zT) of TE materials, hot-side temperature, temperature difference across TE legs, and heat flow through the TE legs, respectively. The equation suggests that ΔT_{TE} is the most important factor for high TE performance with a given TE material and thermal energy. In other words, minimization of thermal impedance of the interface between TE materials and 3D heat sources are key to achieving a high energy conversion efficiency that can accelerate the realization of practical self-powered applications. However, previously reported flexible TEGs generally suffer from limited mechanical flexibility because they employ thick and rigid electrodes to interconnect TE legs [65-67,70]. Due to the poor conformability, the flexible TEGs form air gaps when they are attached to the curved surfaces. These air gaps cause significant heat loss, reducing the ΔT_{TE}. Alternatively, liquid metals, such as eutectic gallium-indium (EGaIn), have been exploited for soft interconnections [35,68], but their deleterious and unstable nature requires high-thermal-impedance polymer passivation, significantly impeding heat transfer to TE materials. Since elastomers generally have low thermal conductivity < 0.2 W m^{-1} K^{-1}, a large portion of total temperature difference is lost across the elastomer layers, resulting in low ΔT_{TE}. Figure 4.1 summarizes the technical issues of previous wearable TEGs. In this regard, for wearable TEGs to achieve high TE performance on 3D surfaces, an intrinsically soft and stretchable interconnection platform with efficient heat transfer strategy is highly required.

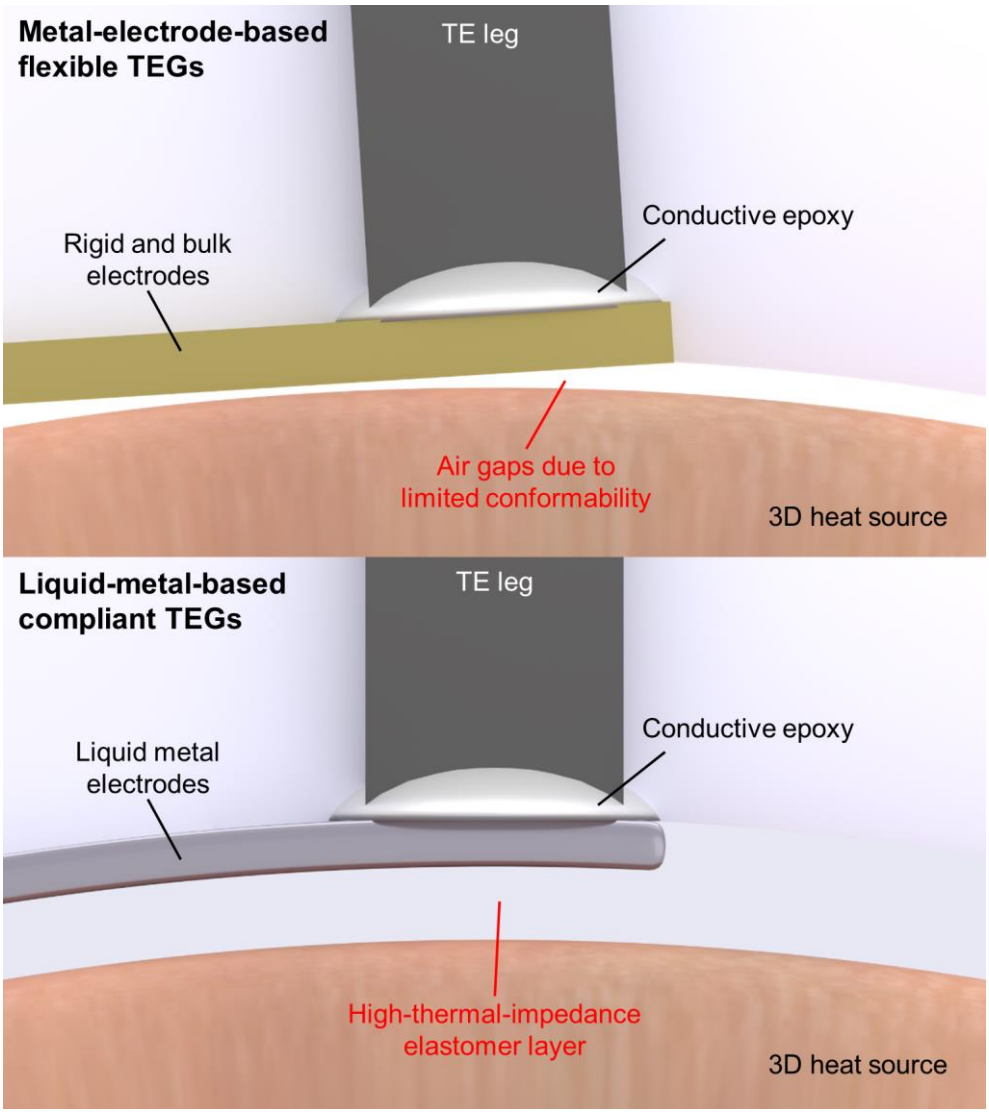

Figure 4.1 | Technical issues in interconnections and passivation of previous wearable TEGs.

In this chapter, as a novel solution for the issues mentioned above, an intrinsically soft heat transfer and electrical interconnection platform (SHEP) is introduced, where intrinsically stretchable electrodes and soft thermal conductors (STCs) are embedded. Figure 4.2 illustrates the concept and structure of the SHEP. The AgNW-based soft electrodes can vertically interconnect high-performance inorganic TE legs, effectively absorbing strain energy, which allows the TEGs to conform perfectly to 3D surfaces. Silver coated nickel microparticles (Ag-Ni MPs) magnetically self-assembled in elastomeric substrates form STCs that significantly enhance the heat transfer ability of the soft platform in the vertical direction, thereby maximizing TE performance of the TE legs. Especially the embedding of the AgNW network and self-assembly of the Ag-Ni MPs are simultaneously achieved during a single curing process of the PDMS matrix, providing a time-saving and reliable method for reproducible SHEPs. Due to the enhanced mechanical conformability and heat transfer ability, unprecedentedly conformal contact

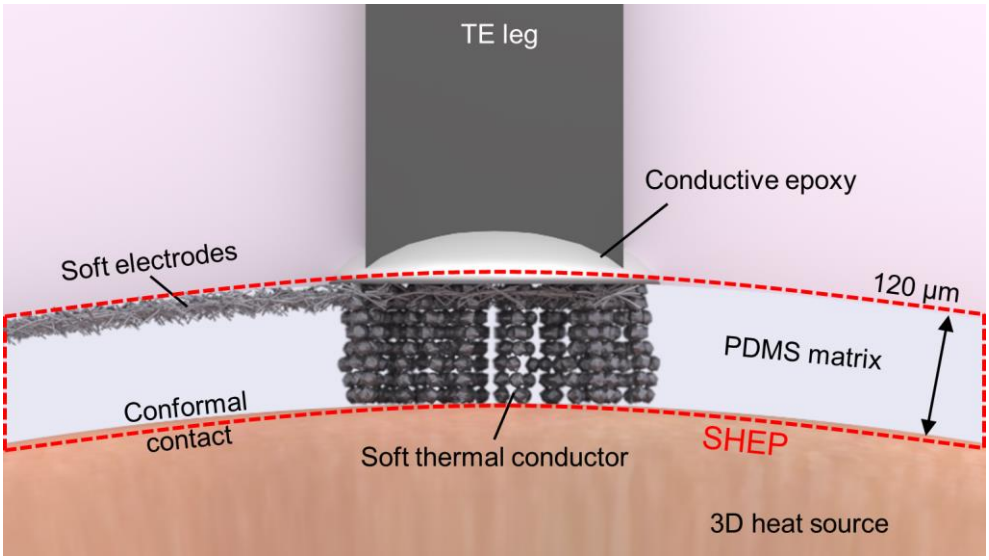

Figure 4.2 | Conceptual illustration of the SHEP.

between TEGs and 3D heat sources and high energy conversion efficiency of the TEGs on them can be achieved. In this chapter, the methodologies, morphology, and mechanical characteristics of the SHEP are covered in detail. In particular, the process parameters and optimization of them for the reliable and reproducible formation of the SHEP are intensively discussed. Furthermore, enhancement of heat transfer ability of the soft platform through self-assembly of ferromagnetic particles is systematically investigated. In Chapter 5, mechanically compliant TEGs using SHEPs will be proposed, and the enhanced heat transfer from 3D heat sources to TE legs *via* improved conformability will be further investigated.

4.2 Experimental Section

4.2.1 Fabrication of SHEPs

Figure 4.3 illustrates the fabrication process of the SHEPs. Before depositing AgNW electrodes, surface treatment with vapor-deposited FOTS was conducted on a 125-μm-thick polyethylene terephthalate (PEN) carrier substrate to ensure sufficient hydrophobic properties that facilitate detachment of the AgNW electrodes. On the prepared PEN substrate, which was on a 70 °C hot plate, 2 mL of a AgNW solution was spray-coated using a patterned metal mask and a portable airbrush (DH-125, Sparmax). Ag-Ni MPs were mixed in PDMS and curing agent with 10:1 in weight ratio using a paste mixer (ARE-310, Thinky). The Ag-Ni MPs/PDMS precursor mixture was poured onto an FOTS-treated 400-μm-thick glass substrate with 120-μm-thick spacers. The prepared AgNW-coated PEN was placed on top of the mixture. The mixture covered by the PEN substrate was sandwiched by two iron pillar arrays (1.2 × 1.2 mm^2 pillar, 9 × 9 arrays) and a designed mold, and then, two vertically aligned magnets were attached at the top and bottom of the pillar arrays. The magnetic flux intensity of two magnets was ~1600 G for all STCs fabricated in this work, if not specified. After sufficient resting (~10 min), the static mixture was cured in a 100 °C oven for 1 h, maintaining the magnetic field until the curing process was completed. After curing the mixture and detaching the PEN substrate, a SHEP on the supporting glass was produced.

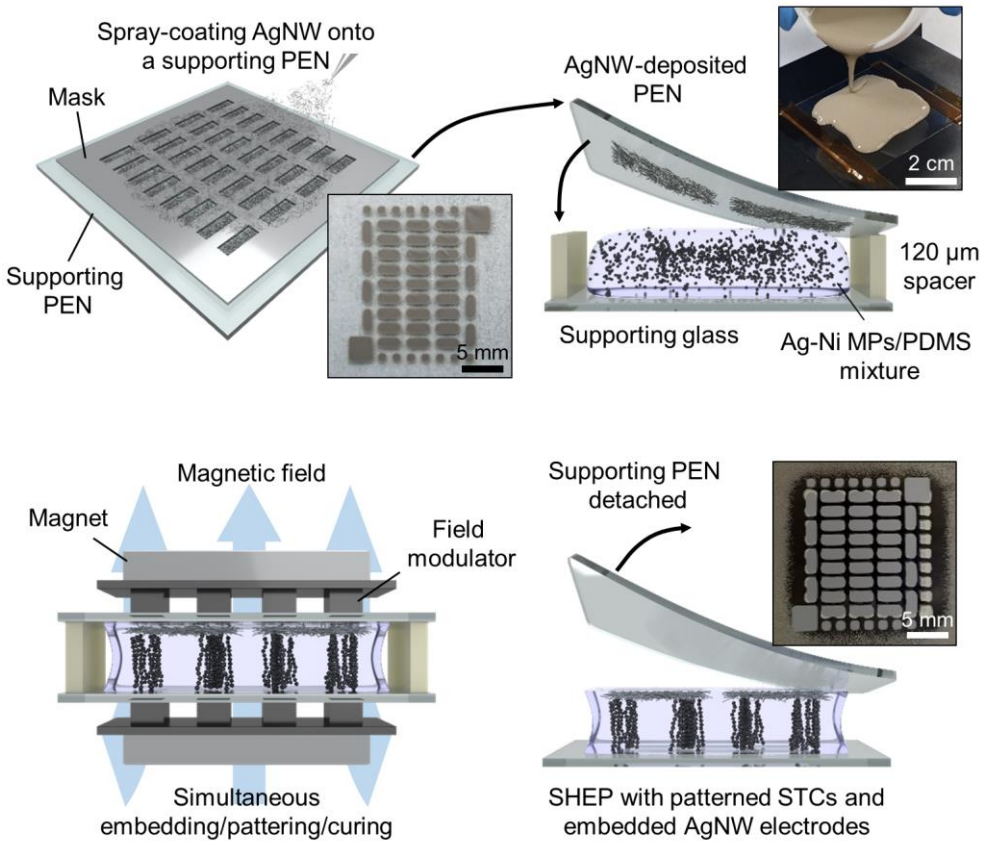

Figure 4.3 | Schematic illustration of fabrication process of the SHEPs.

4.2.2 Measurements

Thermal conductivities. The thermal conductivity was characterized from the measurements of the density, specific heat, and thermal diffusivity of the bulk STCs. The density was measured according to the standard test methods for density and specific gravity of plastics by displacement (ASTM D792) using an electronic densimeter (MD-300S, Alfa Mirage). The specific heat was measured according to Plastics-Differential scanning calorimetry (DSC) – Part 4: Determination of specific heat capacity (ISO 11357-4) using DSC equipment (DSC 25, TA). The thermal diffusivity was measured according to the standard test method for thermal diffusivity by the flash method (ASTM E1461) using a thermal diffusivity measurement system (NETZSCH, LFA 447 NanoFlash).

Strain-Stress curves. Strain-stress curves of the STCs with different Ag-Ni weight ratios (50, 60, and 70 wt%) were compared to those of a bare PDMS layer and commercially available thermal pads (H48-2K, H48-6G, and TGX, t-Global Technology). Tensile strain tests were conducted using a universal testing system (UTM, Instron 5567, Instron) with a strain rate of 20 mm/min. The width, length, and thickness of the STCs were 10 mm, 20 mm and 0.1 mm, respectively. In case of commercial thermal pads, the width and length of the counterparts were the same as those of the STCs, but the thicknesses were different (H48-2K, H48-6G, and TGX: 0.1 mm, 0.3 mm, and 0.5 mm thicknesses, respectively).

Optical, IR, SEM and EDS observations. Surface and cross-section images of the STCs with AgNW interconnections were captured using optical microscopy (DSX510, Olympus). The real-time heat transfer of the STCs was examined using an infrared thermal imaging camera (T420, FLIR Systems). The distribution images of Ag-Ni MPs in the PDMS layers with and without magnetic self-assembly were captured using scanning electron microscopy (SEM, Sigma 300, ZEISS) and analyzed by energy dispersive spectrometry (EDS, XFlash6160, Bruker).

4.3 Results and Discussion

4.3.1 Fabrication Scheme and Morphology of SHEPs

The most compelling feature of the fabrication method for SHEPs is that the magnetically self-assembled STCs, and AgNW-based stretchable electrodes are simultaneously formed in a PDMS matrix during a single curing process. After the Ag-Ni MPs/PDMS precursor mixture on a supporting glass was covered by the AgNW-deposited PEN substrate, they were sandwiched with two iron pillar arrays, and two magnets were attached to the top and bottom of the pillar arrays. Figure 4.4 illustrates the magnetic movement of the Ag-Ni MPs in the PDMS precursor mixture, where the magnetic field is applied through the iron pillar array. Because the magnetic field is concentrated on

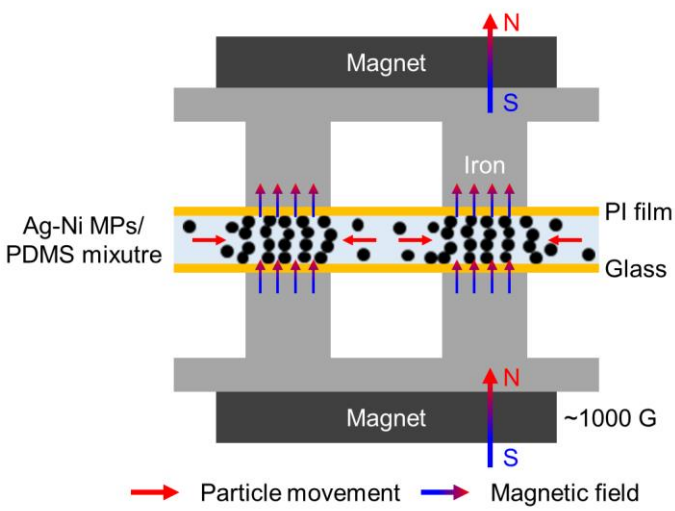

Figure 4.4 | Schematic illustration of the movement of Ag-Ni MPs in the PDMS mixture under the magnetic field applied through the iron pillar arrays.

the vertically aligned iron pillars as shown in the simulation result with a FEA (Figure 4.5), Ag-Ni MPs rapidly converge into the location of the iron pillar couples. At the same time, the MPs between the upper and lower pillars are self-assembled, forming well-defined vertical chains, *i.e.*, percolation paths, in the PDMS mixture. The heat transfer in the through plane direction is significantly enhanced through these vertically connected chains. In this regard, the patterned magnetic field is key to realize patterned heat-conducting paths. Because the magnetic field was applied from before the curing process, the Ag-Ni MPs could freely travel in the uncured PDMS precursor matrix. This behavior was completed as soon as the magnetic field was applied (< ~180 sec), and then the Ag-Ni MPs did not move anymore. After sufficient resting, the static mixture was cured, maintaining the magnetic field until the curing process was completed. Finally, a SHEP containing AgNW electrodes and STCs on the supporting glass was obtained by detaching the magnets, field modulators, and PEN substrates.

The SHEP formation process is fairly simple, highly customizable, and reproducible. The design of STC patterns can be facilely modulated by employing different iron pillar arrays. The Ag-Ni MP concentration in the STC patterns that determines the heat transfer ability can be easily adjusted by changing the volume fraction of the Ag-Ni-PDMS mixture (Subsection 4.4.2). Furthermore, the potential parameters that affect the TE performance, such as magnetic flux intensity and PDMS viscosity, were elaborately optimized to be in the middle of the process window, rendering the process more stable and reliable under ambient conditions (Subsection 4.4.5).

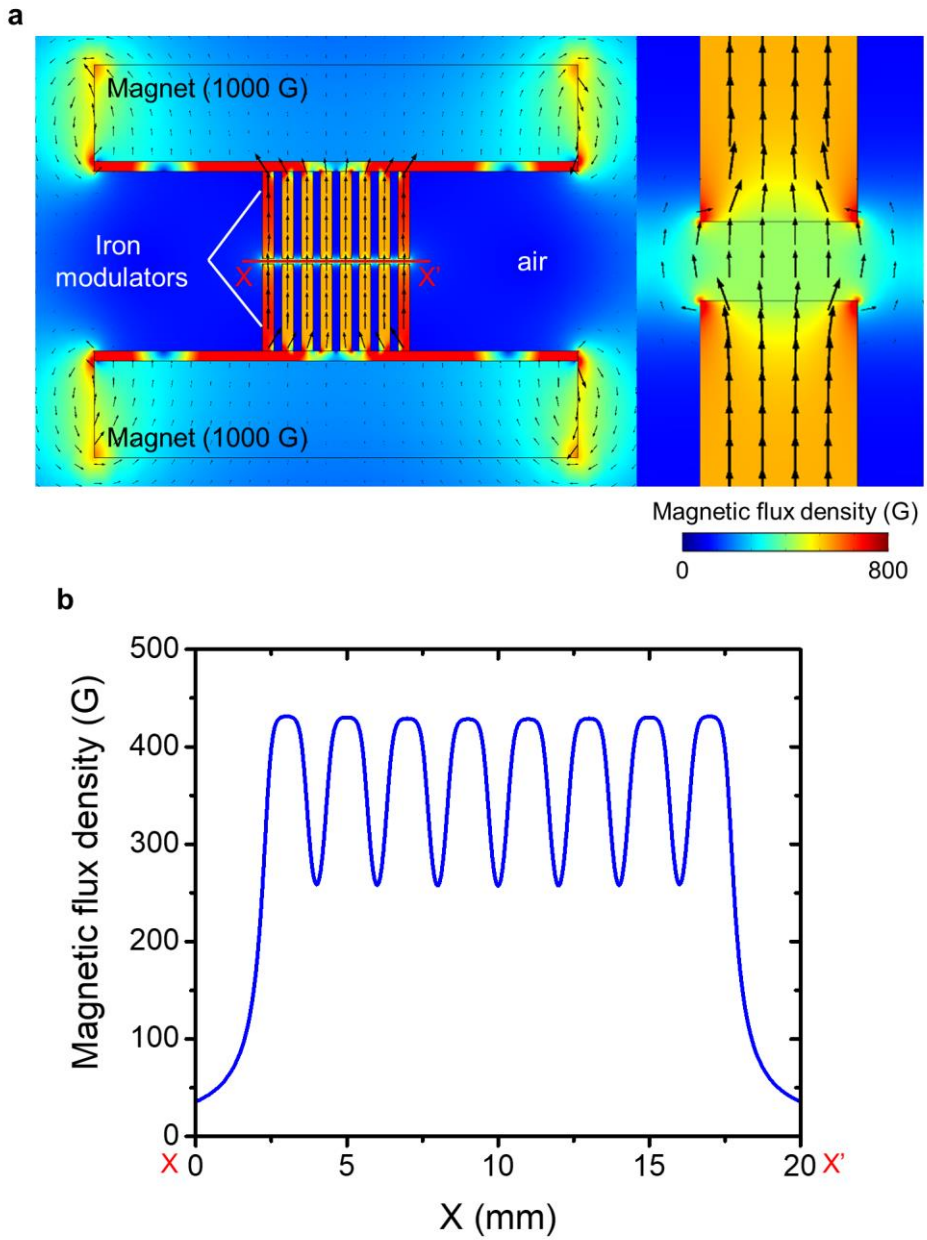

Figure 4.5 | FEA for the patterned magnetic field. a, FEA results showing the magnetic flux intensity when the magnets were attached to the both sides of the two iron pillar arrays. **b**, Line profile of the magnetic flux intensity at the line xx' in **a**.

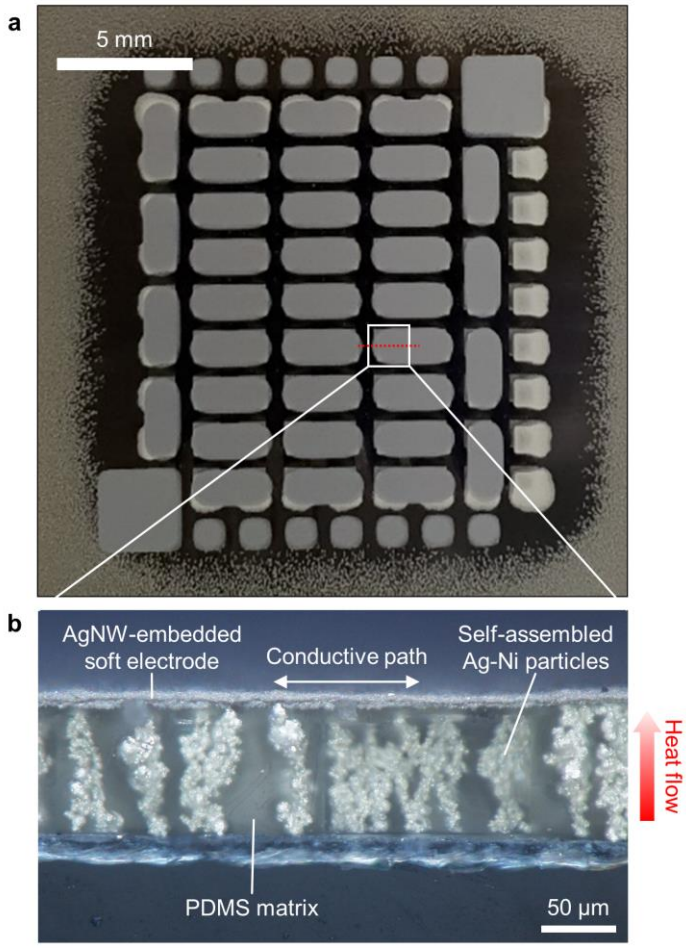

Figure 4.6 | Optical images of the SHEP. a, Top-view of the SHEP. **b**, Cross-section of the SHEP.

Optical images in Figure 4.6 show the fabricated SHEP, where the STC and stretchable electrodes are imbedded. The patterned electrodes and STCs are perfectly aligned, as shown in the top-view optical image in Figure 4.6a. Figure 4.6b shows the cross-sectional view of the SHEP. The thickness of the SHEP was ~120 μm that was the same as the thickness of the spacers. The AgNW random network embedded in the PDMS matrix is shown at the top surface of the cross-section. The thickness of the AgNW network is < 10

μm. The random network embedded in the elastomer can reliably conduct electricity even when tensile strain is applied to the platform. The cross-sectional image clearly show the vertical chains of the Ag-Ni MPs that were self-assembled by the patterned magnetic field. These chains are key to enhancement of heat transfer through the soft platform. The SEM images in Figure 4.7 compare the cross-sections of the Ag-Ni MP/PDMS composites with and without magnetic self-assembly. While the composite without self-assembly has the particles randomly and independently distributed in it, the magnetically self-assembled composite has the well-defined vertical chains of the interconnected particles. The EDS image in Figure 4.7 shows that the chains comprise the Ag-Ni MPs.

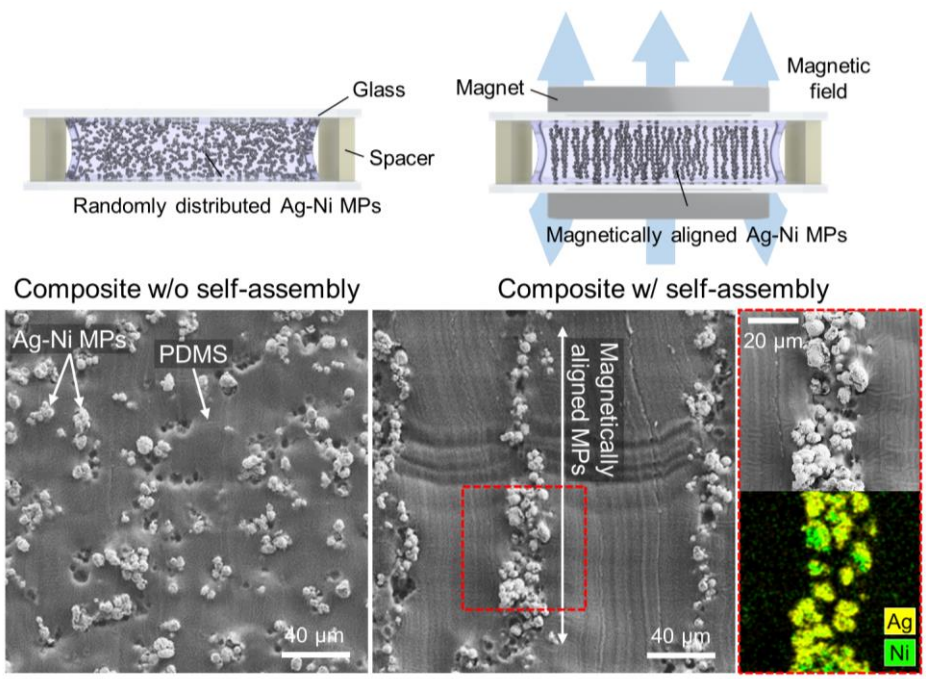

Figure 4.7 | SEM images of bulk composites without and with magnetic self-assembly.

4.3.2 Calculation of Particle Concentration in STCs

The Ag-Ni MP concentration in the STCs needs to be calculated to investigate the heat transfer ability of the STCs. Because randomly distributed Ag-Ni MPs in a PDMS precursor converged at the iron pillar locations by the patterned magnetic field, the concentration of the Ag-Ni MP in the STC areas is much higher than the initial concentration. In particular, all particles outside the pillar areas moved inside the closest pillar areas, forming the same square patterns with the pillar areas. For the calculation of the Ag-Ni MP concentration in the square pattern, we defined a "unit area" as indicated in red rectangles in Figure 4.8a and b, and a "patterned area" that corresponds to the area of the iron pillar (blue rectangles in Figure 4.8a and b). Since the iron pillars are placed with a regular interval, and the Ag-Ni MPs were uniformly mixed with a PDMS precursor, the same amount of the particles in each unit area converged at each patterned area for all of the iron pillars. Note that there remained no particles in the area between the patterned areas, as shown in Figure 4.8b. The Ag-Ni MP concentration in the patterned area is calculated using the initial volume fraction and the ratio between the unit and patterned area. Because the same amount of PDMS and Ag-Ni MPs are mixed, the initial weight concentration of the mixture can be described as follows:

$$\frac{M_{\mathrm{AgNi}}}{M_{\mathrm{AgNi}}+M_{\mathrm{PDMS}}} = 50\ \mathrm{wt\%} \tag{4.1}$$

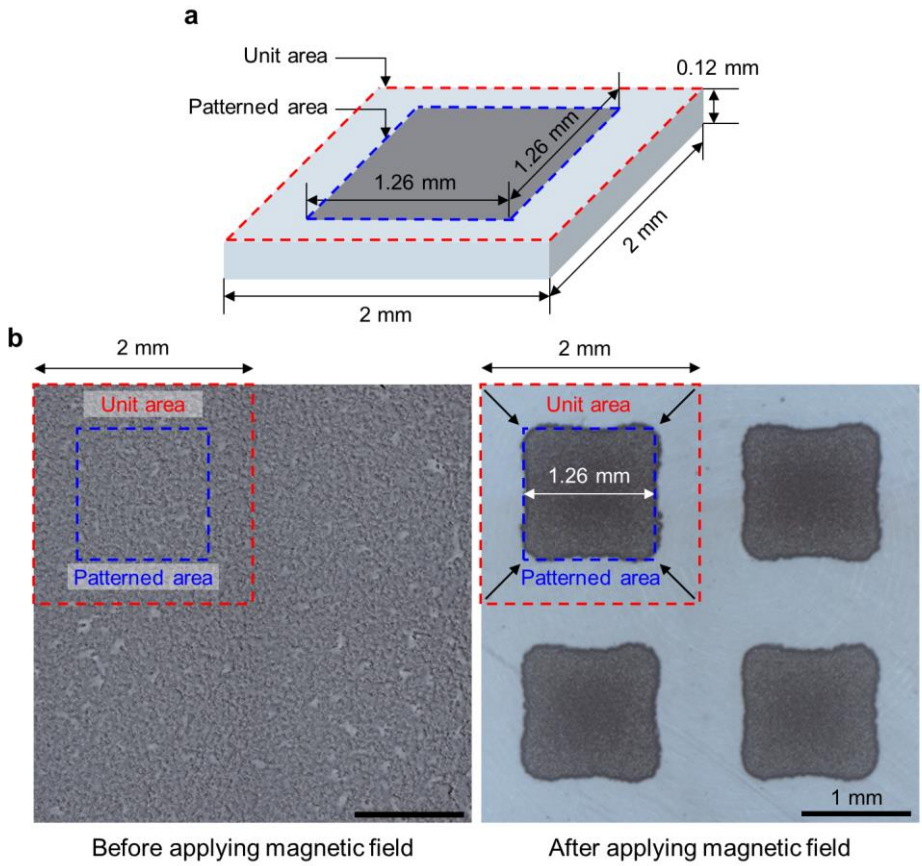

Figure 4.8 | Ag-Ni MP distribution before and after the magnetic self-assembly. a, Schematic image defining a unit area and patterned area for each STC pattern. **b**, Optical images showing Ag-Ni MP distribution before and after the magnetic self-assembly.

where M_{AgNi} and M_{PDMS} are the mass of Ag-Ni MPs and PDMS, respectively. The volume ratio can be calculated for the given mass of the Ag-Ni MPs and PDMS using the relation between volume and mass as follows:

$$\frac{V_{\mathrm{AgNi}}}{V_{\mathrm{AgNi}}+V_{\mathrm{PDMS}}} = \frac{M_{\mathrm{AgNi}}/D_{\mathrm{AgNi}}}{M_{\mathrm{AgNi}}/D_{\mathrm{AgNi}}+M_{\mathrm{PDMS}}/D_{\mathrm{PDMS}}} = 25.79\% \qquad (4.2)$$

where V_{AgNi} and V_{PDMS} are the volume and D_{AgNi} (2.776 g/cm^3) and D_{PDMS} (0.965 g/cm^3) are the densities for Ag-Ni MPs and PDMS, respectively. After the magnetic self-assembly, as the Ag-Ni MPs converge from the unit area to the patterned area, the increased volume concentration is calculated by considering the volume ratio between the unit and patterned areas. Because the thickness is same before and after magnetic self-assembly, only the areas of the unit and patterned area need to be considered. The increased volume concentration can be described as follows:

$$F = \frac{V_{\mathrm{AgNi}}}{V_{\mathrm{AgNi}}+V_{\mathrm{PDMS}}} \times \frac{A_{\mathrm{Unit}}}{A_{\mathrm{Pattern}}} = 64.98\% \tag{4.3}$$

where A_{Unit} (4 mm^2) and $A_{Pattern}$ (1.588 mm^2) are the areas of the unit and patterned area. The weight concentration after magnetic self-assembly can be expressed using Equation 4.3 and densities of the materials as follows:

$$\frac{D_{\mathrm{AgNi}} \cdot F}{D_{\mathrm{AgNi}} \cdot F + D_{\mathrm{PDMS}} \cdot (1-F)} = 84.23 \text{ wt\%} \tag{4.4}$$

The calculated concentration in Equation 4.4 is much higher than the initial concentration of 50 wt%. Together with a chain-like morphology of self-assembled Ag-Ni MPs, this increased MP concentration in the patterned area plays an important role in enhancing the heat transfer ability of STCs.

4.3.3 Enhancement of Heat Transfer Ability *via* Magnetic Self-Assembly

To investigate the heat transfer ability of the STCs, the thermal conductivity of bulk Ag-Ni-PDMS composites, *i.e.*, composites not spatially patterned by the iron pillar arrays, was systematically analyzed as a function of the Ag-Ni MP concentration and with and without magnetic self-assembly. Figure 4.9 shows the through-plane thermal conductivity ($K_{\mathrm{Thru-plane}}$) of the composites with different conditions. The $K_{\mathrm{Thru-plane}}$ of the composite increased from 0.15 to 0.53 W m^{-1} K^{-1} as the Ag-Ni MP concentration increased form 50 wt% to 70 wt%. Interestingly, the $K_{\mathrm{Thru-plane}}$ values of

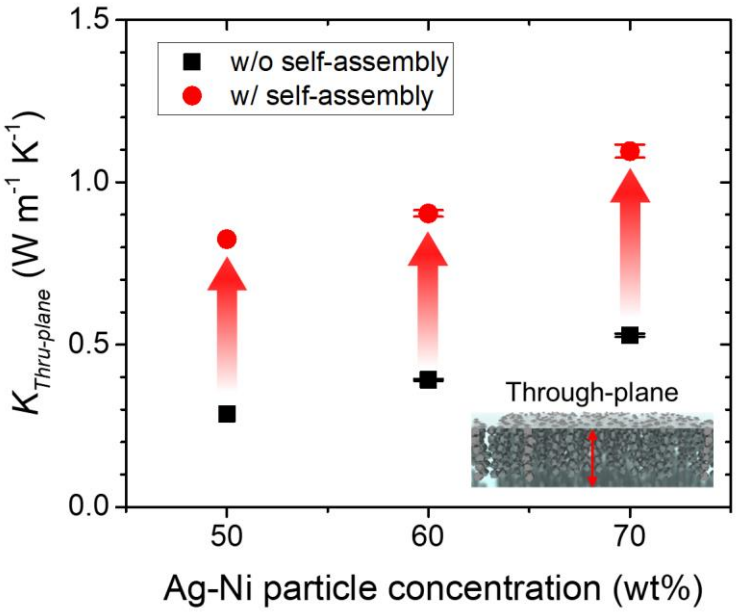

Figure 4.9 | Through-plane thermal conductivity as a function of Ag-Ni particle concentration without and with magnetic self-assembly.

all composites drastically jumped after magnetic self-assembly. For example, the $K_{\mathrm{Thru-plane}}$ of the 70 wt% composite increased from 0.53 W m^{-1} K^{-1} to 1.1 W m^{-1} K^{-1} upon magnetic self-assembly. This result is primarily due to the greatly increased number of vertical percolation paths arising from the applied magnetic field, as shown in the SEM images in Figure 4.7. Figure 4.10 shows the in-plane thermal conductivity ($K_{\mathrm{In-plane}}$) of the bulk composites. The composites without magnetic self-assembly showed $K_{\mathrm{In-plane}}$ > 1 W m^{-1} K^{-1}, which is much higher than $K_{\mathrm{Thru-plane}}$; this result could be attributed to the inhomogeneous Ag-Ni MP distribution in the vertical direction due to the force of gravity during the curing process. After magnetic self-assembly, as high-density Ag-Ni MPs at the bottom of the

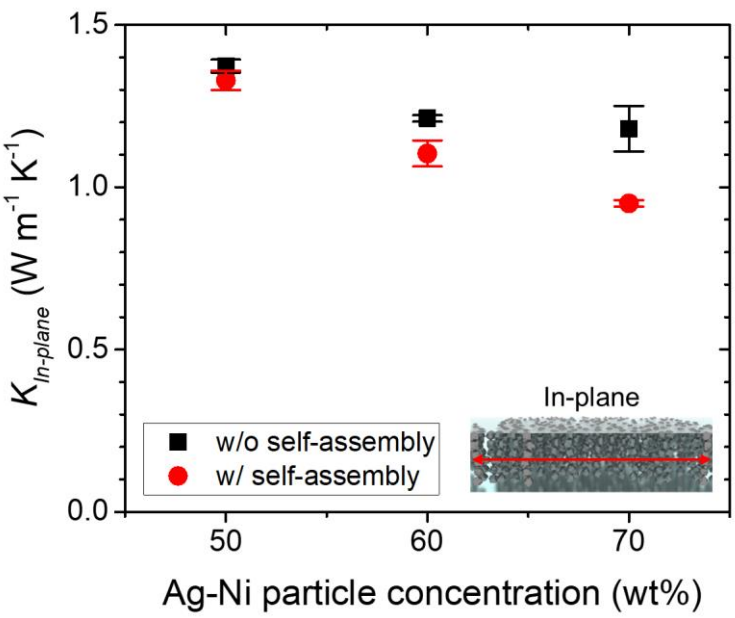

Figure 4.10 | In-plane thermal conductivity as a function of Ag-Ni particle concentration without and with magnetic self-assembly.

composite participated in the vertical chains along the direction of the magnetic field, $K_{\mathrm{In-plane}}$ slightly decreased. It should be noted that the strategy exploiting magnetic self-assembly of Ag-Ni MPs effectively improved $K_{\mathrm{Thru-plane}}$, which is closely related to the ability to transfer heat to the TE legs, without a significant loss in $K_{\mathrm{In-plane}}$. Furthermore, the Ag-Ni MP concentration in the patterned STC areas increased up to ~84 wt% after magnetic patterning process as described in Subsection 4.4.2. The accurate thermal conductivity of the patterned STCs could not be experimentally obtained due to the limitation of our measurement system in terms of required dimensions and the difficulty in fabricating a bulk composite containing > 75 wt% Ag-Ni MPs. Therefore, a $K_{\mathrm{Thru-plane}}$ of ~1.4 W m^{-1} K^{-1} for a Ag-Ni MP concentration of 85 wt% was extracted from the extrapolation of the measured data in Figure 4.9. This thermal conductivity is comparable to that of a Bi_2Te_3 leg (~1.9 W m^{-1} K^{-1}). These results suggest that the heat transfer ability of the STCs in the SHEP is much superior to those of previously reported soft substrates, such as PDMS and engineered Ecoflex, and even comparable to those of commercial thermal pads.

This enhanced heat transfer ability of the STCs was also observed in a SHEP with a patterned STC array. Figure 4.11 presents the thermograms of the SHEP with spatially patterned STCs on a hot plate. The SHEP was placed on the 70 ºC hot plate at 0 s and the top surface of the SHEP was captured by an infrared camera in real time. The temperature of the surfaces of the STC pixels increased faster than that of the non-pixel area (bare PDMS matrix), suggesting the enhanced heat transfer ability of the STC pixels.

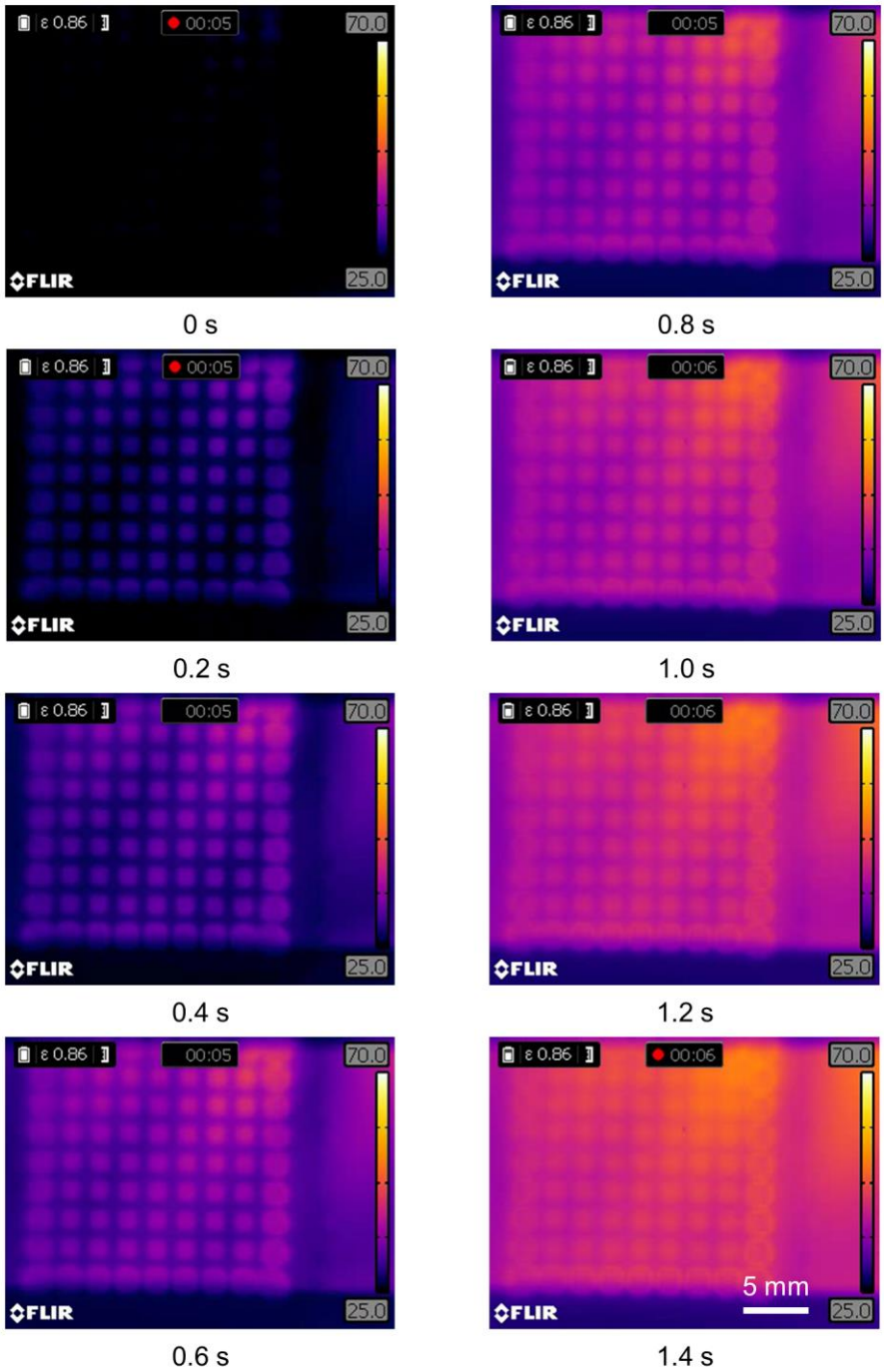

Figure 4.11 | Thermograms of the SHEP with spatially patterned STCs abruptly placed on a hot plate.

4.3.4 Softness of STCs

The softness and elastic deformation of the STC are of great importance for the conformability of the SHEPs and compliant TEGs using them because the low Young's modulus lowers the flexural rigidity of the system. Therefore, the softness and fracture strain of the STCs were investigated. Figure 4.12 presents the strain-stress curves of bare PDMS and magnetically self-assembled Ag-Ni-PDMS composites with different Ag-Ni MP concentrations. As the MP concentration increased, the Young's modulus of the composite also increased. However, they maintained their Young's modulus < 10 MPa even when the MP concentration reached 70 wt%. Furthermore, a fracture

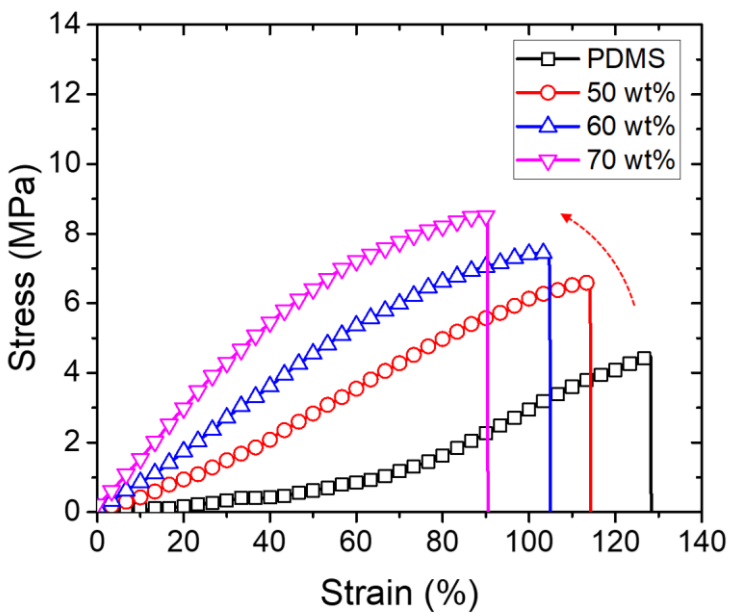

Figure 4.12 | Strain-stress curves of bare PDMS and magnetically self-assembled Ag-Ni-PDMS composites with different Ag-Ni particle concentrations.

strain of the composite was also maintained > 90%. The softness and the fracture strain are comparable to those of most elastomers. These results suggest that the approach exploiting self-assembly of the ferromagnetic particles in an elastomer matrix for realizing STCs effectively enhances their thermal conductivity without significantly compromising their softness. They exhibit higher stretchability than most of the reference commercial thermal pads as shown in Figure 4.13.

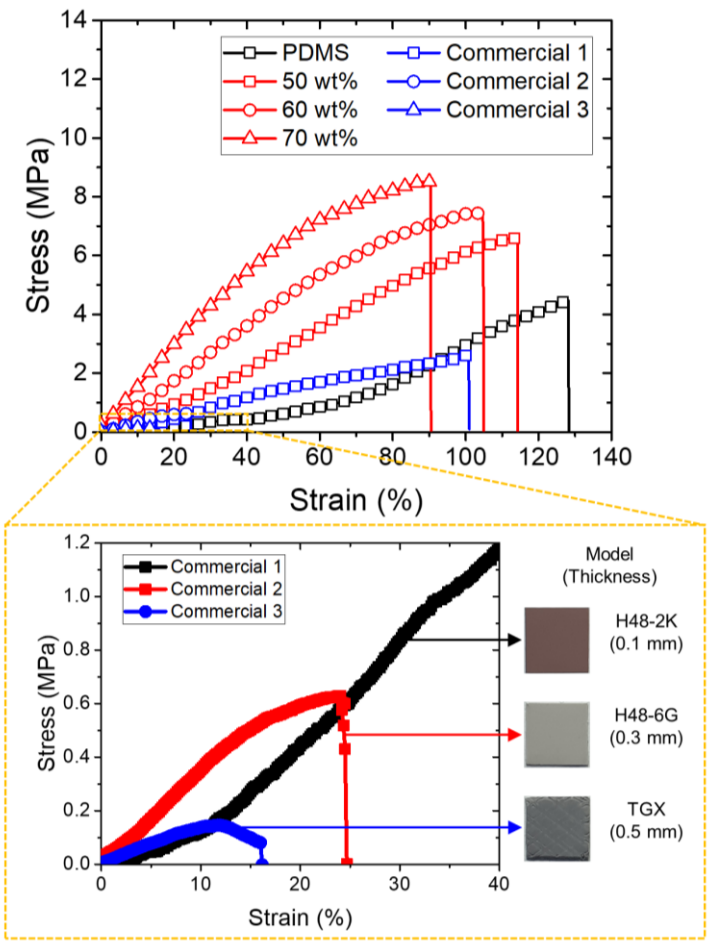

Figure 4.13 | Comparison of strain-stress curves of the STCs and commercial products.

4.3.5 Mechanical Reliability of Stretchable Electrodes

The mechanical reliability of the AgNW-based stretchable electrodes is experimentally investigated. Figure 4.14a illustrates the mechanism of the AgNW-based intrinsically stretchable electrodes. When the tensile strain is applied to the elastomer composites containing AgNW random networks (SEM image in Figure 4.14b), the AgNWs slides in the elastomer matrix, maintain their connections. The important requirement for minimizing conductance change here is that each nanowire should not snap in the elastomer matrix when the strain is applied. Therefore, careful optimization is needed in terms of the diameter and average length of the nanowire. In particular, if the nanowires are too long and too thin, the possibility of the break of each nanowire increases. Hence, the nanowires with a diameter of 100 nm were used, and the length of the nanowires was reduced < 10 μm using a tip sonication method. After further optimization of the process parameters such as the thickness of the random networks and spraying conditions, the high reliability of the AgNW random networks in the PDMS matrix was achieved. The sheet resistance of the resulting electrodes was ~1 Ω sq^{-1}. After a few aging cycles with a strain of 100%, the 1000 stretching cycles with 60% strain for a cycle test were applied to the composite. The stretching speed was 200 mm min^{-1}. Figure 4.14c shows the resistance change of the intrinsically stretchable electrodes during the cycle test. It kept its resistance change < 100% of initial resistance during the 1000 cycles.

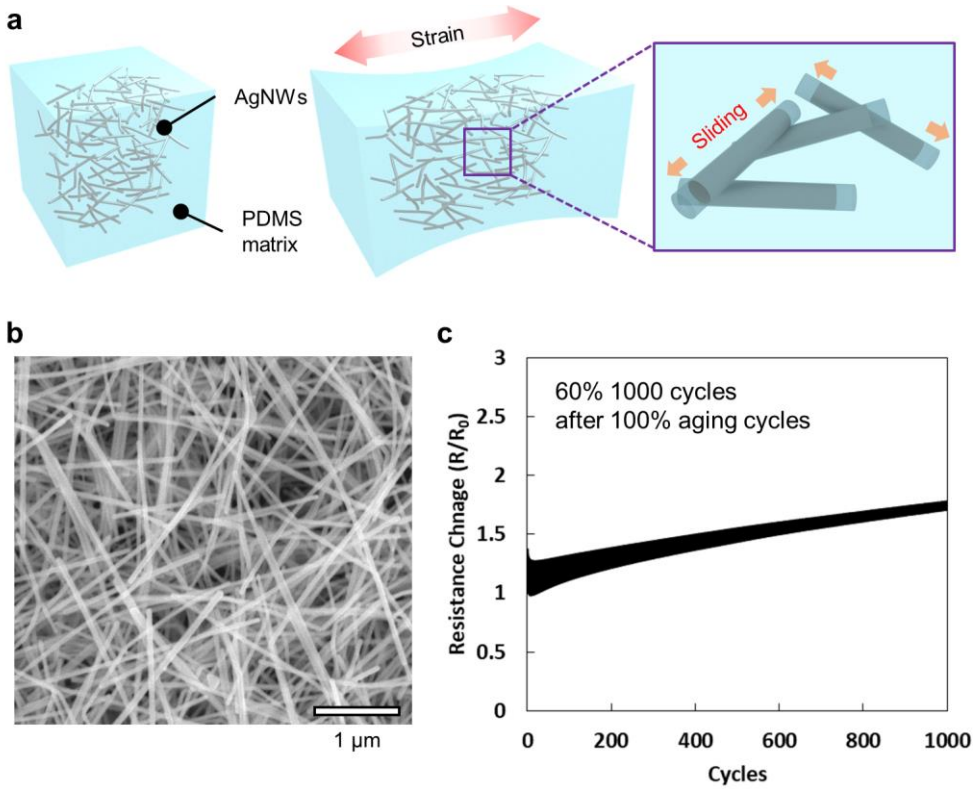

Figure 4.14 | Mechanical reliability of AgNW electrodes. a, Mechanism of the stretchable electrodes. **b**, SEM image of the AgNW random network. **c**, Resistance change of the electrodes during 50% stretching cycles.

4.3.6 Optimization of Magnetic Self-Assembly Process

The formation of reliable and reproducible STCs *via* the magnetic self-assembly process is of great importance for integration into practical large-area TEGs and mass production. In this regard, the process parameters such as magnetic flux intensity and PDMS viscosity that could seriously affect the heat transfer ability and softness of the STCs. Therefore, they were fairly optimized to be placed in a central region in the process window, so they cannot significantly change the mechanical properties of the STCs. As a result, the process can be facilely reproduced by the readers in this field. Thermal conductivity of the STCs was systematically investigated while changing the magnetic flux intensity and PDMS precursor viscosity to demonstrate the stability and reliability of the magnetic self-assembly process.

Magnetic flux intensity. The magnetic field intensity directly affects the degree of the convergence and alignment of the magnetic particles. Therefore, the through-plane thermal conductivity of the STCs was investigated while changing the magnetic flux intensities during STC formation. Figure 4.15a presents the top-view optical images of the STC patterns fabricated using magnets with 600 G, 1000 G, and 1600 G, respectively. The clear patterns were defined for all of the three cases without perceptible differences in shapes and sizes. Furthermore, the thermal conductivities of the STCs did not show noticeable dependency with magnetic flux intensities, as shown in Figure 4.15b, which indicates the magnetic flux intensity > 600 G is enough to saturate the vertically aligned magnetic particles, *i.e.* percolation paths.

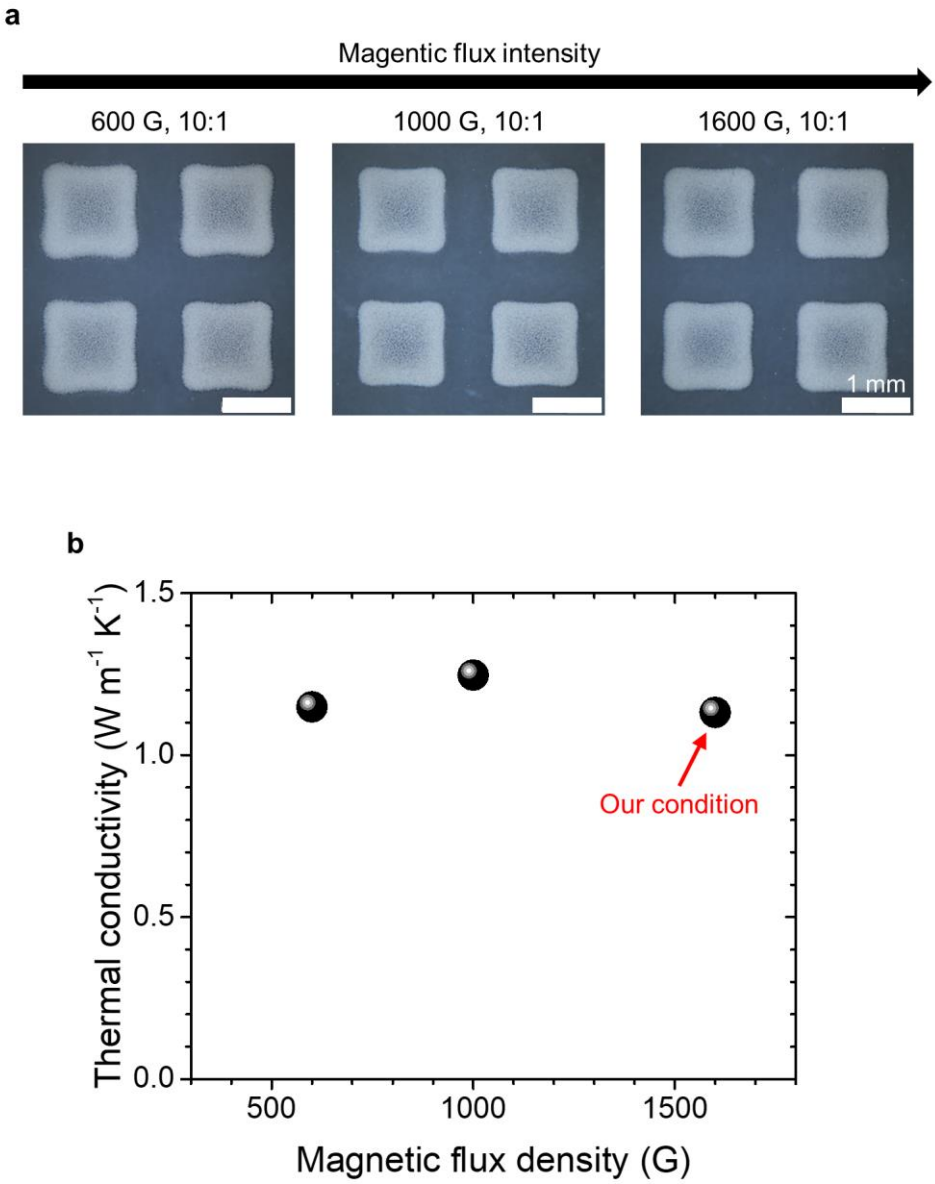

Figure 4.15 | STCs fabricated under different magnetic flux intensities. **a**, Top-view optical images of the STCs patterned using magnets with 600 G, 1000 G, and 1600 G. **b**, Thermal conductivities of the STCs as a function of magnetic flux density.

PDMS precursor viscosity. In the magnetic alignment of Ag-Ni MPs, the viscosity of the Ag-Ni MPs/PDMS mixture determined by the ratio of PDMS base and curing agent is of great importance. For further investigation, STCs were fabricated using mixtures of PDMS and curing agent with 10:1, 20:1, and 30:1 in weight ratio. The corresponding viscosities were 2.4 Pa s, 3.4 Pa s, and 3.8 Pa s, respectively. The top-view optical images in Figure 4.16a shows that all of the STC patterns in the PDMS platform with different mixing ratios are almost identical. Although the through-plane thermal conductivity slightly decreased for the case of the 30:1 PDMS, the STCs with 10:1 and 20:1 PDMS exhibit similar thermal conductivities. (Figure 4.16b). These results support that the magnetic patterning/alignment process is highly reliable without the significant dependency of the viscosity of PDMS mixture maintaining the improved heat transfer ability.

In summary, the key process parameters, such as magnetic field intensity and PDMS precursor viscosity, were placed in the middle of the process window, so allowing the process to be more stable under ambient conditions. They obviously could affect the thermal conductivity of the STCs under specifically extreme conditions such as very low magnetic field intensity or high viscosity. However, from the careful optimization, the experimental conditions, including a magnetic flux intensity of ~1600 G and a PDMS mixing ratio of 10:1, are enough to realize the high-quality, reliable, and reproducible STCs.

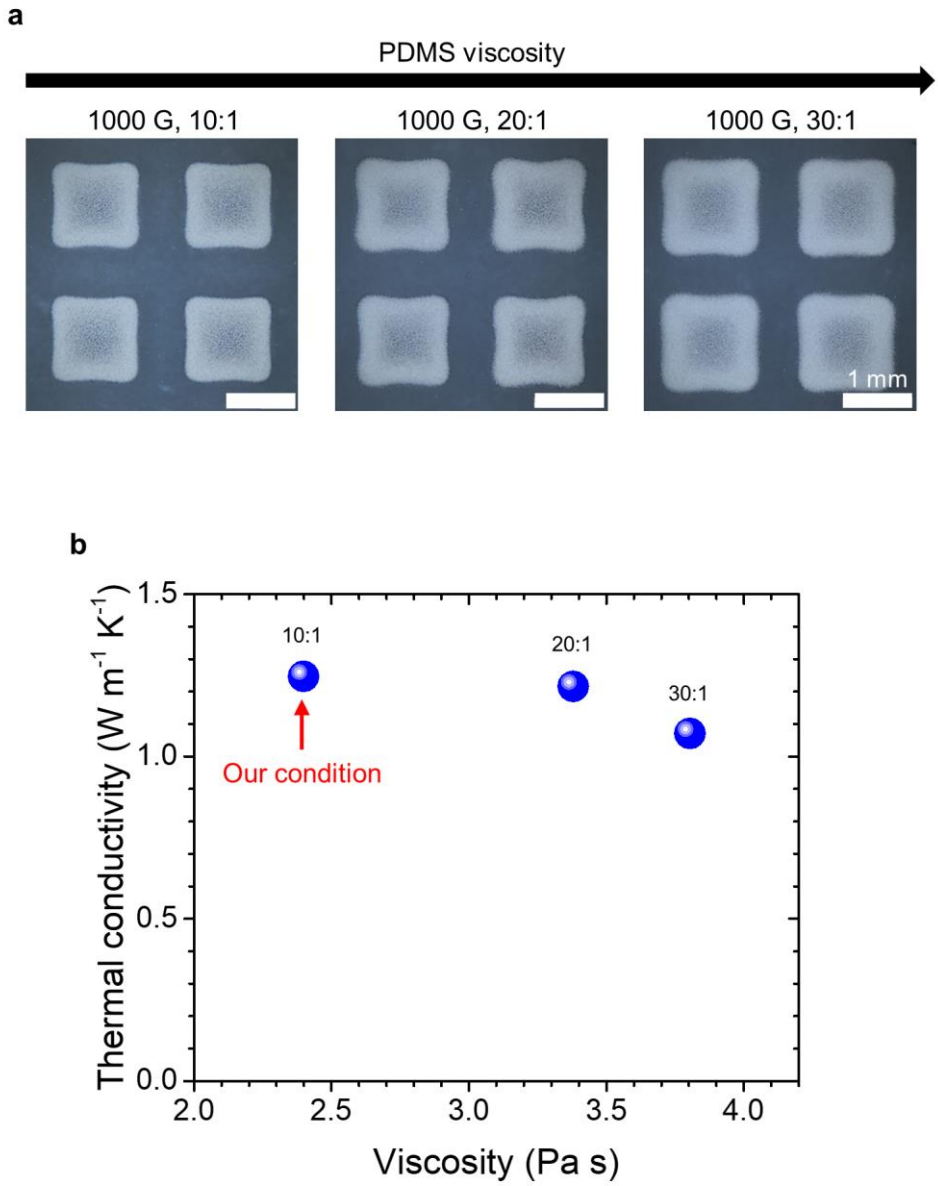

Figure 4.16 | STCs fabricated with different PDMS viscosities. a, Top-view optical images of the STC patterns with a PDMS mixing ratio of 10:1, 20:1, and 30:1. **b**, Thermal conductivities of the STCs as a function of viscosity of the PDMS precursor mixture.

4.4 Conclusion

In summary, this chapter introduced the intrinsically soft interconnection platforms with an efficient heat transfer strategy for high-performance compliant TEGs. The proposed SHEP comprises STCs and stretchable electrodes in an elastomeric matrix. The STC features magnetically self-assembled chains of ferromagnetic particles, which significantly improve the heat transfer ability of the elastomer without compromising its softness, exhibiting a thermal conductivity of ~1.4 W m^{-1} K^{-1} and Young's modulus of < 10 MPa. The AgNW random networks are embedded in the elastomeric matrix, forming intrinsically stretchable interconnections for TE legs. They can maintain their electrical conductivity under a tensile strain without affecting the softness of the soft platform.

Furthermore, the fabrication process of the SHEP shows a number of advantages. In the SHEP formation process, the AgNW networks were embedded, and Ag-Ni MPs were self-assembled in the PDMS matrix, simultaneously, during a single curing process. This unique process is not only facile and customizable but also highly reliable and reproducible with the optimized process windows.

The proposed intrinsically soft platforms could play an important role in realizing highly conformable TEGs for high-efficiency thermal harvesting on 3D surfaces. In the next chapter, mechanically compliant TEGs using SHEPs will be introduced. The enhancement of the heat transfer from 3D heat sources to TE legs due to the improved conformability *via* SHEPs will be intensively investigated. In addition, interesting and practical wearable applications using highly conformable TEGs will be demonstrated.

Chapter 5

Highly Conformable Thermoelectric Generators with Enhanced Heat Transfer Ability

5.1 Introduction

Although recent efforts to improve TE performance of organic materials are promising [93], flexible or soft TEGs based on organic TE materials are still in their infancy due to their much lower performance compared to inorganic TE materials. Therefore, to improve mechanical conformability and heat transfer ability of inorganic-material-based TEGs is the most realistic option for practical wearable applications. This chapter introduces a highly conformable TEG where high-performance inorganic TE legs are integrated with the SHEPs (compliant TEG for short). Figure 5.1 illustrates the design and fabrication scheme of the compliant TEG. As shown in the cross-sectional images of the fabricated TEG in Figure 5.1, the 2-mm-high Bi_2Te_3-based TE legs are sandwiched by the STCs and interconnected by the AgNW-based stretchable electrodes. The dimensions and materials are chosen for a sufficient temperature gradient and high TE performance. Notably, the

integration process is fully automated, enabling fast and reliable implementation of large-area and high-fill-factor TEGs. Due to the AgNW-based soft electrodes in the SHEP, the fabricated compliant TEG shows stretchability up to 20% and conforms perfectly to curved surfaces without air gaps that cause significant heat loss. Furthermore, the STCs in the SHEP efficiently transfer heat from 3D heat sources to the TE legs. In the following sections, the methodologies, mechanical characteristics, and TE performance of the proposed compliant TEGs are described in detail. In particular, the enhanced TE performance due to the STCs is systematically investigated. Furthermore, the enhanced heat transfer from 3D heat sources to TE legs *via* improved conformability is demonstrated by a series of FEAs and experiments. Finally, self-powered wearable systems indicating an abrupt temperature increase is demonstrated to show the feasibility of the proposed concept in practical applications.

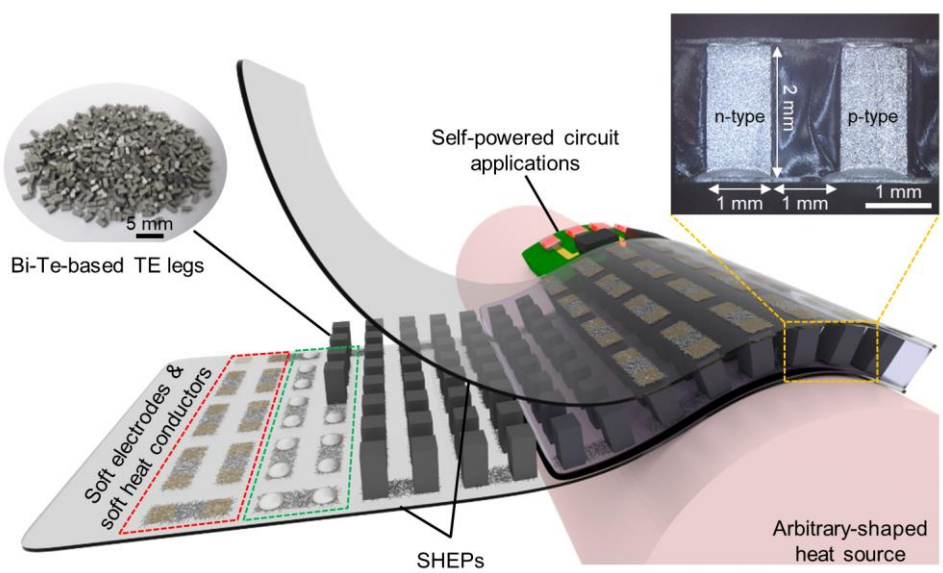

Figure 5.1 | Conceptual illustration of the compliant TEGs with SHEPs.

5.2 Experimental Section

5.2.1 Fabrication of Compliant TEGs

The integration of Bi_2Te_3-based TE legs and the prepared SHEPs was performed using fully automated machines. The dimensions of the TE leg were 1 mm × 1 mm × 2 mm. Figure 5.2 shows detailed procedures for the integration process. Conductive epoxy was automatically printed onto the STC patterns in the top and bottom SHEPs using a programmable pneumatic dispenser (SHOTmini 200Sx, Musashi Eng.) controlled by a 3-axis motorized robot. It should be noted that the amount of the conductive epoxy for each bonding was perfectly optimized to deliver low contact resistance between TE legs and AgNW electrodes and achieve good adhesion by controlling dispensing conditions such as pneumatic pressure and time. In most cases, the dispensing of the epoxy was performed with 400 kPa for 2 s using a 32G needle. Then, the Bi_2Te_3 legs were sequentially placed by a programmable pick-and-place machine (TM220A, NeoDen) on the printed epoxy. The top SHEP with printed epoxy was aligned and attached to the top of the Bi_2Te_3 legs using a home-made aligning apparatus. The printed epoxy was cured at 170 °C for 1 h in an oven. For the realization of mechanically reliable and conformable TEGs, PDMS was infiltrated between the top and bottom SHEPs, followed by annealing at 100 °C for 1 h on a hot plate. Finally, compliant TEGs with STCs and intrinsically stretchable electrodes were obtained after the supporting glasses were detached from the TEGs. For a TE characterization purpose, 36 np-pair TEGs were fabricated. For wearable applications, TEGs comprising 440 TE legs (220 np pairs) were fabricated.

This integration procedure was highly automated except only the PDMS infiltration and glass detachment. This highly automated process enables the rapid and reliable implementation of large-area compliant TEGs, even comprising 440 TE legs, which has been impossible with previous manual integration processes. It should be noted that the compliant TEG with 440 TE legs has the largest number of TE legs in the state-of-the-art flexible and stretchable TEGs.

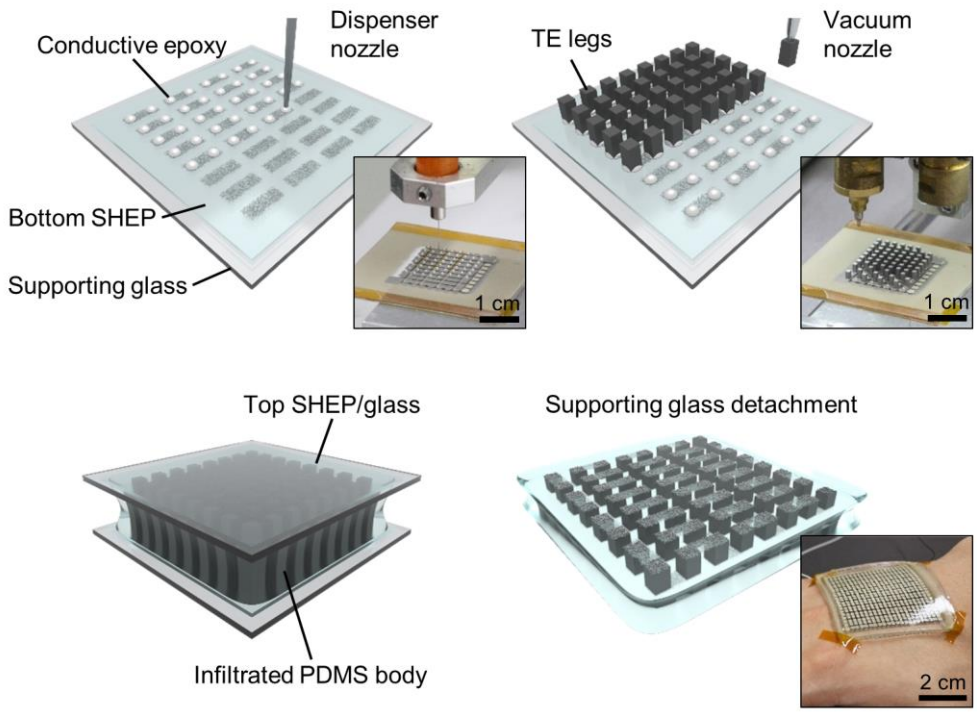

Figure 5.2 | Integration process of the TE legs and prepared SHEPs.

5.2.2 Measurements

Seebeck coefficient of a single TE leg. The Seebeck coefficients of *p*- and *n*-type Bi_2Te_3 legs were calculated from the Seebeck voltages of each leg under different temperature differences. Figure 5.3 illustrates the experimental setup for measuring the Seebeck coefficient of each leg. Thin aluminum (Al) films (16 μm thick) were used as electrodes. Because the thermal conductivity of the Al film (> 200 W m^{-1} K^{-1}) is much higher than that of the TE leg, and the Al film is much thinner than the leg (2 mm height), the vertical temperature drop across Al film is negligible, and the laterally uniform temperature was ensured at each end of the leg. Two Peltier devices were used to apply a stable temperature difference across the leg. The real-time temperature difference was monitored by two thermometers with thermocouples placed between thermal pads and the Al electrodes. The Seebeck voltage was measured by a voltage meter. Figure 5.4 plots the

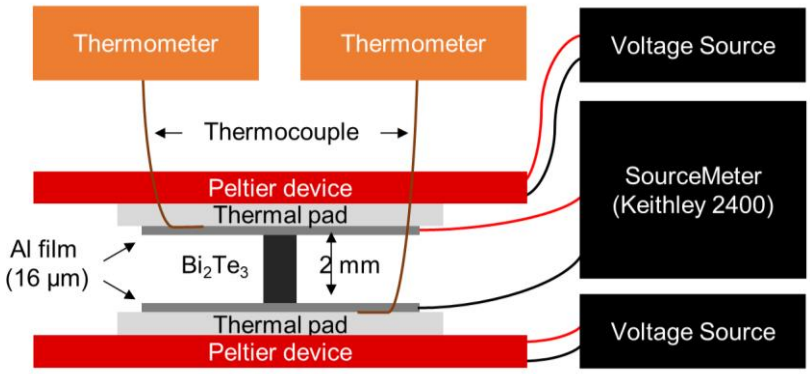

Figure 5.3 | Experimental setup for measuring Seebeck coefficient of a single TE leg.

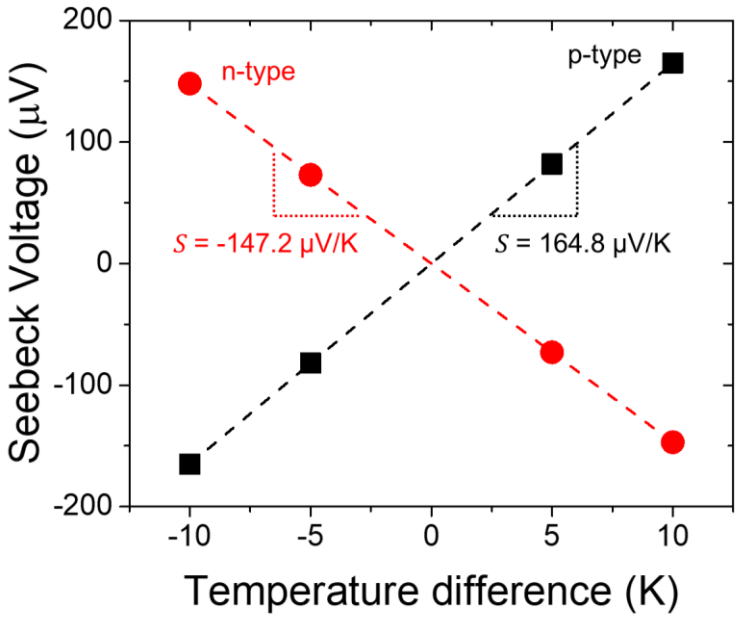

Figure 5.4 | Seebeck voltage as a function of temperature difference to extract Seebeck coefficients of *p*- and *n*-type Bi_2Te_3 TE legs.

measured Seebeck voltage for *p*- and *n*-type Bi_2Te_3 legs. The Seebeck coefficients calculated from these values were 164.8 μV K^{-1} and -147.2 μV K^{-1}, respectively. All simulations and calculations that required the Seebeck coefficient of each leg were performed using these values.

TE characterization of the compliant TEGs. Figure 5.5 illustrates the experimental setup for TE characterization of the compliant TEGs. Peltier devices and air coolers were used for heating and cooling, respectively, to ensure a controlled temperature difference between the Bi_2Te_3 TE legs. The compliant TEGs were sandwiched between the heated and cooled metal plates to measure their TE characteristics. During the measurement, nonconductive thermal pads were attached to the top and bottom of the TEGs to prevent

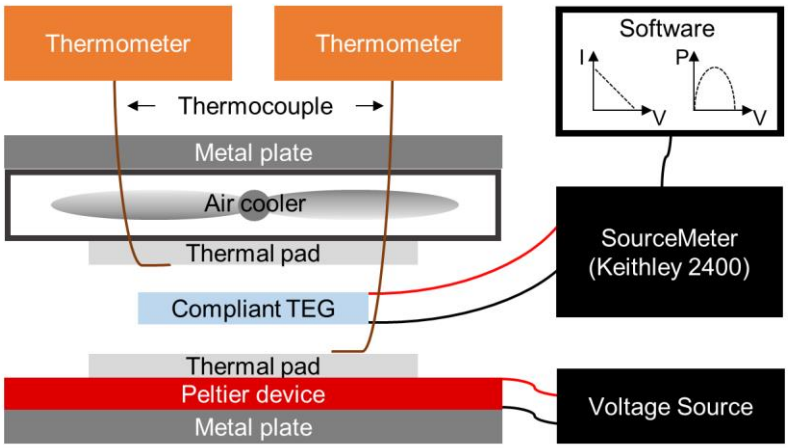

Figure 5.5 | Experimental setup for TE characterization.

electrical shorting among adjacent STCs. The temperature difference between the hot and cool zones was monitored by a thermometer with a thermocouple wire placed between the thermal pad and the TEGs. After the thermal equilibrium state was reached, the output voltage and current were measured by SourceMeter (Keithley 2400).

Mechanical reliability of the compliant TEGs. The resistance and TE performance of the compliant TEG were measured during and after different bending and stretching conditions to investigate the mechanical reliability of the compliant TEG. Cyclic bending and stretching tests were conducted using homemade 1D stretching equipment. A bending radius was 15 mm, and the moving speed was 100mm/min for the bending test. A strain of 10% was applied with a stretching speed of 20mm/min for the stretching test. During the cycle tests, the resistance was monitored in real time by SourceMeter.

5.2.3 Finite Element Analysis

The Heat Transfer in Solids, Electric Currents, and Solid Mechanics modules in COMSOL Multiphysics (COMSOL Inc.) were used to estimate the TE and mechanical performances of the compliant TEG. The thermal conductivity of the STC and Seebeck coefficients of the TE legs were set from the experimentally measured data. Except for those stated above, the properties of materials were taken from the datasheet or default values in COMSOL. Table 5.1 summarizes the parameters for the FEA. The dimensions of all compliant TEGs for modeling were the same as those of the real device. Figure 5.6 shows the details of the 3D models for the FEA.

Table 5.1 | Parameters for the FEA.

Parameter / Material	Seebeck coefficient ($\mu V\ K^{-1}$)	Electrical conductivity ($S\ m^{-1}$)	Thermal conductivity ($W\ m^{-1}\ K^{-1}$)
s-HC	-	-	1.4
p-Bi_2Te_3	147.2	6.11×10^4	1.9
n-Bi_2Te_3	-164.8	3.41×10^4	1.9
AgNW	-	10^6	1.0
PDMS	-	2.5×10^{-14}	0.16

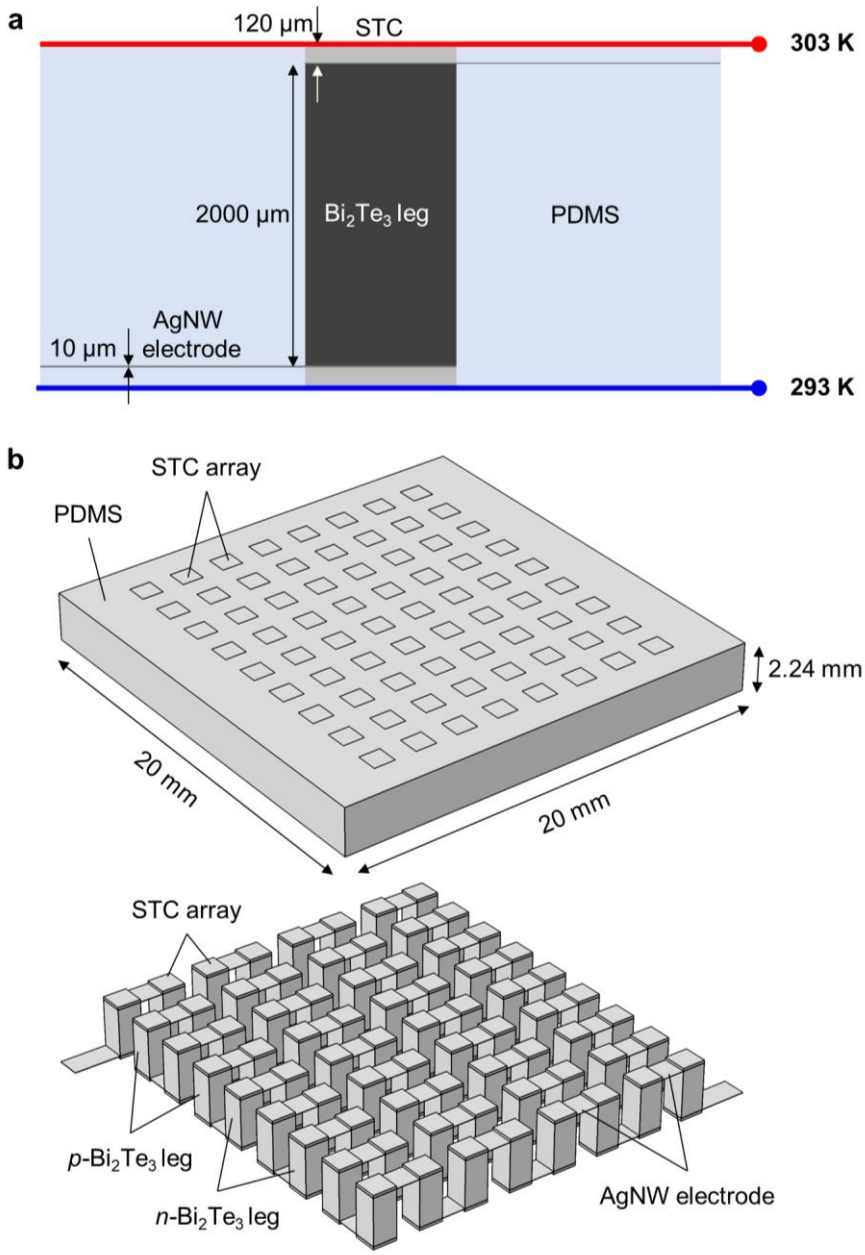

Figure 5.6 | Details of 3D models for the FEA. a, Cross-sectional view of the FEA model. **b**, 3D view of the FEA model.

5.3 Results and Discussion

5.3.1 Enhancement of TE Performance *via* STCs

The performances of 36-np-pair TEGs with and without STCs were compared by both 3D FEA and experimental measurements to investigate the effect of the STCs in the SHEP on the power generation. Figure 5.7a and b present the FEA results showing the temperature distribution on a cross-section of the two TEGs when the $\Delta T_{\mathrm{Applied}}$ between the top and bottom boundaries was 10 K. In the case of the TEG without STCs, although the PDMS supporting layers were sufficiently thin (120 μm) compared to the height of the TE leg, the ΔT_{TE} was only 5.1 K. The main reason for this small difference is that the thermal conductivity of PDMS (~0.16 W m^{-1} K^{-1}) is extremely low compared to that of the TE leg; therefore, a large portion of $\Delta T_{\mathrm{Applied}}$ was lost across the PDMS layers. In contrast, the temperature was linearly distributed across the TEG with STCs, showing a ΔT_{TE} of 8.6 K. It is because the improved thermal conductivity of the STC was comparable to that of the TE leg. Figure 5.7c and d present the electric potential generated by each device calculated from the FEA. The resulting V_{OC} values were 61.7 mV and 96.5 mV for the TEGs without and with STCs, respectively. Figure 5.8 plots the V_{OC} values calculated by the FEA as a function of the thermal conductivity of the STC. The graph shows that the STC enables ~86% of the maximum V_{OC} for the 36-np-pair TE legs. The maximum V_{OC} is the value when the $\Delta T_{\mathrm{Applied}}$ of 10 K is totally applied to the TE leg.

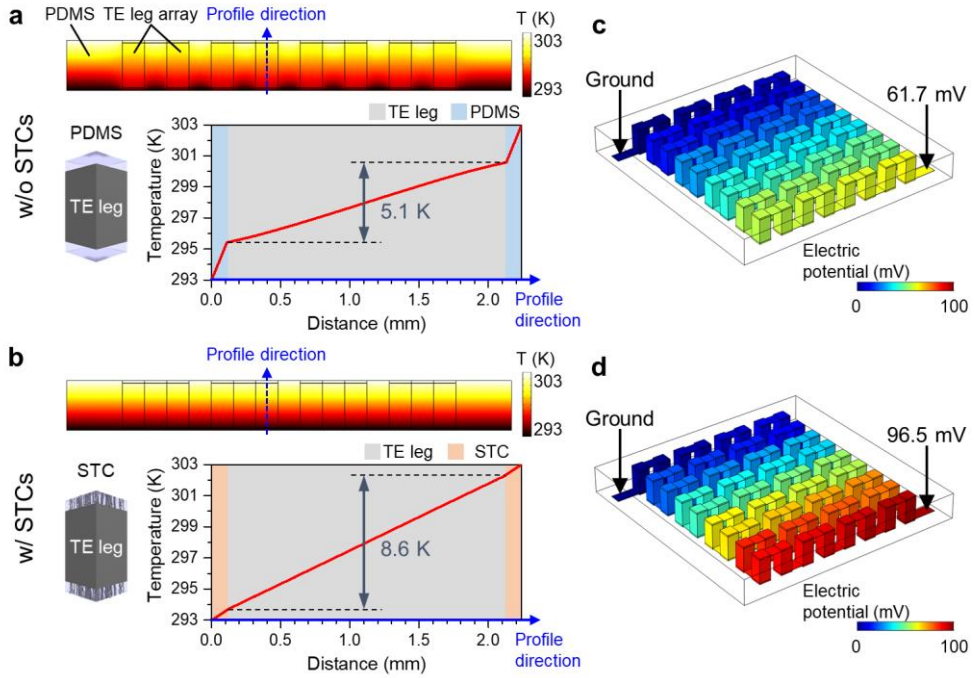

Figure 5.7 | Effect of the STCs on TE performance. a and **b**, FEA results showing the temperature distribution on the cross-section of the TEGs without (**a**) and with STCs (**b**) for a given temperature difference of 10 K. **c** and **d**, FEA results showing the V_{OC} of the 36-np-pair TEGs without (**c**) and with STCs (**d**) for a given temperature difference of 10 K.

The experimental results also verified the effect of the STCs on the TE performance of the TEGs. Two 36-np-pair compliant TEGs without and with STCs were fabricated for comparison. In other words, the compliant TEG using SHEPs and the reference TEG comprising only stretchable electrodes without STC were fabricated. The performance of the two TEGs was measured using homemade measurement equipment while changing the $\Delta T_{\mathrm{Applied}}$, as explained in Experimental Section and Figure 5.5. Figure 5.9a and b show the current and power of the two TEGs as a function of voltage.

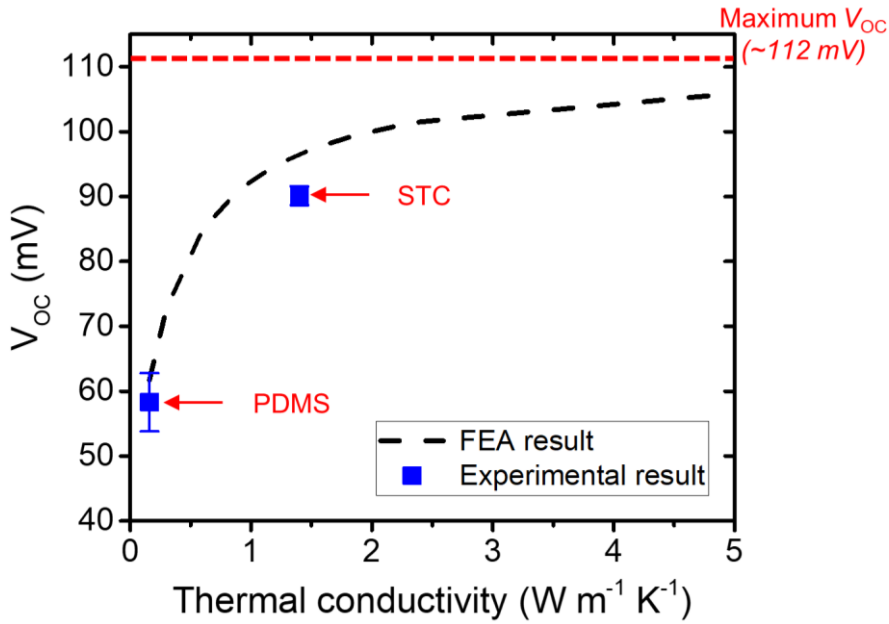

Figure 5.8 | V_{OC} of a 36-np-pair TEG as a function of thermal conductivity of the STC.

Both TEGs showed linear and quadratic increases in V_{OC} and output power, respectively, as $\Delta T_{\mathrm{Applied}}$ increased. The TEG with STCs showed 45% higher V_{OC} compared to that without STCs, 61.4 mV versus 89.5 mV at a $\Delta T_{\mathrm{Applied}}$ of 10 K, which is consistent with the FEA results. The maximum powers of the TEGs without and with STCs at a $\Delta T_{\mathrm{Applied}}$ of 40 K were 232 μW and 828 μW, respectively. These experimental results highlight that the STC significantly improves the TE performance of the elastomer-based compliant TEGs. Although the V_{OC} can be further improved by increasing the thermal conductivity of the STC or decreasing the thickness of the STC, the parameters were optimized with regard to softness, mechanical reliability, and process stability. Furthermore, the enhanced heat transfer ability of the

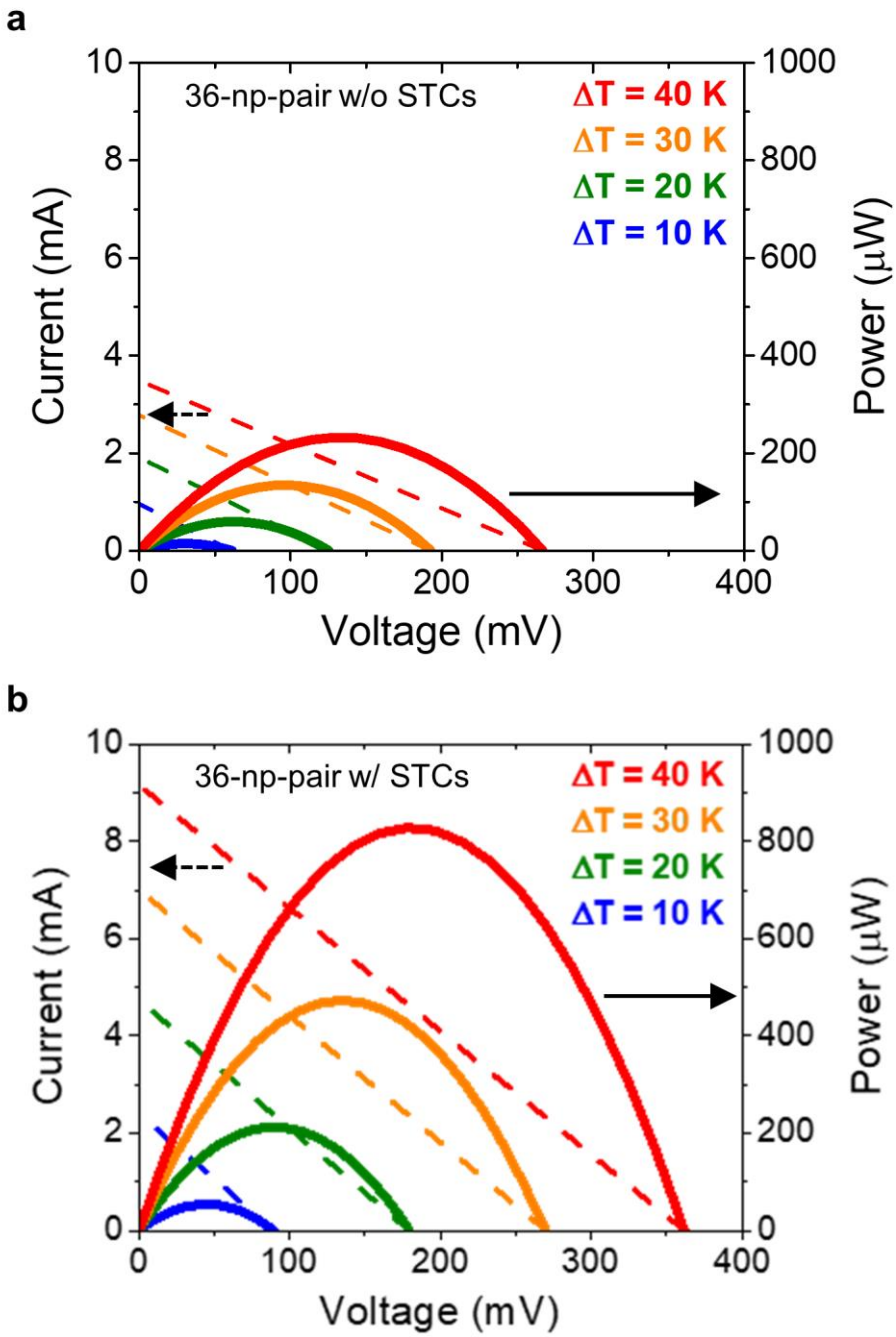

Figure 5.9 | a and **b**, Experimentally measured TE performances of 36-np-pair TEGs without (**a**) and with STCs (**b**) showing current and power as a function of voltage.

compliant TEG allows a fast response to a dynamic temperature change. The V_{OC} of the two TEGs was measured when an aluminum cup with hot water (~70 °C) was abruptly placed in contact with their top surfaces. The schematic illustration and optical image in Figure 5.10a show the experimental setup. Figure 5.10b plots the time-resolved V_{OC} of the two TEGs (black and red dots). The TEG with STCs responded to the temperature change faster than

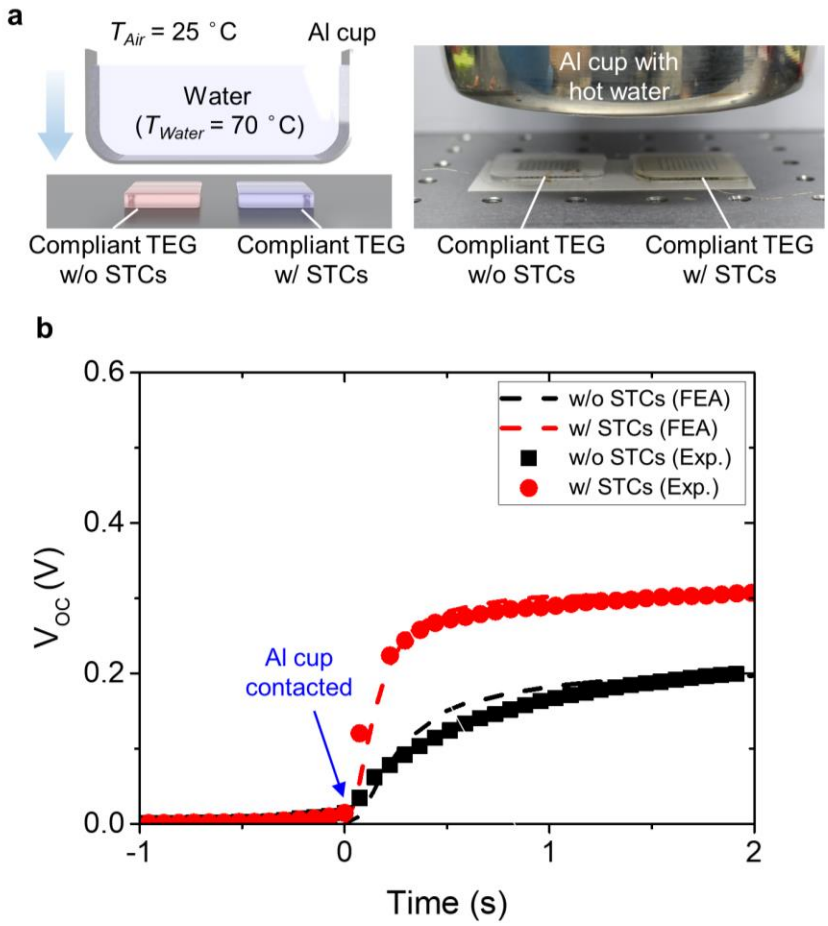

Figure 5.10 | Dynamic response of the TEGs without and with STCs. a, Experimental setup. **b**, Time-resolved V_{OC} of the TEGs without and with STCs when an aluminum cup with hot water is abruptly placed on the two TEGs. The dashed lines represent the corresponding FEA results.

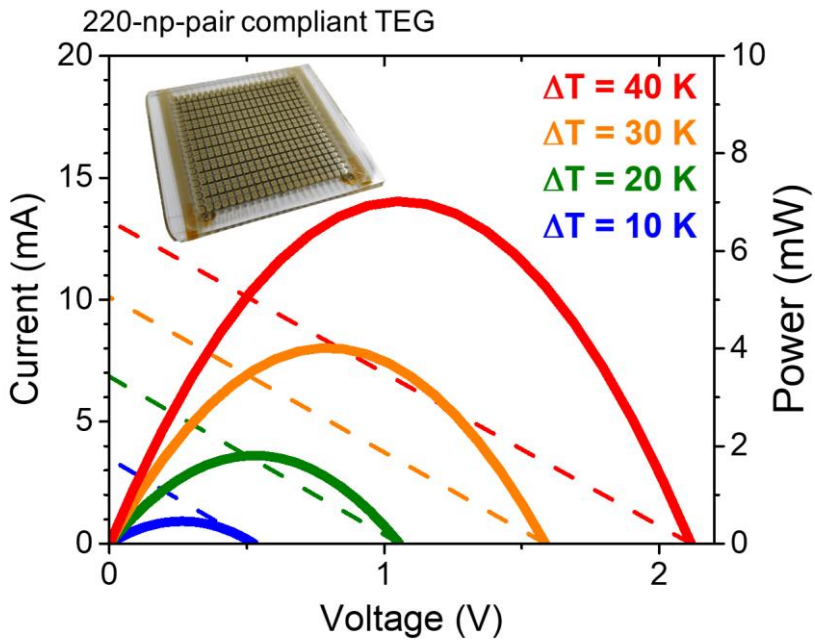

Figure 5.11 | Experimentally measured TE performance of a 220-np-pair compliant TEG showing current and power as a function of voltage. The inset photograph shows the large-area compliant TEG.

the TEG without STCs, with a higher saturation V_{OC}. The dashed lines are the FEA results, which show good agreement with the experimental results.

One of the long-term demands in wearable TEG applications is the reliable operation of high-fill-factor compliant TEGs. A compliant TEG with 440 TE legs was successfully reliably fabricated in an area of 3.9 × 4.3 cm^2 using the proposed scalable and automated fabrication method. Figure 5.11 shows the performance of the 220-np-pair TEG. The TEG generated a maximum power of 7.02 mW and a V_{OC} of 2.12 V at a $\Delta T_{\mathrm{Applied}}$ of 40 K. Figure 5.12 and Table 5.2 summarize the performance of the state-of-the-art flexible/wearable TEGs [28,64-73,94]. The fabricated 220-np-pair compliant

TEG with STCs shows the highest normalized Seebeck voltage per unit area, the V_{OC} normalized by the ΔT and the dimension of TEGs. It is due to the outstanding heat transfer ability of the STCs and the high fill factor achieved by the automated integration process. Furthermore, it shows the highest normalized power density, the power density divided by ΔT^2 to exclude the ΔT dependency, in the stretchable TEG group. The value of 0.26 μW cm^{-2} K^{-2} is even comparable to the top records of previous flexible TEGs with the rigid Cu electrodes, although some of them show higher values > 1 μW cm^{-2} K^{-2} owing to the high conductivity of the rigid Cu electrodes. But the rigid electrodes severely compromise the conformability of TEGs, which will be further investigated in the following sections.

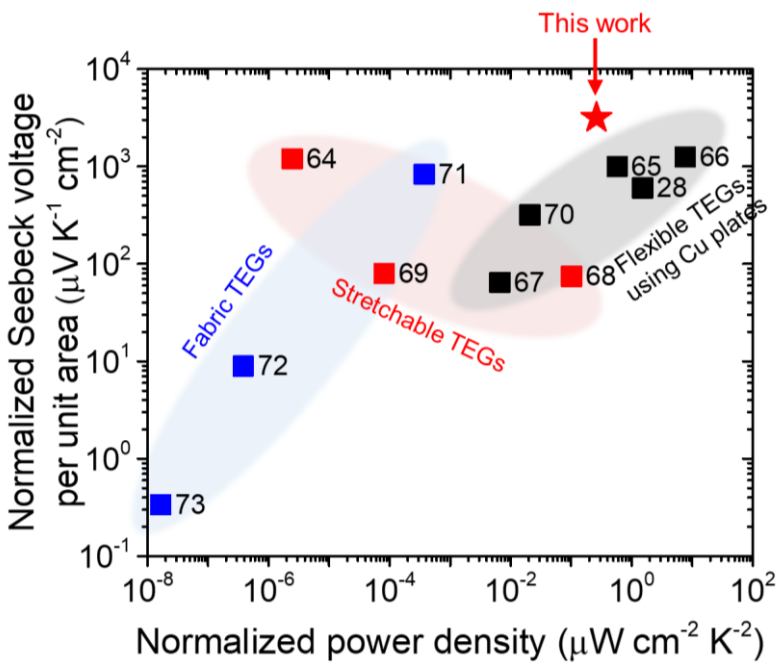

Figure 5.12 | Performance summary of wearable TEGs [28,64-73,94].

Table 5.2 | Summary of wearable TEGs [28,64-73,94].

Ref.	Strategy	Interfacing substrate (thermal conductivity, W m^{-1} K^{-1})	Legs	Area (cm^2)	ΔT (K)	V_{OC} (mV)	Normalized Seebeck voltage per unit area (μV K^{-1} cm^{-2})	Normalized power density (μW cm^{-2} K^{-2})	Flexibility	Stretchability
This works	Bi_2Te_3-based TE leg /AgNW electrodes	s-HC (1.4)	72	2.55	40	362	3549	0.203		20%
This works	Bi_2Te_3-based TE leg /AgNW electrodes	s-HC (1.4)	440	16.77	40	2116	3154	0.262		20%
[68]	BiTe-based TE leg /LM electrodes	Silicone composite (0.28)	8	2.02	20	3	74.4	0.1		20%
[64]	silicone coils	PDMS (0.16)	128	2.25	19	51.3	1200	2.5E-06		60%
[69]	Transition metal dichalcogenide nanosheets	PDMS (0.16)	32	10	3	2.4	80	8.1E-05		50%
[28]	BiTe-based TE film /Cu electrodes	PDMS (0.16)	8	3	50	90	600	**1.52**	20 mm	
[66]	BiTe-based TE leg /Cu electrodes	PDMS (0.16)	144	16	25	500	1250	**7.648**	5 mm	
[70]	BiTe-based TE leg /Cu electrodes	PI film	36	12.6	12	48	317.5	0.02083	NA	
[67]	BiTe-based TE leg /Cu electrodes	PDMS (0.16)	104	11.5	50	37.2	64.5	0.00668	15 mm	
[65]	BiTe-based TE leg /Cu electrodes	Ecoflex/AlN (0.77)	144	25	6.6	165	1000	**0.576**	20 mm	
[94]	BiTe-based TE film /PEDOT:PSS hybrid composites	PI film	14	NA	50	85.2	NA	**0.48**	15 mm	
[71]	BiTE-based TE film /polymer fabric	fabric	24	1.5	20	25	833.3	0.00037	NA	
[72]	Nanomaterial/fabric/silver foil electrodes	fabric	24	32	35	10	8.93	3.8E-07	NA	
[73]	PEDOT:PSS/MWCNT-based yarns	fabric	20	36	66	0.8	0.337	1.66E-08	NA	

The limitations of previously reported approaches are highlighted in red.

5.3.2 Mechanical Reliability of Compliant TEGs

The compliant TEGs showed high deformability and mechanical reliability under tensile strain compared to those reported in the previous literature because the intrinsically stretchable AgNW electrodes with a low Young's modulus effectively absorb the applied stress, and the infiltrated PDMS acts as a buffer preventing each leg from being ruptured by extreme deformation. For a systematic analysis, a FEA was carried out on the stress and strain distribution at an interconnection surface when the compliant TEG (c-TEG) with AgNW-based soft electrodes and a reference TEG (r-TEG) with Cu electrodes were mechanically bent and stretched. Figure 5.13 presents the FEA result on the bent TEGs. When they were bent, extremely high stress occurred across the Cu electrodes compared to that across the AgNW

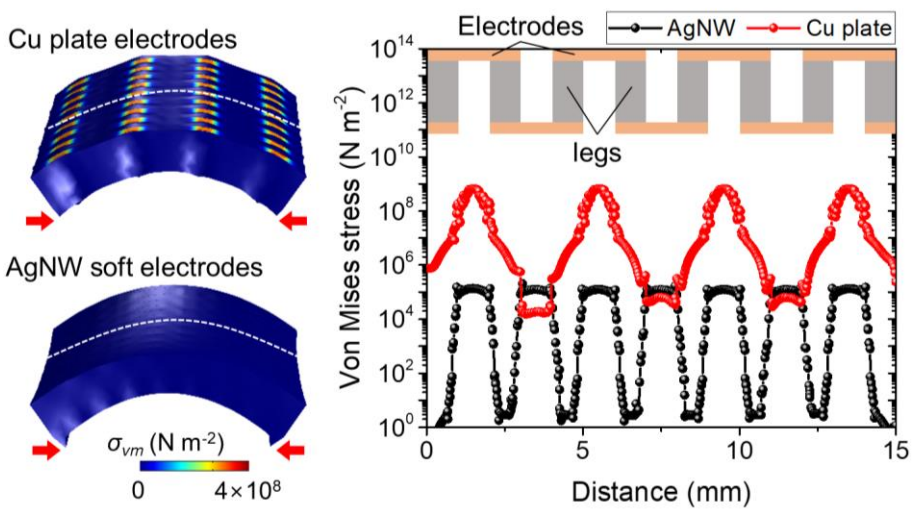

Figure 5.13 | FEA results showing the von Mises stress of the surfaces of a TEG with Cu plate electrodes and a TEG with AgNW-based soft electrodes under bending conditions.

electrodes due to the high Young's modulus of the Cu plates (~120 GPa). This excessive stress results in high flexural rigidity and limited deformability. In contrast, because the Young's modulus of the AgNW electrodes is almost the same as that of the PDMS, the stress across the AgNW electrodes is as low as that across the PDMS matrix. This results in low flexural rigidity and high conformability of the compliant TEG. Furthermore, the c-TEG showed smooth bending surfaces, unlike the rugged ones of the r-TEG.

Figure 5.14 is the FEA result under a stretching condition. When a tensile strain of 20% was applied, the FEA results showed a concentrated strain > 250% at the interfaces between the PDMS and the Cu plates, which far exceeds the fracture strain of PDMS. This concentrated strain could rupture the device and impede reliable operation under the stretching condition. On the other hand, the AgNW electrodes effectively absorbed the

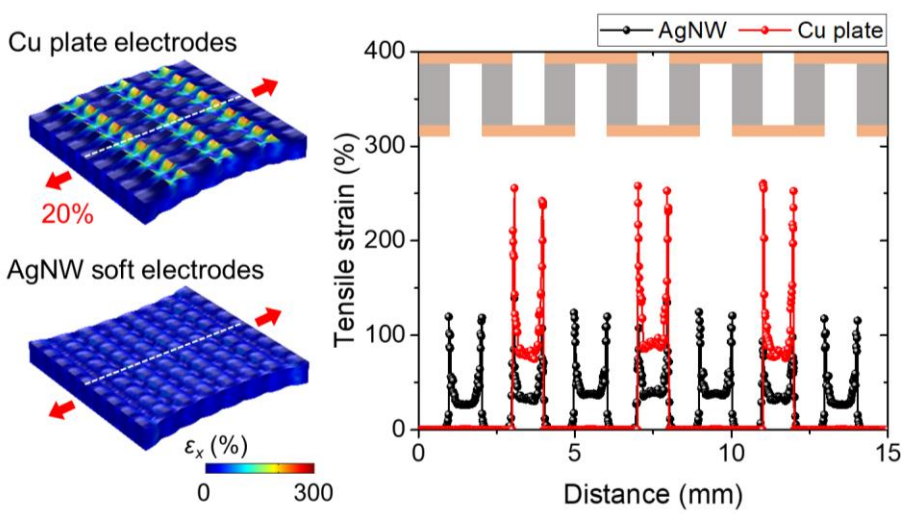

Figure 5.14 | FEA results showing the principal strain of the surfaces of a TEG with Cu plate electrodes and a TEG with AgNW-based soft electrodes under a uniaxial strain of 20%.

strain energy and maintained a maximum strain < 150%, which lowers the possibility of the device rupture.

The mechanical reliability of the compliant TEG was experimentally demonstrated by measuring the resistance change (ΔR) to the initial resistance (R_0) and TE performance under different bending and stretching conditions. Figure 5.15a shows the resistance change of the TEG when it is bent with different bending radii. The $\frac{\Delta R}{R_0}$ of the TEG remained < 50% even when the bending radius reached ~11 mm. Figure 5.15b shows the $\frac{\Delta R}{R_0}$ of the TEG while it is bent repeatedly with a bending radius of 15 mm. The resistance of the TEG was stable over 1000 bending cycles. The TE performance of the TEG was repeatedly measured after 1st, 10th, 100th, 1000th, and 10000th bending cycles along both x-axis and y-axis, to check the degradation of the

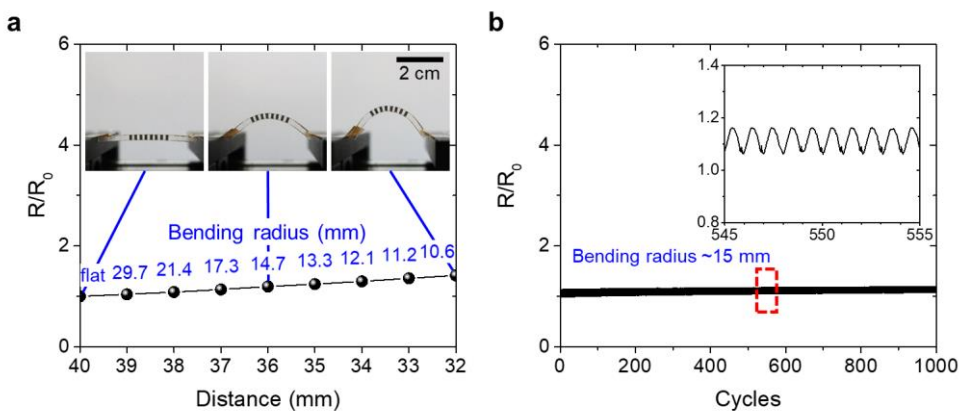

Figure 5.15 | Resistance change of the compliant TEG under bending conditions. a, Resistance change as a function of a bending radius. The inset photographs show side views of the bent TEG for different bending radii. **b**, Resistance change of the compliant TEG under cyclic bending with a bending radius of ~15 mm. The inset shows an enlarged view of the recorded data.

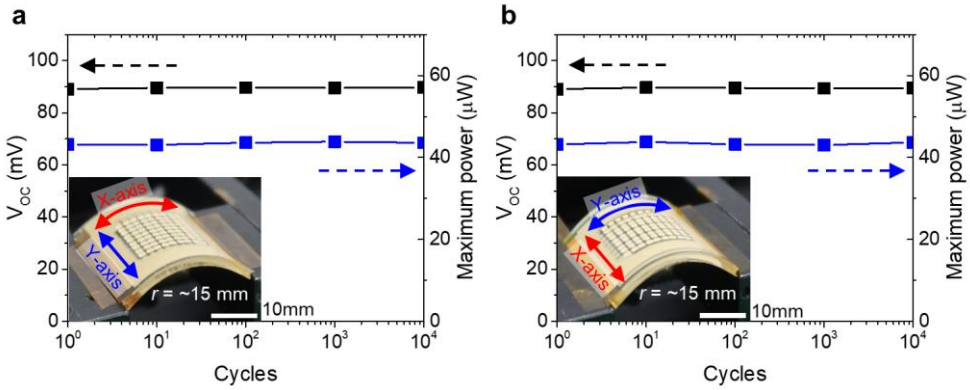

Figure 5.16 | TE performance after cyclic bending. a and **b**, TE performance of 36-np-pair compliant TEG measured after different bending cycles with different bending directions of x-axis (**a**) and y-axis (**b**).

performance after the bending stress. As shown in Figure 5.16, the V_{OC} and power at a $\Delta T_{\mathrm{Applied}}$ of 10 K were maintained without degradation even after 10000 bending cycles along both x-axis and y-axis.

The stretchability of the compliant TEG and the performance change under the stretching conditions were also investigated. Figure 5.17a shows the resistance change of the TEG when it is continuously stretched. The compliant TEG maintained its conduction up to the tensile strain of 20% with a $\frac{\Delta R}{R_0}$ of 160%. Figure 5.17b shows the resistance change of the TEG under the cyclic stretching condition with a strain of 10%. It showed great cyclic reliability. Figure 5.17c plots the V_{OC} generated by the compliant TEG when it is strained at a $\Delta T_{\mathrm{Applied}}$ of 10 K. It is noted that while flexible TEGs exploiting nanostructured or thin-film TE materials suffer from the strain effect on the Seebeck coefficient [95,96], the V_{OC} of the compliant TEG with

SHEPs did not change under the applied strain because the Bi_2Te_3 legs in the compliant TEG are strain-free (see Figure 5.14).

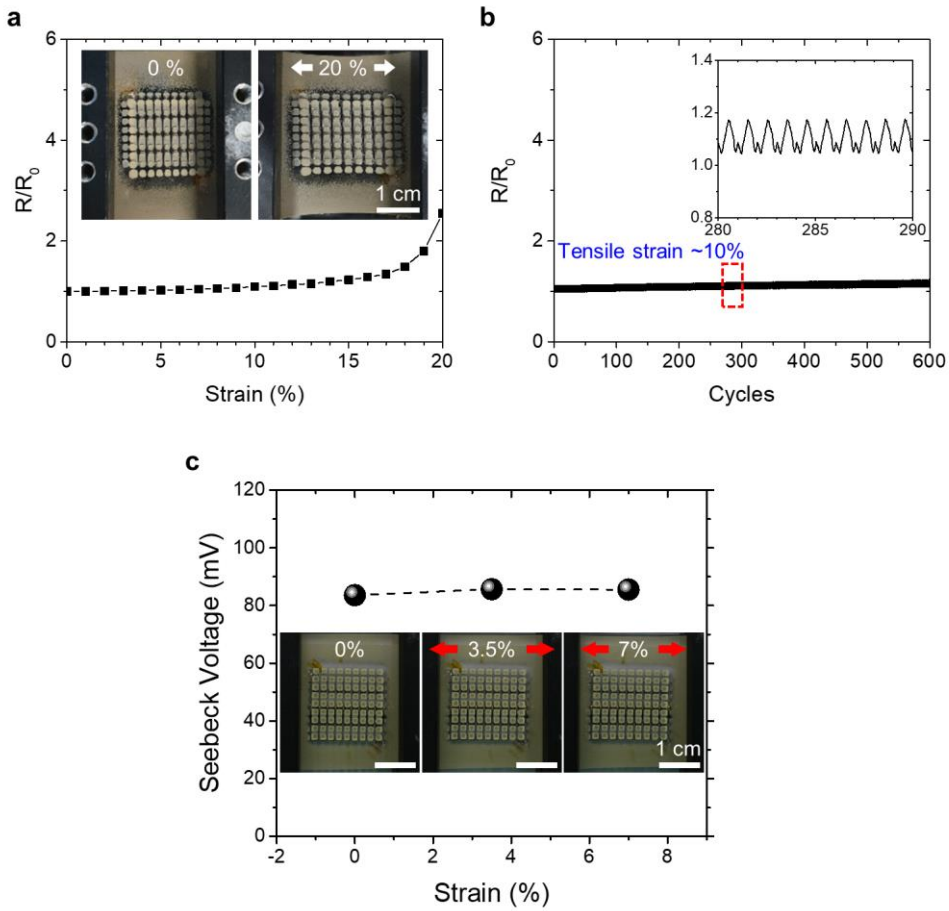

Figure 5.17 | Performance of the compliant TEG under stretching conditions. a, Resistance change as a function of a tensile strain. The inset photographs show the compliant TEG under a strain of 0 and 20%. **b**, Resistance change of the compliant TEG under cyclic stretching with a tensile strain of ~10%. The inset shows an enlarged view of the recorded data. **c**, V_{OC} generated by the stretched TEG at a $\Delta T_{\mathrm{Applied}}$ of 10 K.

5.3.3 Enhanced TE Performance on 3D Surfaces *via* Conformability

Due to the high degree of mechanical freedom and softness of the low-thermal-impedance STCs, the proposed compliant TEG could form unprecedented conformal contact with various 3D heat sources, resulting in significantly enhanced TE performance on them. The superior conformability of the proposed compliant TEGs became crystal clear when compared with previous methods. A reference TEG (r-TEG) was fabricated using Bi_2Te_3 TE legs and Cu electrodes, which have been widely employed in previous flexible TEGs. Its bending deformation was then compared with that of the compliant TEG with SEHPs (c-TEG). Figure 5.18 presents the bending morphologies of the two TEGs. The r-TEG showed a rugged and angular deformation at the bottom surface, and it even fractured from the PDMS substrate due to the concentrated tensile strain (Figure 5.18a). This is because of the large Young's modulus difference between the Cu electrodes and the

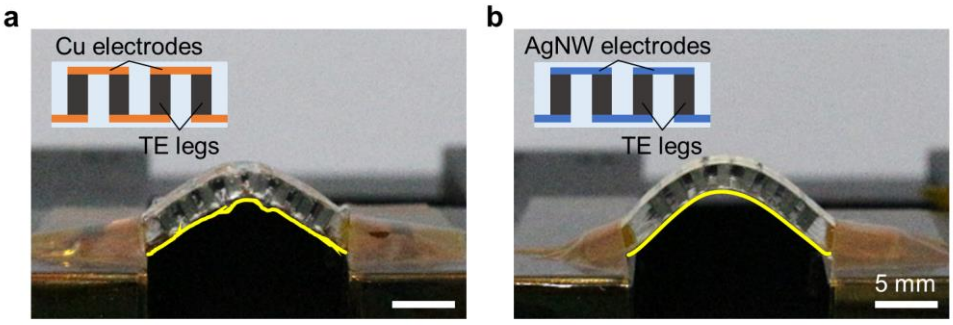

Figure 5.18 | Comparison of bending morphologies of the Cu-electrode-based TEG and AgNW-electrode-based TEG. a and **b**, Photographs of bent TEGs comprising Bi_2Te_3 legs and Cu electrodes (**a**) and AgNW-based soft electrodes (**b**).

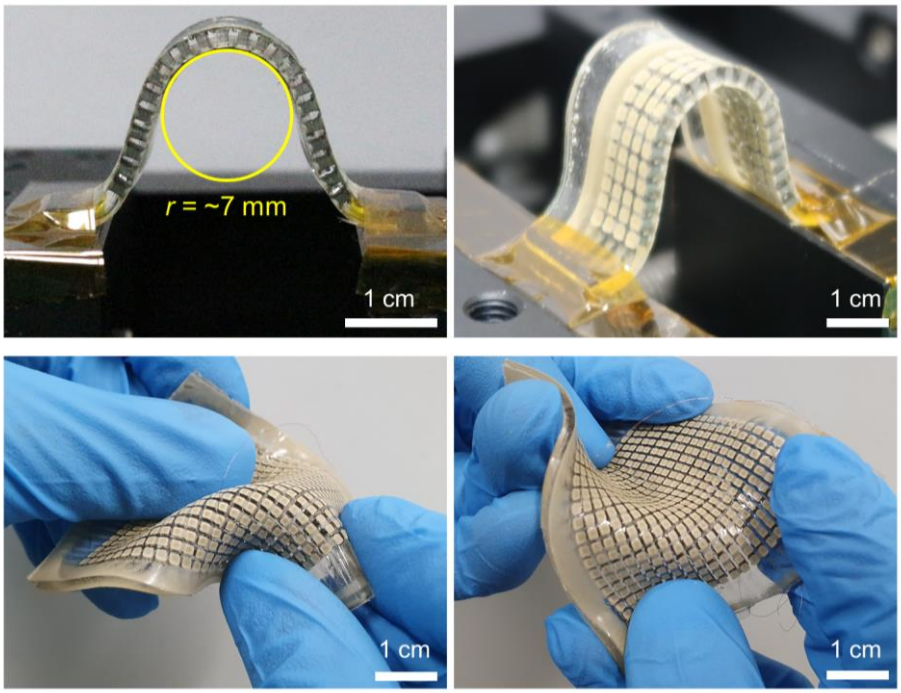

Figure 5.19 | Photographs of the compliant TEGs showing extremely high conformability under various deformations.

PDMS matrix. On the other hand, the c-TEG showed a smooth and free-flowing deformation (Figure 5.18b). The smooth surface under deformation is attributed to the low Young's modulus of the AgNW electrodes, which can effectively absorb the strain energy. This enables highly conformable contact between the c-TEG and complex 3D surfaces. Figure 5.19 presents the photographs of the c-TEGs showing high conformability under various deformation. The c-TEG can be softly and easily deformed by hand. It even formed a perfect 7-mm-radius circle without fracture. For a systematic investigation of the effect of the improved conformability on TE performance on 3D heat sources, a FEA was conducted to compare the V_{OC} of the r-TEG and c-TEG that are attached to a curved heat source. Figure 5.20 presents the

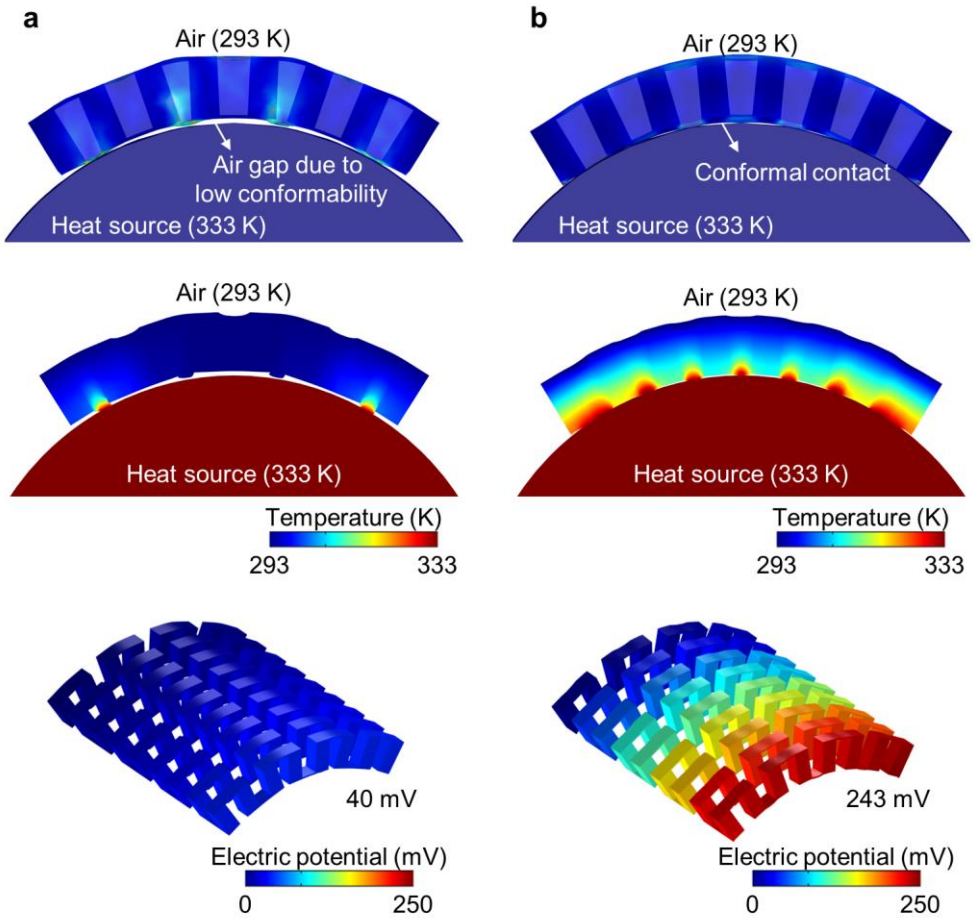

Figure 5.20 | Effect of conformability on TE performance. a and **b**, FEA results showing different conformability of the r-TEG (**a**) and c-TEG (**b**), and its effect on heat transfer and TE performance.

simulation results. As shown in Figure 5.20a, the r-TEG cannot perfectly wrap the curved surface, resulting in undesirable air gaps. These air gaps substantially impeded the heat transfer from the heat source to the bottom surface of the TEG. As a result, the TE performance of the r-TEG was significantly inhibited. On the contrary, the c-TEG formed a perfect fit to the curved surface without air gaps, facilitating much better heat transfer to the

TE legs (Figure 5.20b). The resulting V_{OC} was ~243 mV, ~600% higher than that of the r-TEG. These FEA results highlight that the proposed approach can significantly improve the energy harvesting efficiency of compliant TEGs on 3D heat sources. The TE performance of the compliant TEGs on different 3D surfaces was experimentally compared to further demonstrate reliable energy harvesting on 3D surfaces. The compliant TEG was attached to different positions of a bell-shaped aluminum cup with anisotropic bending curvatures (Figure 5.21a). The V_{OC} of the TEG on each position was monitored in real time when 78 °C water was abruptly poured into the cup. The TEG generated a maximum V_{OC} of ~340 mV, and no significant difference was observed in the time-resolved V_{OC} according to the position

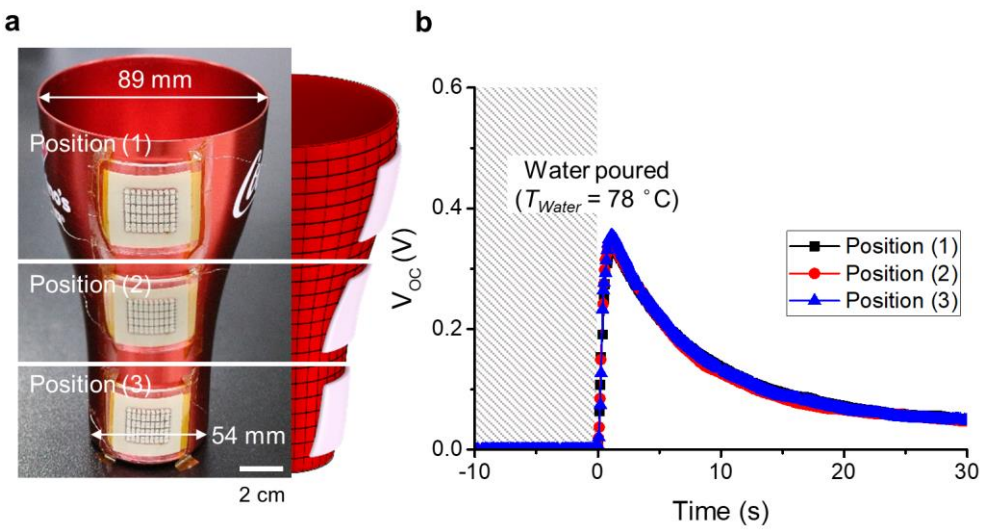

Figure 5.21 | Comparison of TE performance of the compliant TEG on different 3D surfaces. a, Photographs of a TEG attached to different positions of a bell-shaped aluminum cup. The schematic image shows the different bending curvatures of each position. **b**, Time-resolved V_{OC} of the TEG attached to each position when hot water is poured into the cup.

(Figure 5.21b). This result demonstrates the efficient heat collection of the compliant TEG regardless of the shapes of the heat source. Furthermore, due to the highly placed TE performance and unprecedented conformability, the compliant TEG showed high TE performance when attached to human skin. The TEG was attached to various body parts such as a hand, palm, forearm, neck, thigh, and shoulder, and its V_{OC} was monitored in real time (Figure 5.22a). It generated the V_{OC} of 266 mV that is corresponding to the maximum power density of 6.96 μW cm^{-2} when attached to the hand (Figure 5.22b). These values are the highest record in previously reported wearable TEGs on human skin without heat sinks (Figure 5.22c).

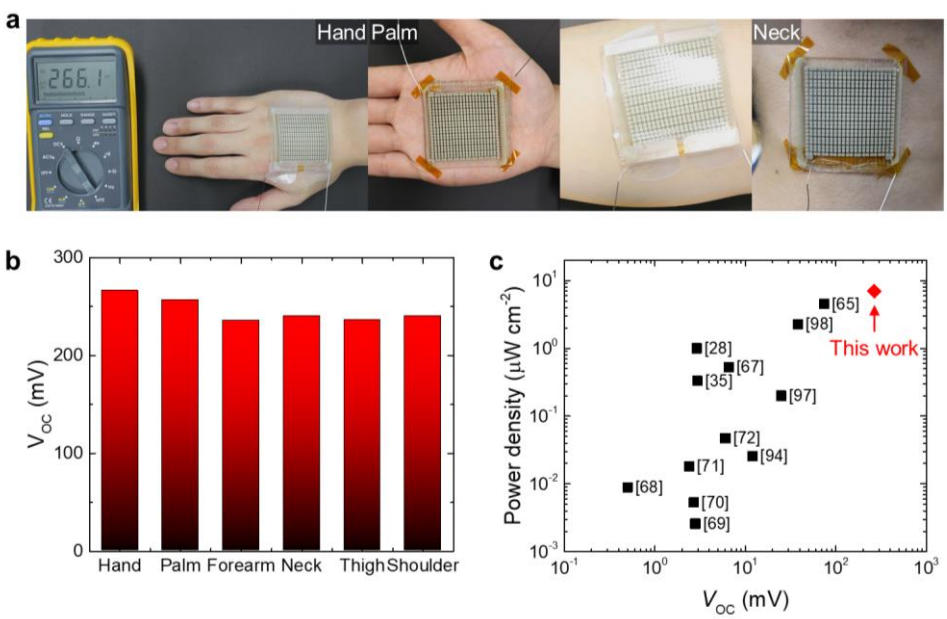

Figure 5.22 | TE performance of the compliant TEG on human skin. a, Photographs of the compliant TEG attached to various body parts. **b**, V_{OC} of the compliant TEG attached to the body parts. **c**, Summary of power density and V_{OC} of wearable TEGs attached to human skin without heat sinks [28,35,65,67-72,94,97,98].

5.3.4 Self-Powered Wearable Applications

A fully self-powered wearable device that provides an alert about an abrupt temperature increase was demonstrated using the compliant TEG. A flexible printed circuit board (f-PCB) with a step-up voltage converter and five mini-LEDs was designed and integrated with the 220-np-pair TEG. Figure 5.23 shows the self-powered LED system comprising the compliant TEG and f-PCB. Only two terminals were used to connect the TEG and circuit, minimizing the possibility of electrical failure. Figure 5.24 is the circuit diagram for step-up voltage conversion and LED operation. The circuit consists of a voltage regulator (LTC3105, Linear Technology), capacitors, resistors, an inductor, and red LEDs (SML-P11UT). Although the 220-np-pair TEG can generate sufficient power for most wearable applications, the stable maintenance of higher voltage is required for practical applications.

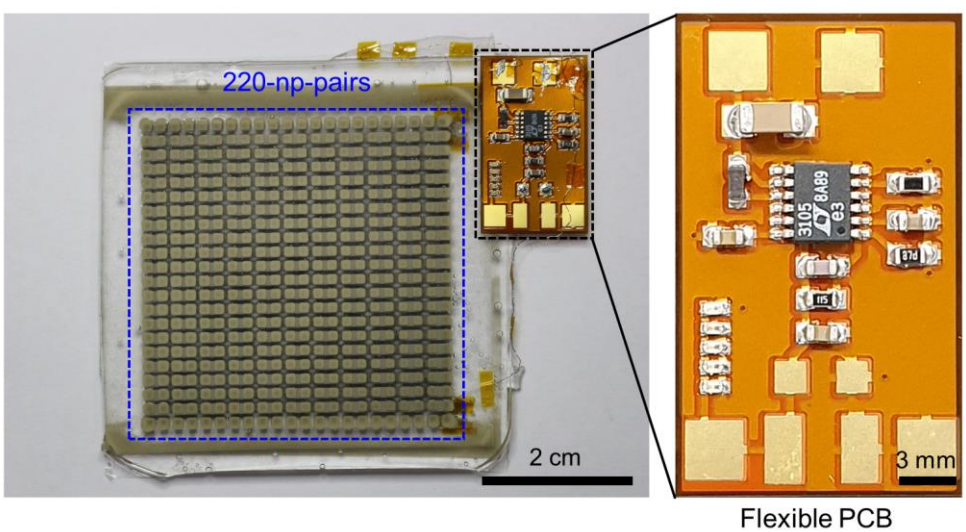

Figure 5.23 | Photograph of the 220-np-pair compliant TEG connected with an f-PCB with a step-up voltage converter and five mini-LEDs.

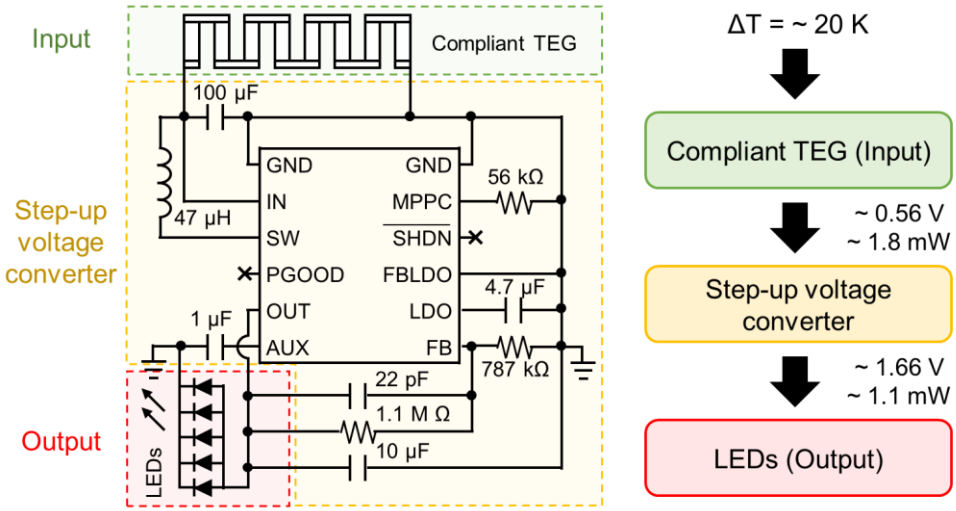

Figure 5.24 | Circuit diagram for step-up voltage conversion and LED operation.

Therefore, the circuit was designed to raise the output voltage to the turn-on voltage of the LED (~1.6 V) with high power efficiency and maintain it without fluctuation. When $\Delta T_{\text{Applied}}$ was ~20 K, the TEG generated ~1.8 mW at 0.56 V, and the output voltage of the step-up converter connected with LEDs was ~1.66 V with ~1.1 mW, which was sufficient to turn on the LEDs. It should be noted that only the compliant TEG powered the flexible circuit system without additional power supply. The minimum $\Delta T_{\text{Applied}}$ to turn on the LEDs was calculated to be ~13 K. Figure 5.25 shows the input and output voltages of the step-up converter and the resulting LED operation when the TEG was placed on a hot plate for a sufficient $\Delta T_{\text{Applied}}$. The input voltage abruptly increased to ~0.56 V after the TEG was placed on the hot plate. The output voltage was raised to ~1.66 V, instantaneously turning on the LEDs. Then, the generated voltages gradually decreased as the thermal equilibrium state was reached.

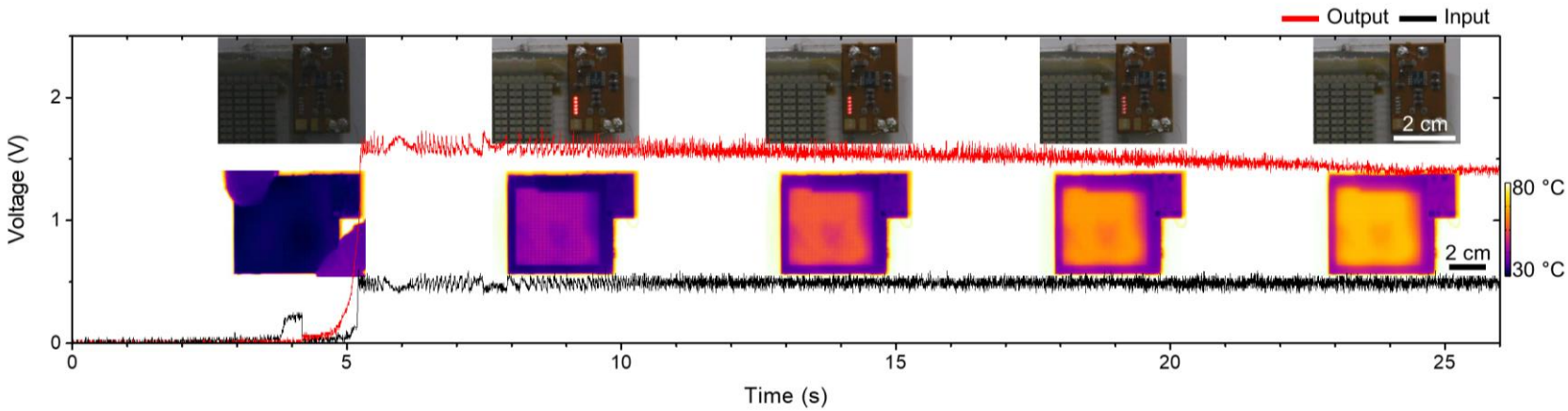

Figure 5.25 | Input and output voltages of the step-up converter when the TEG was put on a hot plate for a sufficient temperature difference. The upper insets are photographs showing that the LEDs turned on after the TEG was placed in contact with the hotplate. The bottom insets are thermograms showing the temperature of the upper surface of the TEG.

"Hot surface warning gloves" were fabricated by integrating the self-powered LED system, light masking packages, and oven gloves. Figure 5.26a illustrates the design of the self-powered hot surface warning gloves. When the TEG-attached gloves were used to grasp various hot objects, such as a glass bottle and a kettle, the conformal contact between the TEG and the 3D surfaces resulted in a bright 'H' sign, without the assistance of external power (Figure 5.26b). This demonstration highlights the feasibility of the high-performance compliant TEG in practical wearable applications.

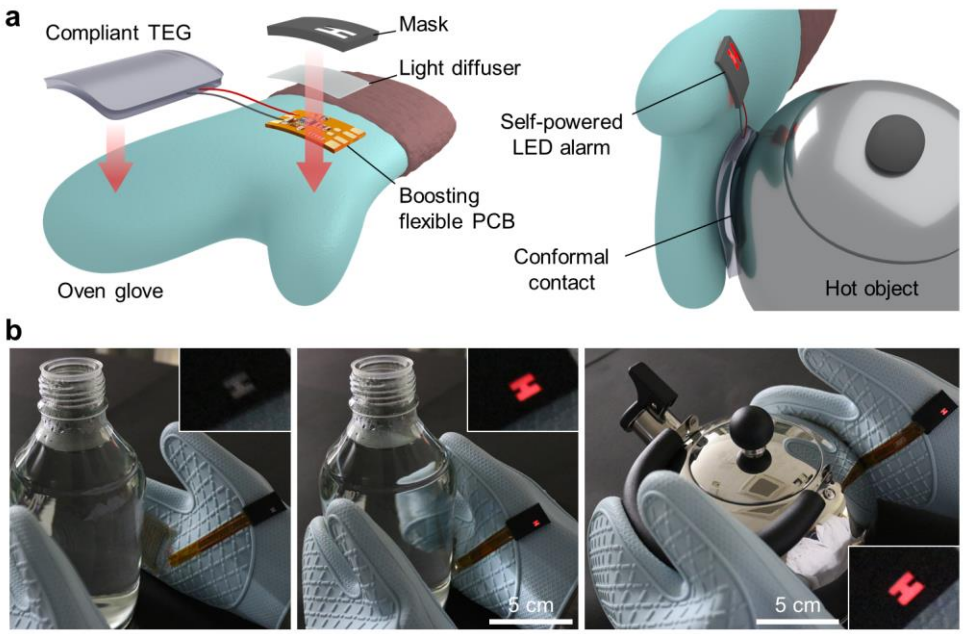

Figure 5.26 | Hot surface warning gloves with a self-powered LED system and light masking packages. **a**, Schematic illustration showing the structure of the gloves comprising the compliant TEG, flexible circuit, and package. **b**, photographs showing the demonstration of the gloves when they are used to grasp various hot objects such as a bottle and a kettle. The insets show an enlarged view of the H sign.

5.4 Conclusion

This chapter introduced an unprecedentedly conformable TEG with high TE performance arising from an improved heat transfer ability. The STCs in the SHEPs maximize the $\frac{\Delta T_{\mathrm{TE}}}{\Delta T_{\mathrm{Applied}}}$ up to ~80%, resulting in a ~260% improvement in the output power compared to the TEG without s-HCs. In addition, intrinsically stretchable interconnections effectively absorb strain energy, improving mechanical reliability and deformability of the TEG that is even stretchable up to ~20%. The approach facilitates unprecedented conformal contact with arbitrary 3D surfaces, thus significantly minimizing energy loss in undesirable air gaps, which has been a chronic limitation of previous flexible and wearable TEGs using rigid interconnections. Due to their excellent conformability, the compliant TEG achieves the highest TE performance on human skin, proving its superiority in energy harvesting on 3D heat sources. A self-powered wearable warning system for arbitrary hot features is successfully demonstrated, showing the feasibility of the proposed approach. The automated additive manufacturing with high yield under ambient conditions realizes low-cost, high-fill-factor, and highly customizable TEGs beyond laboratory-scale applications, shedding light on the mass-production of wearable TEGs. Future work would include further improvement in TE performance, such as conductivity of stretchable interconnections. This direction could significantly minimize waste heat from changing 3D heat sources, paving the way toward the realization of wearable and self-powered IoT devices.

Chapter 6

Summary, Limitations, and Recommendations for Future Researches

6.1 Summary and Conclusion

In this dissertation, the novel materials, methodologies, and designs were proposed to improve the mechanical conformability of the two essential devices for self-powered wearable electronics, *i.e.*, tactile sensors and thermoelectric generators. The strategy for improving conformability was fairly optimized for each device, considering its structure, performance, and potential advantages. Because the devices cannot become soft and thin simultaneously due to the performance issues, the most suitable one between the two strategies was chosen. For the selected scheme, the appropriate device structures were designed to substantially enhance their mechanical conformability without compromising their basic performance (or even improving their characteristics). In this stage, the composite materials such as cellulose nanocomposites and magnetic composites played critical roles for

both thickness-based and softness-based strategies. The enhanced conformability facilitated the spatial signal/heat transfer from 3D surfaces in each device. This augmented the functionalities of each device, such as high-spatial-fidelity pressure imaging and significantly improved TE performance on 3D heat sources. The performances reinforced by the engineered conformability were properly characterized, and they were compared with those of the state-of-the-art technologies in each area to show the necessity and validity of the proposed strategies. The feasibility of the proposed methodologies was further verified by the demonstration of practical and novel wearable applications.

For wearable tactile sensors, the ultrathin nanocellulose composite for contact-resistance-based pressure sensors and the photonic skin capable of pressure imaging with extremely high spatial fidelity were introduced in Chapter 2 and Chapter 3. Since soft materials exploited in pressure sensors generally cause considerable performance degradation and poor reliability, the thickness-based strategy was most effective in realizing ultra-conformable pressure sensors. Especially, challenging the conventional sense that engineered microstructures are beneficial to the performance of pressure sensors, the ultrathin CNN featuring a nanostructured surface showed numerous advantages that previous sensors have not achieved, such as ultrahigh sensitivity (> 5000 kPa^{-1}), wide working range (~1 MPa) with great linearity, ultrafast response time (< 1 ms), and high mechanical reliability. Furthermore, due to the ultrathin morphology under 1 μm thick, the sensing layer can transfer and sense high-resolution pressure distribution without distortion arising from the thick and inhomogeneous sensing film. Therefore, the photonic skin comprising the CNN and electroluminescent film can image

high-spatial-fidelity pressure distribution without the need for pixel structures. The experimental results showed that the device could clearly visualize the spatial pressure applied by a 1000 dpi pillar array, and the FEA calculated the maximum spatial resolution of ~6000 dpi. Furthermore, the systematic experiments and FEA figured out the effect of the thickness of a sensing layer on the spatial signal transfer. The ultraflexible device further enabled novel touch interfaces that can identify the user in addition to touch position and force.

For wearable TEGs, intrinsically soft interconnection platforms with enhanced heat transfer ability and highly conformable TEGs using the platforms were proposed in Chapter 4 and Chapter 5. Because the miniaturization of TEGs is limited due to the need for a sufficient thermal gradient, the softening of the rigid components was an efficient way to enable conformal contact between the TEG and 3D heat sources. The self-assembly of magnetic particles formed heat-conducting paths in an elastomeric matrix, which substantially improved the heat transfer ability of the SHEP without compromising its softness. Furthermore, the AgNW random networks embedded in the SHEP maintained their high conductivity under a tensile strain without affecting the softness of the SHEP. The compliant TEG was fabricated by integrating high-performance inorganic TE legs with the SHEPs *via* a fully automated process. The intrinsically stretchable electrodes effectively lowered the flexural rigidity of the TEG. As a result, the compliant TEG could form unprecedented conformal contact with a curved surface. This facilitates heat transfer from the 3D heat source to the TEG, which has been impeded by air gaps due to the limited conformability of previous flexible TEGs. Furthermore, the enhanced heat transfer ability *via* STCs minimized

the heat loss across the soft platforms, enabling superior energy harvesting performance on the 3D surfaces such as human skin. By using the proposed compliant TEGs, a practical self-powered wearable system was demonstrated. The gloves lighted up a warning sign about an abrupt increase in temperature without additional power supply.

In conclusion, this dissertation provides a systematic and fundamental framework for enhancing mechanical conformability of e-skin and thereby improving the transfer of spatial signals and energy from time-dynamic and complex 3D surfaces. The materials, manufacturing methods, and devices introduced here will be actively exploited in practical and futuristic applications of wearables and e-skin such as skin-attachable advanced user interfaces, implantable bio-imaging systems, nervous systems in soft robotics, and self-powered artificial tactile systems. In particular, the devices developed here can be directly integrated into flexible and soft electronic systems without degrading their flexibility and softness, augmenting their functionalities by effectively resolving the technical issues arising from the limited conformability. Furthermore, the framework explained in this dissertation can be universally applied to other fields that require improvement in signal/energy transfer through conformal contact with 3D surfaces.

6.2 Limitations and Recommendations for Future Works

6.2.1 Pressure Sensors and Photonic skin

The next milestone using the ultrathin and high-performance pressure sensor proposed in Chapter 2 is the electrical mapping of high-resolution pressure distribution. Direct mapping of pressure distribution into electrical signals without the need for digital imaging systems would be beneficial in many practical applications. Although the ultrathin morphology of the CNN allows us to implement conformable electroluminescent skin that can image the high-resolution pressure distribution with superior spatial fidelity, the electrical mapping of high-resolution spatial pressure is still challenging. It should be noted that complicated structures such as electrodes and vertical interconnection accesses need to be fabricated by the traditional semiconductor process to achieve 1000 dpi or higher-resolution sensor arrays. Furthermore, it is on a thin and flexible substrate where such a sophisticated process must be performed to obtain highly conformable pressure mapping devices. If the backplane is successfully fabricated, the high-resolution pressure distribution on 3D surfaces can be directly mapped into the electrical signals, where the ultrathin CNN would play a critical role. In the case of the photonic skin, because the electroluminescent layer is based on the solution-processed QLED, the passivation issue needs to be resolved. Since the thickness of the total structure directly affects the quality of the output image, it should remain under a few micrometers. Therefore, this is closely related to the thin-film encapsulation. Such directions would expand the range of applications using highly conformable pressure sensors and photonic skin.

6.2.2 Compliant TEGs

Although the compliant TEGs using SHEPs described in Chapters 4 and 5 achieved a high level of conformability as compared to conventional flexible TEGs, they still have rigid skeletons such as rigid TE legs and conductive epoxy. These rigid parts inevitably introduce soft-rigid interfaces where the tensile strain is focused when deformed and mechanical fracture could easily occur. Therefore, the strategy for soft TEGs without such rigid parts, namely, intrinsically soft TEGs is required. For example, the composites of elastomers and inorganic TE particles could be exploited for realizing intrinsically soft TE legs. Otherwise, organic TE materials have great potential as an active part of soft TEGs, if they are appropriately engineered to have softness and stretchability. However, in this case, the insufficient performance of the organic TE materials compared to those of the inorganic materials should be taken into account and the solution for improving the performance needs to be suggested. Furthermore, the electrical conductivity of the stretchable electrodes is another main issue to be resolved to improve the energy efficiency of soft TEGs. If such issues are successfully resolved, intrinsically soft TEGs with uncompromised TE performance would significantly increase the energy harvested from the waste heat by perfectly adhering to complex 3D surfaces without airgaps.

Bibliography

[1] Kim, D.-H. *et al.* Epidermal electronics, *Science* **333**, 838 (2011).

[2] Byun, J. *et al.* Electronic skins for soft, compact, reversible assembly of wirelessly activated fully soft robots. *Sci. Robot.* **3,** eaas9020 (2018).

[3] Byun, J. *et al*. Fully printable, strain-engineered electronic wrap for customizable soft electronics. *Sci. Rep.* **7**, 45328 (2017).

[4] Xu, J. *et al.* Highly stretchable polymer semiconductor films through the nanoconfinement effect. Science **355**, 6320 (2017).

[5] Wang, S. *et al.* Skin electronics from scalable fabrication of an intrinsically stretchable transistor array. *Nature* **555,** 83–88 (2018).

[6] Hua, Q. *et al.* Skin-inspired highly stretchable and conformable matrix networks for multifunctional sensing. *Nat. Commun.* **9,** 244 (2018).

[7] Kaltenbrunner, M. *et al.* An ultra-lightweight design for imperceptible plastic electronics. *Nature* **499,** 458–463 (2013).

[8] Park, S. *et al.* Self-powered ultra-flexible electronics via nano-grating-patterned organic photovoltaics. *Nature* **561,** 516–521 (2018).

[9] Yokota, T. *et al.* Ultraflexible organic photonic skin. *Sci. Adv.* **2,** e1501856 (2016).

[10] Fan, F.-R. *et al.* Transparent Triboelectric Nanogenerators and Self-Powered Pressure Sensors Based on Micropatterned Plastic Films. *Nano Lett.* **12,** 3109–3114 (2012).

[11] Pan, L. *et al.* An ultra-sensitive resistive pressure sensor based on hollow-sphere microstructure induced elasticity in conducting polymer film. *Nat. Commun.* **5,** 3002 (2014).

[12] Bae, G. Y. *et al.* Linearly and Highly Pressure-Sensitive Electronic Skin Based on a Bioinspired Hierarchical Structural Array. *Adv. Mater.* **28,** 5300–5306 (2016).

[13] Amjadi, M., Yoon, Y. J. & Park, I. Ultra-stretchable and skin-mountable strain sensors using carbon nanotubes-Ecoflex nanocomposites. *Nanotechnology* **26,** 375501 (2015).

[14] Cai, G. *et al.* Extremely Stretchable Strain Sensors Based on Conductive Self-Healing Dynamic Cross-Links Hydrogels for Human-Motion Detection. *Adv. Sci.* **4,** 1600190 (2017).

[15] Trung, T. Q., Ramasundaram, S., Hwang, B.-U. & Lee, N.-E. An All-Elastomeric Transparent and Stretchable Temperature Sensor for Body-Attachable Wearable Electronics. *Adv. Mater.* **28,** 502–509 (2016).

[16] Gao, W. *et al.* Fully integrated wearable sensor arrays for multiplexed in situ perspiration analysis. *Nature* **529,** 509–514 (2016).

[17] Lee, H. *et al.* A graphene-based electrochemical device with thermoresponsive microneedles for diabetes monitoring and therapy. *Nat. Nanotechnol.* **11,** 566–572 (2016).

[18] Kang, S.-K. *et al.* Bioresorbable silicon electronic sensors for the brain. *Nature* **530,** 71–76 (2016).

[19] Kim, Y. *et al.* A bioinspired flexible organic artificial afferent nerve. *Science* **360,** 998–1003 (2018).

[20] Yu, X. et al. Skin-integrated wireless haptic interfaces for virtual and augmented reality. *Nature* **575**, 473 (2019)

[21] Jung, S. *et al.* Reverse-Micelle-Induced Porous Pressure-Sensitive Rubber for Wearable Human-Machine Interfaces. *Adv. Mater.* **26,** 4825–4830 (2014).

[22] Cañón Bermúdez, G. S. *et al.* Magnetosensitive e-skins with directional perception for augmented reality. *Sci. Adv.* **4,** eaao2623 (2018).

[23] Kim, J. *et al.* Stretchable silicon nanoribbon electronics for skin prosthesis. *Nat. Commun.* **5,** 5747 (2014).

[24] Gerratt, A. P., Michaud, H. O. & Lacour, S. P. Elastomeric Electronic Skin for Prosthetic Tactile Sensation. *Adv. Funct. Mater.* **25,** 2287–2295 (2015).

[25] Kim, H.-J., Sim, K., Thukral, A. & Yu, C. Rubbery electronics and sensors from intrinsically stretchable elastomeric composites of semiconductors and conductors. *Sci. Adv.* **3,** e1701114 (2017).

[26] Xu, S., *et al.* Self-powered nanowire devices. *Nat. Nanotechnol.* **5,** 366–373 (2010).

[27] Lai, Y.-C. *et al.* Entirely, Intrinsically, and Autonomously Self-Healable, Highly Transparent, and Superstretchable Triboelectric Nanogenerator for Personal Power Sources and Self-Powered Electronic Skins. *Adv. Funct. Mater.* **29**, 1904626 (2019).

[28] Kim, S. J., We, J. H. & Cho, B. J. A wearable thermoelectric generator fabricated on a glass fabric. *Energy Environ. Sci.* **7**, 1959–1965 (2014).

[29] Son, D. *et al.* An integrated self-healable electronic skin system fabricated via dynamic reconstruction of a nanostructured conducting network. *Nat. Nanotechnol.* **13**, 1057 (2018).

[30] Markvicka, E. J., Bartlett, M. D., Huang, X. & Majidi, C. An autonomously electrically self-healing liquid metal–elastomer composite for robust soft-matter robotics and electronics, *Nat. Mater.* **17**, 618-624 (2018).

[31] Miyamoto, A. *et al.* Inflammation-free, gas-permeable, lightweight, stretchable on-skin electronics with nanomeshes. *Nat. Nanotechnol.* **12,** 907–913 (2017).

[32] Jeong, J.-W. *et al.* Materials and optimized designs for human-machine interfaces via epidermal electronics. *Adv. Mater.* **25**, 6839–6846 (2013).

[33] Mohammed, M. G. & Krammer, R. All-Printed Flexible and Stretchable Electronics. *Adv. Mater.* **29**, 1604965 (2017).

[34] Fassler, A. & Majidi, C. Liquid-Phase Metal Inclusions for a Conductive Polymer Composite. *Adv. Mater.* **27**, 1928 (2015).

[35] Suarez, F. *et al.* Flexible thermoelectric generator using bulk legs and liquid metal interconnects for wearable electronics. *Appl. Energy* **202,** 736–745 (2017).

[36] Ladd, C., So, J.-H., Muth, J. & Dickey, M. D. 3D Printing of Free Standing Liquid Metal Microstructures. *Adv. Mater.* **25**, 5081 (2013).

[37] Kim, S. *et al.* Revisit to three-dimensional percolation theory: Accurate analysis for highly stretchable conductive composite materials. *Sci. Rep.* **6**, 34632 (2016).

[38] Amjadi, M., Pichitpajongkit, A., Lee, S., Ryu, S. & Park, I. Highly Stretchable and Sensitive Strain Sensor Based on Silver Nanowire-Elastomer Nanocomposite. *ACS Nano* **8**, 5154-5163 (2014).

[39] Xu, F., & Zhu, Y. Highly Conductive and Stretchable Silver Nanowire Conductors. *Adv. Mater.* **24**, 5117–5122 (2012)

[40] Yan, C. Y. *et al.* An Intrinsically Stretchable Nanowire Photodetector with a Fully Embedded Structure. *Adv. Mater.* **26**, 943-950 (2014).

[41] Kim, S. *et al.* Negatively Strain-Dependent Electrical Resistance of Magnetically Arranged Nickel Composites: Application to Highly Stretchable Electrodes and Stretchable Lighting Devices. *Adv. Mater.* **26**, 3094-3099 (2014).

[42] Chortos, A. *et al.* Investigating Limiting Factors in Stretchable All-Carbon Transistors for Reliable Stretchable Electronics. *ACS Nano* **11**, 7925-7937 (2017).

[43] Kim, K. H., Vural, M. & Islam, M. F. Single-Walled Carbon Nanotube Aerogel-Based Elastic Conductors. *Adv. Mater.* **23**, 2865 (2011).

[44] Matsuhisa, N. *et al.* Printable elastic conductors by in situ formation of silver nanoparticles from silver flakes. *Nat. Mater.* **16**, 834-840 (2017).

[45] Darabi, M. A. *et al.* Skin-Inspired Multifunctional Autonomic-Intrinsic Conductive Self-Healing Hydrogels with Pressure Sensitivity, Stretchability, and 3D Printability. *Adv. Mater.* **29**, 1700533 (2017)

[46] Larson, C. *et al.* Highly stretchable electroluminescent skin for optical signaling and tactile sensing. *Science* **351**, 1071-1074 (2016).

[47] Hu, L. B. *et al.* Stretchable, Porous, and Conductive Energy Textiles. *Nano Lett.* **10**, 708-714 (2010).

[48] Oh, E. *et al.* Modulus-gradient Conductive Core-shell Structures Formed by Magnetic Self-assembling and Printing Processes for Highly Stretchable Via Applications. *Adv. Electron. Mater.* **3**, 1600517 (2017).

[49] Byun, J. *et al.* A Single Droplet-Printed Double-Side Universal Soft Electronic Platform for Highly Integrated Stretchable Hybrid Electronics, *Adv. Funct. Mater.* **27**, 1701912 (2017).

[50] Wang, Y. *et al.* A highly stretchable, transparent, and conductive polymer. *Sci. Adv.* **3**, e1602076 (2017)

[51] Mannsfeld, S. C. B. *et al.* Highly sensitive flexible pressure sensors with microstructured rubber dielectric layers. *Nat. Mater.* **9,** 859–864 (2010).

[52] Chen, L., Chen, G. & Lu, L. Piezoresistive Behavior Study on Finger-Sensing Silicone Rubber/Graphite Nanosheet Nanocomposites. *Adv. Funct. Mater.* **17,** 898–904 (2007).

[53] Gong, S. *et al.* A wearable and highly sensitive pressure sensor with ultrathin gold nanowires. *Nat. Commun.* **5,** 3132 (2014).

[54] Zhan, Z. *et al.* Paper/Carbon Nanotube-Based Wearable Pressure Sensor for Physiological Signal Acquisition and Soft Robotic Skin. *ACS Appl. Mater. Interfaces* **9,** 37921–37928 (2017).

[55] Tao, L.-Q. *et al.* Graphene-Paper Pressure Sensor for Detecting Human Motions. *ACS Nano* **11,** 8790–8795 (2017).

[56] Wei, Y., Chen, S., Lin, Y., Yuan, X. & Liu, L. Silver nanowires coated on cotton for flexible pressure sensors. *J. Mater. Chem. C* **4,** 935–943 (2016).

[57] Xu, X. *et al.* Copper Nanowire-Based Aerogel with Tunable Pore Structure and Its Application as Flexible Pressure Sensor. *ACS Appl. Mater. Interfaces* **9,** 14273–14280 (2017).

[58] Yao, H.-B. *et al.* A Flexible and Highly Pressure-Sensitive Graphene-Polyurethane Sponge Based on Fractured Microstructure Design. *Adv. Mate.* **25,** 6692–6698 (2013).

[59] Lv, L., Zhang, P., Xu, T. & Qu, L. Ultrasensitive Pressure Sensor Based on an Ultralight Sparkling Graphene Block. *ACS Appl. Mater. Interfaces* **9,** 22885–22892 (2017).

[60] Hou, C., Wang, H., Zhang, Q., Li, Y. & Zhu, M. Highly Conductive, Flexible, and Compressible All-Graphene Passive Electronic Skin for Sensing Human Touch, *Adv. Mater.* **26**, 5018-5024 (2014)

[61] Choong, C.-L. *et al.* Highly Stretchable Resistive Pressure Sensors Using a Conductive Elastomeric Composite on a Micropyramid Array. *Adv. Mater.* **26,** 3451–3458 (2014).

[62] Park, J. *et al.* Giant Tunneling Piezoresistance of Composite Elastomers with Interlocked Microdome Arrays for Ultrasensitive and Multimodal Electronic Skins. *ACS Nano* **8,** 4689–4697 (2014).

[63] Jian, M. *et al.* Flexible and Highly Sensitive Pressure Sensors Based on Bionic Hierarchical Structures. *Adv. Funct. Mater.* **27,** 1606066 (2017).

[64] Nan, K. *et al.* Compliant and stretchable thermoelectric coils for energy harvesting in miniature flexible devices. *Sci. Adv.* **4,** eaau5849 (2018).

[65] Hong, S. *et al.* Wearable thermoelectrics for personalized thermoregulation. *Sci. Adv.* **5,** eaaw0536 (2019).

[66] Kim, S. J. *et al.* High-Performance Flexible Thermoelectric Power Generator Using Laser Multiscanning Lift-Off Process. *ACS Nano* **10,** 10851–10857 (2016).

[67] Wang, Y., Shi, Y., Mei, D. & Chen, Z. Wearable thermoelectric generator to harvest body heat for powering a miniaturized accelerometer. *Appl. Energy* **215,** 690–698 (2018).

[68] Jeong, S. H. *et al.* Stretchable Thermoelectric Generators Metallized with Liquid Alloy. *ACS Appl. Mater. Interfaces* **9,** 15791–15797 (2017).

[69] Oh, J. Y. *et al.* Chemically exfoliated transition metal dichalcogenide nanosheet-based wearable thermoelectric generators. *Energy Environ. Sci.* **9**, 1696–1705 (2016).

[70] Liu, H., Wang, Y., Mei, D., Shi. Y. & Chen, Z. Design of a Wearable Thermoelectric Generator for Harvesting Human Body Energy. *Wear. Sens. Robots* **399**, 55–66 (2016).

[71] Kim, M.-K., Kim, M.-S, Lee, S., Kim, C. & Kim, Y.-J. Wearable thermoelectric generator for harvesting human body heat energy. *Smart Mater. Struct.* **23**, 105002 (2014).

[72] Lu, Z., Zhang, H., Mao, C. & Li, C. M. Silk fabric-based wearable thermoelectric generator for energy harvesting from the human body. *Appl. Energy* **164**, 57–63 (2016).

[73] Wu, Q. & Hu, J. A novel design for a wearable thermoelectric generator based on 3D fabric structure. *Smart Mater. Struct.* **26**, 045037 (2017).

[74] Lee, B. *et al.* Ultraflexible and transparent electroluminescent skin for real-time and super-resolution imaging of pressure distribution. *Nat. Commun.* **11**, 663 (2020).

[75] Bae, E. J., Kang, Y.-H., Jang, K.-S. & Cho, S. Enhancement of Thermoelectric Properties of PEDOT:PSS and Tellurium-PEDOT:PSS Hybrid Composites by Simple Chemical Treatment. *Sci. Rep.* **6,** 18805 (2016).

[76] Wang, Q., Jian, M., Wang, C. & Zhang, Y. Carbonized Silk Nanofiber Membrane for Transparent and Sensitive Electronic Skin. *Adv. Funct. Mater.* **27,** 1605657 (2017).

[77] Jeong, H., Noh, Y., Ko, S. H. & Lee, D. Flexible resistive pressure sensor with silver nanowire networks embedded in polymer using natural formation of air gap. *Compos. Sci. Technol.* **174,** 50–57 (2019).

[78] Chen, S., Song, Y. & Xu, F. Flexible and Highly Sensitive Resistive Pressure Sensor Based on Carbonized Crepe Paper with Corrugated Structure. *ACS Appl. Mater. Interfaces* **10,** 34646–34654 (2018).

[79] Nardes, A. M., Kemerink, M. & Janssen, R. A. J. Anisotropic hopping conduction in spin-coated PEDOT:PSS thin films. *Phys. Rev. B* **76**, 085208 (2007).

[80] Zhou, J. *et al.* The temperature-dependent microstructure of PEDOT/PSS films: insights from morphological, mechanical and electrical analyses. *J. of Mater. Chem. C* **2**, 9903-9910 (2014).

[81] Kamaya, M. & Kawakubo, M. A procedure for determining the true stress-strain curve over a large range of strains using digital image correlation and finite element analysis. *Mech. Mater.* **43,** 243–253 (2011).

[82] Takei, K. *et al.* Nanowire active-matrix circuitry for low-voltage macroscale artificial skin. *Nat. Mater.* **9,** 821–826 (2010).

[83] Lin, L. *et al.* Triboelectric Active Sensor Array for Self-Powered Static and Dynamic Pressure Detection and Tactile Imaging. *ACS Nano* **7,** 8266–8274 (2013).

[84] Wang, X. *et al.* Self-Powered High-Resolution and Pressure-Sensitive Triboelectric Sensor Matrix for Real-Time Tactile Mapping. *Adv. Mater.* **28,** 2896–2903 (2016).

[85] Wang, X. *et al.* Full Dynamic-Range Pressure Sensor Matrix Based on Optical and Electrical Dual-Mode Sensing. *Adv. Mater.* **29,** 1605817 (2017).

[86] Wang, C. *et al.* User-interactive electronic skin for instantaneous pressure visualization. *Nat. Mater.* **12,** 899–904 (2013).

[87] Pan, C. *et al.* High-resolution electroluminescent imaging of pressure distribution using a piezoelectric nanowire LED array. *Nat. Photonics* **7,** 752–758 (2013).

[88] Peng, M. *et al.* High-Resolution Dynamic Pressure Sensor Array Based on Piezo-phototronic Effect Tuned Photoluminescence Imaging. *ACS Nano* **9,** 3143–3150 (2015).

[89] Bao, R. *et al.* CdS nanorods/organic hybrid LED array and the piezo-phototronic effect of the device for pressure mapping. *Nanoscale* **8,** 8078–8082 (2016).

[90] Wang, X. *et al.* Dynamic Pressure Mapping of Personalized Handwriting by a Flexible Sensor Matrix Based on the Mechanoluminescence Process. *Adv. Mater.* **27,** 2324–2331 (2015).

[91] Park, C. *et al.* Quick, Large-Area Assembly of a Single-Crystal Monolayer of Spherical Particles by Unidirectional Rubbing. *Adv. Mater.* **26,** 4633-4638

(2014).

[92] Kim, K. K. *et al.* Transparent wearable three-dimensional touch by self-generated multiscale structure. *Nat. Commun.* **10,** 2582 (2019).

[93] Russ, B., Glaudell, A., Urban, J. J., Chabinyc, M. L. & Segalman, R. A. Organic thermoelectric materials for energy harvesting and temperature control. *Nat. Rev. Mater.* **1**, 16050 (2016).

[94] We, J. H., Kim, S. J. & Cho, B. J. Hybrid composite of screen-printed inorganic thermoelectric film and organic conducting polymer for flexible thermoelectric power generator. *Energy* **73**, 506–512 (2014).

[95] Jeong, M. H. *et al.* Increasing the thermoelectric power factor of solvent-treated PEDOT:PSS thin films on PDMS by stretching. *J. Mater. Chem. A* **6**, 15621–15629 (2018).

[96] Zhang, T. *et al.* Mechanically Durable and Flexible Thermoelectric Films from PEDOT:PSS/PVA/$Bi_{0.5}Sb_{1.5}Te_3$ Nanocomposites. *Adv. Electron. Mater.* **3**, 1600554 (2017).

[97] Jo, S. E., Kim, M. K., Kim, M. S. & Kim, Y. J. Flexible thermoelectric generator for human body heat energy harvesting. *Electron. Lett.* **48,** 1015–1017 (2012).

[98] Kim, C. S. *et al.* Structural design of a flexible thermoelectric power generator for wearable applications. *Appl. Energy* **214,** 131–138 (2018).

Publication List

International Journals

1. **B. Lee**[†], H. Cho[†], K. T. Park, J.-S. Kim, M. Park, H. Kim*, Y. Hong*, and S. Chung*, "High-performance compliant thermoelectric generators with magnetically self-assembled soft heat conductors for self-powered wearable electronics," *Nat. Commun.* (Under Review).
2. **B. Lee**[†], J.-Y. Oh[†]*, H. Cho, C. W. Joo, H. Yoon, S. Jeong, E. Oh, J. Byun, H. Kim, S. Lee, J. Seo, C. W. Park, S. Choi, N.-M. Park, S.-Y. Kang, C.-S. Hwang, S.-D. Ahn, J.-I. Lee, and Y. Hong*, "Ultraflexible and transparent electroluminescent skin for real-time and super-resolution imaging of pressure distribution," *Nat. Commun.* **11**, 663 (2020).
3. J. Byun[†], **B. Lee**[†], E. Oh, H. Kim, S. Kim, S. Lee, and Y. Hong*, "Fully printable, strain-engineered electronic wrap for customizable soft electronics," *Sci. Rep.* **7**, 45328 (2017).
4. S. Choi, S. Lee, **B. Lee**, T. Kim*, and Y. Hong*, "Selective Crack Formation on Stretchable Silver Nano-particle Based Thin Films for Customized and Integrated Strain-sensing System," *Thin Solid Films* **707**, 138068 (2020).

5. S. Jeong, H. Yoon, **B. Lee**, S. Lee, and Y. Hong*, "Distortion-free Stretchable Light-Emitting Diodes via Imperceptible Microwrinkles," *Adv. Mater. Technol.*, 2000231 (2020).

6. J. Seo, J. Ha, **B. Lee**, H. Kim, and Y. Hong*, "Fluoroelastomer encapsulation for enhanced reliability of solution-processed carbon nanotube thin-film transistors," *Thin Solid Films* **704**, 138021 (2020).

7. J. Park†, G. Kim†, **B. Lee**, S. Lee, P. Won, H. Yoon, H. Cho, S. Ko, and Y. Hong*, "Highly Customizable Transparent Silver Nanowire Patterning via Inkjet-printed Conductive Polymer Templates Formed on Various Surfaces", *Adv. Mater. Technol.*, 2000042 (2020).

8. J. O. Kim, J. S. Hur, D. Kim, **B. Lee**, J. M. Jung, H. A. Kim, U. J. Chung, S. H. Nam, Y. Hong, K.-S. Park, J. K. Jeong*, "Network Structure Modification-Enabled Hybrid Polymer Dielectric Film with Zirconia for the Stretchable Transistor Applications," *Adv. Funct. Mater.* **30**, 1906647 (2020).

9. H. Cho, Y. Lee, **B. Lee**, J. Byun, S. Chung*, and Y. Hong*, "Stretchable strain tolerant soft printed circuit board: A systematic approach for design rules of stretchable interconnects," *J. Inf. Disp.* **21**, 41-47 (2020).

10. J. Park, H. Yoon, G. Kim, **B. Lee**, S. Lee, S. Jeong, T. Kim, J. Seo, S. Chung, Y. Hong*, "Highly Customizable All Solution–Processed Polymer Light Emitting Diodes with Inkjet Printed Ag and Transfer Printed Conductive Polymer Electrodes," *Adv. Funct. Mater.* **29**, 1902412 (2019).

11. J. Yoon†, Y. Joo†, E. Oh, **B. Lee**, D. Kim, S. Lee, T. Kim, J. Byun*, and Y. Hong*, "Soft Modular Electronic Blocks (SMEBs): A Strategy for Tailored Wearable Health-Monitoring Systems," *Adv. Sci.* **6**, 1801682 (2019).

12. E. Oh, T. Kim, J. Yoon, S. Lee, D. Kim, **B. Lee**, J. Byun, H. Cho, J. Ha, and Y. Hong*, "Highly Reliable Liquid Metal-Solid Metal Contacts with

a Corrugated Single-Walled Carbon Nanotube Diffusion Barrier for Stretchable Electronics," *Adv. Funct. Mater.* **28**, 1806014 (2018).

13. J. Byun†, Y. Lee†, J. Yoon, **B. Lee**, E. Oh, S. Chung, T. Lee, K.-J. Cho*, J. Kim*, and Y. Hong*, "Electronic skins for soft, compact, reversible assembly of wirelessly activated fully soft robots," *Sci. Robot.* **3**, eaas9020 (2018).

14. S. Lee, S. Lee, H. Yoon, C.-K. Lee, C. Yoo, J. Park, J. Byun, G. Kim, **B. Lee**, B. Lee, and Y. Hong*, "Printed cylindrical lens pair for application to the seam concealment in tiled displays," *Opt. Express* **26**, 824 (2018).

15. J. Byun†, E. Oh†, **B. Lee**, S. Kim, S. Lee, and Y. Hong*, "A Single Droplet-Printed Double-Side Universal Soft Electronic Platform for Highly Integrated Stretchable Hybrid Electronics," *Adv. Funct. Mater.* **27**, 1701912 (2017).

16. Y. Joo, J. Yoon, J. Ha, T. Kim, S. Lee, **B. Lee**, C. Pang, and Y. Hong*, "Highly sensitive and bendable capacitive pressure sensor and its application to 1V operation pressure sensitive transistor," *Adv. Electron. Mater.* **3**, 1600455 (2017).

17. E. Oh, J. Byun, **B. Lee**, S. Kim, D. Kim, J. Yoon, and Y. Hong*, "Modulus-gradient Conductive Core-shell Structures Formed by Magnetic Self-assembling and Printing Processes for Highly Stretchable Via Applications," *Adv. Electron. Mater.* **3**, 1600517 (2017).

18. S. Kim, S. Choi, E. Oh, J. Byun, H. Kim, **B. Lee**, S. Lee, and Y. Hong*, "Revisit to three-dimensional percolation theory: Accurate analysis for highly stretchable conductive composite materials," *Sci. Rep.* **6**, 34632 (2016).

19. J. Kim, Y. Jeong, H. Kim, C.-K. Lee, **B. Lee**, J. Hong, Y. Kim, Y. Hong, S.-D. Lee, and B. Lee*, "F-number matching method in light field microscopy using an elastic micro lens array," *Opt. Lett.* **41**, 2751 (2016).

International Conferences

1. **B. Lee**, J.-Y. Oh, H. Cho, H. Yoon, S. Jeong, N.-M. Park, C.-S. Hwang, S.-D. Ahn, J.-I. Lee, Y. Hong, "Ultraflexible and Transparent Pressure-Imaging Skin Using Cellulose/Nanowire Nanohybrid Networks for High-Information-Density Human-Machine Interfaces," *2019 Materials Research Society (MRS) Fall Meeting & Exhibit*, Boston, USA, December, 2019 (Poster).
2. **B. Lee**, J. Seo, H. Cho, T. Kim, and Y. Hong, "Printed Integration of High-Performance Intrinsically Stretchable TFTs with Soft Sensors for Mass Customization of Wearable Electronics," *2018 Materials Research Society (MRS) Fall Meeting & Exhibit*, Boston, USA, November, 2018 (Poster).
3. **B. Lee**, J. Seo, T. Kim, and Y. Hong, "Fabrication and Characterization of Nanocomposite Dielectrics for Applications in Intrinsically Stretchable Thin Film Transistors," *27th International Conference on Amorphous and Nanocrystalline Semiconductors (ICANS 27)*, Seoul, Korea, August, 2017 (Poster).
4. **B. Lee**, J. Byun, E. Oh, H. Kim, S. Kim, and Y. Hong, "All-Ink-Jet-Printed Wearable Information Display Directly Fabricated onto an Elastomeric Substrate," *SID Display Week 2016*, San Francisco, USA, May, 2016 (Oral presentation).
5. **B. Lee**, J. Byun, and Y. Hong, "Rationally Designed Topographic Configuration of Elastomeric System for Inkjet Printed Stretchable Electronics," *International Conference on Electronic Materials and Nanotechnology for Green Environment 2014 (ENGE 2014)*, Jeju, Korea, November, 2014 (Oral presentation).

Patents

1. Y. Hong, E. Oh, J. Byun, **B. Lee** (SNU R&DB Foundation), "Forming method of stretchable substrate having via and stretchable substrate having via," USA, 16/476,784, 2019 (Application).
2. Y. Hong, **B. Lee**, J. Byun (SNU R&DB Foundation), "Method of fabricating stretchable electrical circuit and apparatus for fabricating stretchable electrical circuit," USA, 15/594,766, 2017 (Application).
3. 홍용택, 오은호, 변정환, **이병문** (서울대학교 산학협력단), "비아를 포함하는 신축성 기판 형성 방법 및 비아를 가지는 신축성 기판", 대한민국, 10-1953962, 2019 (등록).
4. 홍용택, **이병문**, 변정환 (서울대학교 산학협력단), "신장성 전기 회로 형성 방법 및 신장성 전기 회로 형성 장치", 대한민국, 10-1894137, 2018 (등록).
5. 홍용택, 이승환, **이병문**, 윤진수 (서울대학교 산학협력단), "신축성 겹눈 구조 모사 렌즈 및 그 제조 방법", 대한민국, 10-2020-0059730, 2020 (출원).
6. 홍용택, 윤형수, 오은호, **이병문**, 정수진 (서울대학교 산학협력단), "전자 장치 및 스탬핑과 자기장 정렬을 이용한 전자 소자의 전사 방법", 대한민국, 10-2020-0047364, 2020 (출원).
7. 정승준, 홍용택, **이병문**, 조현, 김희숙, 손정곤, 이상수, 김태안 (한국과학기술원, 서울대학교 산학협력단), "신축성 열전소자 및 그 제조방법", 대한민국, 10-2019-0158390, 2019 (출원).
8. 정승준, 홍용택, **이병문**, 손정곤, 김희숙, 이상수, 조현, 김태안 (한국과학기술원, 서울대학교 산학협력단), "열전 효율이 높은

신축성 열전소자 및 그 제조방법", 대한민국, 10-2019-0158343, 2019 (출원).

Other Publications

1. Y. Hong*, **B. Lee**, J. Byun, E. Oh, J. Yoon, H. Kim, S. Choi, and H. Cho, "*Invited Paper*: Strain-engineered Platform Technology for Stretchable Hybrid Electronics," *SID Symposium Digest of Technical Papers* **49**, 483-485 (2018)
2. J. Yoon, Y. Joo, **B. Lee**, E. Oh, H. Cho, and Y. Hong*, "*Late-News Poster*: Stretchable Active-Matrix Light-Emitting Diode Array Using Printed Electric Components on Plastic and Elastomer Hybrid Substrate," *SID Symposium Digest of Technical Papers* **49**, 1925-1927 (2018)
3. Y. Hong*, **B. Lee**, J. Byun, E. Oh, H. Kim, S. Kim, S. Lee, D. Kim, and J. Yoon, "*Invited Paper*: Key Enabling Technology for Stretchable LED Display and Electronic System," *SID Symposium Digest of Technical Papers* **48**, 253-256 (2017)
4. Y. Hong*, **B. Lee**, E. Oh, J. Byun, "Stretchable Displays: From Concept Toward Reality," *Information Display* **33**, 6-38 (2017)
5. **B. Lee**, J. Byun, E. Oh, H. Kim, S. Kim, Y. Hong*, "*Late-News Paper*: All-Ink-Jet-Printed Wearable Information Display Directly Fabricated onto an Elastomeric Substrate," *SID Symposium Digest of Technical Papers* **47**, 672-675 (2016)

국문 초록

인간 피부의 기계적 특성 및 기능을 모방하는 전자피부(electronic skin, e-skin)는 웨어러블 전자기기 분야의 트렌드를 바꾸고 있다. 기존의 웨어러블 전자기기가 단지 착용하는데 그쳤다면, 전자피부는 인간의 피부와 장기 표면에 완벽하게 붙어 동작함으로써 기존에는 접근 불가능 했던 다양한 생체 신호를 높은 신뢰도로 감지하고 처리할 수 있다. 실시간으로 감지 가능한 생체 신호의 확장은 사물인터넷(Internet of Things, IoT)의 성장을 획기적으로 가속화하고 헬스케어, 의료용 임플란트, 소프트 로봇 및 새로운 휴먼 머신 인터페이스로의 응용을 가능하게 한다.

전자피부의 필수요소인 센서와 에너지 소자에서는 삼차원 표면의 공간신호와 열에너지를 손실 없이 전달하는 것이 매우 중요하다. 이러한 공간 신호와 열에너지는 다양한 기하 구조와 전자소자를 거쳐 처리 가능한 신호로 전달된다. 이 과정에서 3 차원 표면에 빈틈없이 붙는 기계적 순응성(mechanical conformability)은 공간신호와 열에너지를 왜곡 없이 전달하는 것을 가능하게 한다. 전자피부의 기계적 순응성을 증가시키는 방법은 크게 다음과 같이 두 가지로 나눌 수 있다. (1) 전자피부를 두께를 낮추는 전략과 (2) 전자피부의 영률(Young’s modulus)을 낮추어 고무와 같이 부드럽게 만드는 전략이다. 하지만, 기존 센서 및 에너지 소자를 위한 재료

와 디자인이 각 장치의 성능을 향상시키는 것에 초점이 맞추어져 있기 때문에, 고성능을 유지하면서 매우 얇거나 연질 형태의 소자를 개발하는 것은 매우 도전적이었다. 따라서 고유연성을 확보하지 못한 기존 센서와 에너지 소자는 공간 신호 및 열 전달이 심각하게 저해되고, 이로 인해 공간 압력의 왜곡, 열전 효율의 저하와 같은 한계를 보여준다.

이 논문에서는 웨어러블 센서와 에너지 소자의 비약적인 기능 향상을 궁극적인 목표로, 각 소자에 최적화된 재료와 제작방식, 구조를 이용해 이들의 기계적 순응성을 획기적으로 높이고, 이를 통한 공간 신호 및 열 전달의 향상을 심도 있게 분석한다. 특히, 두께를 낮추거나 영률을 낮추는 두 가지 전략 중 각 소자에 가장 적합한 전략을 선택하고, 체계적인 방법론을 적용하여 이들의 기계적 순응성과 공간 신호 및 열 전달을 증진시킨다. 이 과정에서 나노융복합재료가 각 전략을 구현하는 핵심 요소로 작용한다. 각 소자에 따른 구체적인 연구 내용은 다음과 같다.

첫째, 압력 센서의 경우 초박막 셀룰로오스/나노와이어 복합체를 이용하여 고성능의 저항방식 압력 센서를 개발한다. 이러한 복합체는 표면에 형성된 고유한 나노구조 덕분에 마이크로구조체를 이용한 기존 압력 센서보다 월등한 성능을 보여준다. 특히, 1 마이크로 미터 수준의 매우 얇은 두께로 인해 접촉 물체의 복잡한 형상에 완벽하게 순응할 수 있고, 이로 인해 고해상도 압력 분포를 왜곡 없이 저항 분포로 전달할 수 있다. 이러한 압력 센서를

양자 점 발광소자와 결합하여 고해상도의 압력분포를 높은 정밀도로 이미징 가능한 발광 소자를 보고한다.

둘째, 열전 소자의 경우 기존의 금속 전극으로 인한 낮은 유연성과 탄성중합체의 낮은 열 전도도를 극복하기 위해 열 전달 능력이 획기적으로 향상된 낮은 영률의 소프트 전극 플랫폼을 개발한다. 소프트 플랫폼은 내부에 은 나노와이어 기반의 신축성 전극을 갖고 있으며, 자기장을 통해 자가 정렬된 금속 입자들이 효과적으로 외부 열을 열전 재료에 전달한다. 이를 기반으로 제작된 고유연성 열전 소자는 삼차원 열원에 빈틈없이 붙어 열 손실을 최소화 하며, 이로 인해 높은 열전 효율을 달성한다.

이 논문은 다양한 전자소자의 유연성을 증진시키고 이를 통한 공간 신호 및 열 전달의 향상을 도모하고 분석하는 체계적이고 종합적인 방법론을 제시했다는 데 큰 의의가 있다. 제안된 방법론은 분야에 국한되지 않고 다양한 소자의 개발에 적용할 수 있어 웨어러블 기기와 전자피부 분야의 기계적, 기능적 발전에 크게 기여할 것으로 기대된다. 뿐만 아니라 이 연구에서 최초로 개발한 소재 및 소자들은 다양한 웨어러블 어플리케이션과 산업에 곧바로 융합되고 응용될 수 있다. 이를 통해 신체 부착 및 삽입 가능한 생체 이미징 시스템, 소프트 로봇을 위한 신경 체계, 자가 발전이 가능한 인공 감각 기관, 가상 및 증강 현실을 위한 새로운 유저 인터페이스와 같은 미래 지향적 융합 어플리케이션의 실현을 앞당길 것으로 기대된다.